

NACA TN 4235 97501

0066805

TECH LIBRARY KAFB, NM

# NATIONAL ADVISORY COMMITTEE FOR AERONAUTICS

TECHNICAL NOTE 4235

OBSERVATIONS OF TURBULENT-BURST GEOMETRY  
AND GROWTH IN SUPERSONIC FLOW

By Carlton S. James

Ames Aeronautical Laboratory  
Moffett Field, Calif.



Washington

April 1958

AFMDC  
TECHNICAL



0066805

NACA TN 4235

## TABLE OF CONTENTS

SUMMARY . . . . .	1
INTRODUCTION . . . . .	1
SYMBOLS . . . . .	3
EXPERIMENTAL CONSIDERATIONS . . . . .	5
Sources of Data . . . . .	5
Optical Aspects of the Shadowgraphs . . . . .	5
METHOD OF ANALYSIS . . . . .	6
RESULTS AND DISCUSSION . . . . .	9
Burst Thickness Profiles . . . . .	9
Burst Plan Form and Transverse Growth . . . . .	11
Three-Dimensional Burst Shape . . . . .	15
Burst Upstream-Edge Velocity . . . . .	16
Effects of Mach number and Reynolds number . . . . .	17
Effect of surface roughness . . . . .	17
Burst Longitudinal Growth Rate . . . . .	19
Effect of Mach number . . . . .	20
Effect of surface roughness . . . . .	20
Burst Downstream-Edge Velocity . . . . .	21
Burst Formation Rate . . . . .	21
Effect of Mach number . . . . .	24
Effect of Reynolds number . . . . .	24
Effect of surface roughness . . . . .	25
Effect of leading-edge geometry . . . . .	25
Further Observations From the Shadowgraphs . . . . .	27
SUMMARY OF RESULTS . . . . .	30
REFERENCES . . . . .	31
TABLE . . . . .	32
FIGURES . . . . .	34

---

TECHNICAL NOTE 4235

---

OBSERVATIONS OF TURBULENT-BURST GEOMETRY

AND GROWTH IN SUPERSONIC FLOW

By Carlton S. James

SUMMARY

One step in the process of boundary-layer transition is the formation and spread of turbulent spots or bursts. A study of the shape, growth, and formation rate of turbulent bursts in supersonic boundary layers has been made using spark shadowgraphs of small gun-launched models in free flight through still air and through a countercurrent supersonic air stream. The shadowgraph data were obtained from a number of previous investigations which, collectively, represent a variety of model shapes, and a fairly wide range of Mach numbers, unit Reynolds numbers, surface roughnesses, and heat-transfer rates. The model shapes include cones, ogive-cylinders, and hollow cylinders aligned with the stream. The approximate ranges of the flow variables are as follows: free-stream Mach numbers from 2.7 to 10; unit Reynolds numbers from 1.6 million to 6.3 million per inch; surface roughness maximum peak-to-valley distance 10 microinches to 2100 microinches; and ratio of wall temperature to free-stream temperature either 1.0 (still air) or 1.8 (countercurrent air stream).

Three-dimensional burst geometry was determined for two typical turbulent bursts. From a comparison of burst plan forms and thickness profiles observed under different flow conditions, burst geometry was found to be insensitive to variation of Mach number, unit Reynolds number, and surface roughness. These variables, together with body shape, were found to have significant effects on the rate at which a burst is swept along the surface, its growth rate (relative to distance traveled), and the rate of burst formation.

INTRODUCTION

For many years scientists have sought to understand the fundamental nature of the transition from laminar to turbulent flow and the parameters which affect its occurrence. The present concept of the transition process, as outlined by Dryden in reference 1, is the result of numerous contributions by various investigators. Notable among these are the theoretical work of Tollmien and Schlichting and subsequent verification of the existence of Tollmien-Schlichting waves by Schubauer and Skramstad (ref. 2), the observance by Dryden (ref. 3) of the suddenness with which turbulence

first appears, and the hypothesis proposed by Emmons and Bryson (ref. 4) which has been recently substantiated in its essentials by the experiments of Schubauer and Klebanoff (ref. 5). Dryden separates the transition process into three successive steps:

- (1) The amplification of small disturbances
- (2) The generation of localized spots of turbulence through a secondary instability of the flow
- (3) The growth and spread of turbulent spots until the whole flow field is turbulent

If the initial disturbance is large, step (1) does not take place. Likewise the development of the secondary instability of step (2), which reference 1 associates with the formation of a system of Görtler type vortices (ref. 6), probably depends upon the nature as well as the magnitude of the initial disturbance. If, for example, the disturbance source is at a leading edge or on a surface, the generation of a localized spot, or burst, can occur without the need of steps (1) and (2). The process proceeds directly from the generation of the localized spot to step (3). The present paper is concerned with step (3) of this process.

From observations made during their water-table experiments, Emmons and Bryson (ref. 4) hypothesized that each minute spot or burst of turbulence once formed, grows perpendicular to its surface, and in all directions with respect to the fluid, by consuming the surrounding laminar boundary layer. As it grows it is swept along the surface by the main flow followed by newly formed bursts. The burst continues to grow until it merges with adjacent bursts to form a continuum of turbulent boundary layer.

As early as 1950 irregularities in the thickness of the turbulent boundary layer on free-flight models fired in the Ames supersonic free-flight wind tunnel were observed in spark shadowgraphs (ref. 7). Also observed in the flow field adjacent to the boundary layer were shock waves having angles much greater than Mach angles. These waves appeared to be associated with the turbulence irregularities. The Emmons and Bryson experiments, provided a plausible and timely explanation of the observed phenomenon. As the optics of the wind tunnel were improved and longer models were tested, discrete bursts of turbulence were observed more frequently and with sufficient clarity to define the geometric profiles of many of the bursts. In a study of boundary-layer transition on a slender ogive-cylinder body, Jedlicka, Wilkins, and Seiff (ref. 8) observed that the number of bursts that appeared in the boundary layer seemed to depend on surface roughness near the tip, and on abrupt changes in profile slope near the tip. These bursts were observed to sweep downstream along the surface. More recently, in a further study of boundary-layer transition on free-flight hollow-cylinder models, the present author was impressed by the fact that when two or more distinct bursts appeared along a single

streamline, the downstream burst was invariably larger than the upstream one. Furthermore, there was a striking similarity between the profiles of some of the observed bursts and the profile determined by Schubauer and Klebanoff from hot-wire measurements in low-speed flow. These observations are illustrated in figures 1 and 2. In the shadowgraph of figure 1 any given burst is seen to have greater length and thickness than bursts upstream of it. The implication is that a burst grows in length and thickness as it progresses downstream. Figure 2(a) reproduces a portion of figure 6 of reference 5 showing the plan form and center-line profile of a spark-initiated turbulent spot, or burst, on a flat plate in low-speed flow. (Nomenclature has been altered to conform to that of the present report.) Figure 2(b) is a shadowgraph profile, close to the plane of symmetry, of a burst on the ogive-cylinder model of reference 8. The similarity of the two profiles is quite apparent. The upper profile was measured at a stream Mach number of approximately 0.03. The lower profile was observed at a stream Mach number of 3.6. It should be pointed out, however, that in the elevation view of figure 2(a) the vertical scale is 2.4 times the horizontal scale. It is perhaps not surprising that such a similarity exists, since every boundary layer contains the full velocity spectrum from zero to the local stream value, and the effect of Mach number on the characteristics of the fully laminar or the fully turbulent boundary layer has proven to be largely one of degree. It remained, however, for such a comparison as this to drive home the real potentialities of the spark shadowgraph for the detailed study of bursts of turbulence in supersonic flow.

With an extensive portfolio of shadowgraphs, obtained during investigations of other phenomena, immediately available, it became of interest to determine how much information on the transition process these shadowgraphs could be made to yield. The purpose of the present report is to set forth the results of a study of these shadowgraphs.

#### SYMBOLS

$a_e$	local speed of sound at edge of the boundary layer, ft/sec
$c$	laminar boundary-layer thickness parameter, $\frac{\delta}{x} \sqrt{R_x}$ , dimensionless
$f$	frequency of burst formation, $\text{sec}^{-1}$
$\Delta f$	width of statistical class in sample of frequency observations, $\text{sec}^{-1}$
$H$	height of roughness, in.
$L$	length of burst, in.
$M_d$	Mach number of streamline at boundary-layer edge relative to downstream end of burst, dimensionless

$M_e$	Mach number of streamline at edge of boundary layer relative to the body surface, dimensionless
$M_u$	Mach number of streamline at boundary-layer edge relative to upstream end of burst, dimensionless
$M_\infty$	free-stream Mach number, dimensionless
$N$	number of observations in statistical sample, dimensionless
$n_{\Delta f}$	number of observations in statistical class of width $\Delta f$ , dimensionless
$Re_H$	Reynolds number based on roughness height, $\frac{U_e}{\nu} H$ , dimensionless
$Re_u$	Reynolds number at burst upstream edge, $\frac{U_e}{\nu} x_u$ , dimensionless
$Re_x$	Reynolds number based on distance $x$ , $\frac{U_e}{\nu} x$ , dimensionless
$r_o$	distance from burst origin to point at which transverse spread begins, in.
$t$	time, sec
$U_e$	local stream velocity at edge of the boundary layer, ft/sec, except when used as component of Reynold number, for which case, in./sec
$\frac{U_e}{\nu}$	Reynolds number per unit length based on conditions at edge of boundary layer, in. <sup>-1</sup>
$V_d$	velocity of downstream end of burst with respect to body surface, ft/sec
$V_u$	velocity of upstream end of burst with respect to body surface, ft/sec
$x$	coordinate in stream direction measured from burst origin, in.
$x_d$	distance of burst downstream end from burst origin, in.
$x_u$	distance of burst upstream end from burst origin, in.
$y$	coordinate normal to surface, in.
$z$	coordinate normal to $xy$ plane, in.
$\alpha$	half-angle of burst-growth envelope, deg (see fig. 2(a))

- $\delta$  thickness of laminar boundary layer, in.
- $\theta$  half-angle of burst downstream-end wedge, deg (see fig. 2(a))
- $\lambda$  wave spacing, in. (see fig. 2(b))
- $\nu$  coefficient of kinematic viscosity, in.<sup>2</sup>/sec
- $\phi$  radial angle of burst center-line meridian, measured in positive roll direction, from intersection of vertical center plane of wind tunnel with upper surface of model, deg
- $\psi$   $\tan^{-1} \left| \frac{z}{x} \right|$  on developed body surface

### EXPERIMENTAL CONSIDERATIONS

#### Sources of Data

The shadowgraphs which provided the greatest amount of information for the purposes of this study were obtained from the tests of reference 8, and from more recent tests on hollow cylinders aligned with the stream. Sketches of the models used in these tests are shown in figures 3(a), (b), and (c). To the slender ogive-cylinder of reference 8 the name "pencil model" has been ascribed. For the sake of simplicity it will be so referred to in the following paragraphs. The hollow cylinders were designed to provide quasi-two-dimensional flow over the outer surfaces. They were simply fin-stabilized open-ended tubes having sharp leading edges. The internal flow was always supersonic. Two exterior profiles were tested: a pure cylinder, and an open ogive segment tangent to a cylinder. These profiles will be referred to as the "straight tube" and the "contoured tube," respectively. Additional information was obtained from shadowgraphs of the 19° included-angle cones of reference 7, a few shadowgraphs of a model having the body profile of the A-4, a 10° included-angle cone, and a model of the NACA RM-10. These models are shown in figures 3(d), (e), (f), and (g), respectively. Representative shadowgraphs, from among the large group selected for study, are presented in figure 4.

#### Optical Aspects of the Shadowgraphs

Some of the shadowgraphs are of models in flight upstream through a wind tunnel (see ref. 9) while others are of models in flight in a conventional aeroballistic range. The optical system of the wind tunnel, for stations utilizing parallel light fields, requires light falling on the photographic plate first to reflect from a collimating mirror and then to

pass through two windows in the tunnel walls. For stations utilizing conical light fields, light from each source must pass through two windows. With the wind tunnel in the "air-off" condition (i.e., not operating - still air in the test section) resolution of detail in the shadowgraph is impaired due to imperfect collimation of the light and to a shadow pattern resulting from imperfections in the surfaces of the mirrors and windows. With the wind tunnel in the "air-on" condition (supersonic air stream) introduction of stream turbulence and a turbulent boundary layer on each window causes a large additional loss of resolution. The range shadowgraphs, on the other hand, were obtained using a conical light field with no intermediate optics at all. These shadowgraphs showed the greatest amount of detail. Since air-on testing was required to obtain data at Mach numbers above approximately 4, considerably less information on burst behavior could be gained above this Mach number than below it.

#### METHOD OF ANALYSIS

The initial step of the study was made from the point of view of determining whether or not the transition process remains fundamentally the same in supersonic flow as in subsonic flow. A general qualitative inspection of the shadowgraphs showed that, for the flow conditions represented: (1) bursts form at forward locations on the surface of a model; (2) they are swept downstream, growing in length and thickness as they go; and (3) their profiles bear a marked similarity to that of a burst in a low-speed boundary layer.

Some information from other sources was also available. From the angle of the shock wave emanating from the upstream edge<sup>1</sup> of a burst, Emmons and Bryson (ref. 4) calculated this edge to be moving downstream over the surface at 0.43 of the stream velocity, which is equivalent to 0.57 of the stream velocity in the upstream direction relative to the stream (i.e.,  $M_u/M_\infty = 0.57$ ). Their measurement was made on a spark shadowgraph of a cone-cylinder model flying at a Mach number of 2.1. By the same procedure Jedlicka, Wilkins, and Seiff (ref. 8) calculated a value of  $M_u/M_\infty$  equal to 0.4 for a burst on an ogive-cylinder flying at a Mach number of 3.5. Mitchner (ref. 10) and Schubauer and Klebanoff (ref. 5) reported values of 0.56 and 0.5, respectively, for low-speed flow.

The comparison thus far suggested that differences in the transition process between subsonic and supersonic flow were likely to be small. It was considered reasonable, therefore, for the purpose of the present study to adopt the concept of burst formation and growth already well substantiated for low-speed flow by the experiments of reference 5. If it is assumed that (a) a burst originates as a point, and (b) its upstream and

---

<sup>1</sup>To avoid possible ambiguities arising from use of the term "leading edge" as applied to a burst, the term "upstream edge" is used throughout this report to designate the edge of a burst nearest the model leading edge.



downstream edges move at constant - though not equal - velocities, a simple relationship can be written between these velocities and the positions of the edges relative to their point of origin. Using rectangular coordinates with origin at the point of origin of the burst, we can write

$$\left. \begin{aligned} x_u &= V_u t \\ x_d &= V_d t \end{aligned} \right\} \quad (1)$$

where  $t = 0$  at the instant the burst is formed. Substituting

$$L = x_d - x_u$$

and eliminating  $t$  leads to

$$\frac{V_d}{V_u} = \frac{L}{x_u} + 1 \quad (2)$$

From the shadowgraph, the velocity of the upstream end of a burst relative to the velocity of the stream can be determined by the angle the burst shock wave makes with the stream direction. (This velocity, of course, must be supersonic so that the technique is applicable only when  $M_e > \frac{1}{M_{u1}/M_e}$ .)

Formation of a burst shock wave commences with the formation of a burst (or shortly thereafter), the upstream edge of which then serves as a source for the continuous formation of the wave. Thus, ideally, the point of origin of a burst can be located by projecting the outer end of the burst shock wave (providing it has not already intersected the bow wave) forward along a Mach line to intersect the body profile.

Once the point of origin of a burst is established the distance from this point to the upstream end of the burst is determined and  $x_u$  and  $L$  can be measured directly from the shadowgraph. It is then possible to calculate  $V_d$  by substitution of the measured quantities into equation (2). A measure of the longitudinal growth of a burst is thus obtainable from the shadowgraphs.

From wave-angle measurements, the velocity of the burst upstream edge is given in terms of local Mach number. It is convenient, therefore, to put equation (2) in terms of Mach number. The Mach number of the local stream relative to the burst upstream edge is given by

$$M_{u1} = \frac{U_e - V_u}{a_e}$$

so that

$$\left. \begin{aligned} \frac{V_u}{U_e} &= 1 - \frac{M_u}{M_e} \\ \text{similarly,} \quad \frac{V_d}{U_e} &= 1 - \frac{M_d}{M_e} \end{aligned} \right\} \quad (3)$$

Substituting equations (3) in equation (2) results in

$$\frac{M_d}{M_e} = \frac{M_u}{M_e} - \frac{L}{x_u} \left( 1 - \frac{M_u}{M_e} \right) \quad (4)$$

In addition to the longitudinal growth characteristics it was found possible to obtain information concerning the plan form, thickness distribution, and lateral growth of a burst in supersonic flow. Presuming that a pair of shadowgraphs can be found, taken at the same instant and in orthogonal planes, in which the same burst appears in both, there are provided two, three, or four profiles of the burst, depending on its lateral extent, which have known spatial relationships. If the burst is on a cylindrical body the radius of which is large compared to the boundary layer or burst thickness, the flow can be considered two-dimensional and the cylinder can be developed into a plane. The coordinates of the burst plan form can then be plotted on the developed meridians of the cylinder. If the observed profiles of the burst are sufficiently distinct to be measured, it is also possible to map contours of burst thickness. The practical application of such a scheme, unfortunately, was subject to many limitations not the least of which was the requirement of finding a suitable pair of shadowgraphs in which a single uncontaminated burst was clearly visible in both. Two such pairs of shadowgraph were found, however, on which this approach was reasonably successful. In addition, a small group of shadowgraphs was found from which it was possible to obtain enough information to plot burst plan forms, but which would not yield sufficient information to define the complete three-dimensional form. Likewise, a number of individual profiles were sufficiently well defined to yield thickness distributions. In some of these cases the position of the profile with respect to the plane of symmetry of the burst could be approximately established. This was done by estimating the burst width from the known approximate transverse growth rate and bounding the lateral extremities of the burst by the orthogonal meridians, views of which showed laminar flow. For bursts whose estimated widths were nearly equal to the surface distance between the diametral meridians (half the body circumference), the observed profile must be close to the plane of symmetry.

## RESULTS AND DISCUSSION

The length of a transition region, which may be defined as the region between the forwardmost point at which bursts form and the aftermost point at which laminar flow exists, depends upon the streamwise velocity of the bursts, their transverse and longitudinal growth characteristics, and their rate of formation. Each of these variables is in turn dependent upon the environmental conditions of the flow. It is this order of consideration which has been followed as closely as possible in presenting the present results, so that a logical picture of burst behavior in supersonic flow may be drawn. Consideration of the dynamic aspects of burst behavior is preceded by a discussion of the observed geometric characteristics.

## Burst Thickness Profiles

Burst thickness distributions measured on several profiles lying close to the plane of symmetry are shown in figure 5. To facilitate comparisons of shape the profiles are plotted in terms of burst length, although the absolute magnitudes of the bursts varied considerably. Important environmental parameters are tabulated to the right of each profile. The most prominent feature of this figure is the similarity of shape of the profiles. Thickness increases continuously from the upstream end to a maximum at about 70 percent of the burst length  $L$  ( $\pm 10$  percent), then decreases continuously to the downstream end. This similarity extends to the low-speed profile of figure 2(a), except that its maximum thickness point is located at about 50-percent  $L$ . Parameters such as Mach number, Reynolds number, heat-transfer rate, and surface shape, as well as burst size, have no discernible effect on the burst profile shape within the ranges of these parameters observed here. The domelike shape at  $x/L = 0.75$  of profiles (a) and (d) of figure 5 is due in each case to the presence of a relatively large eddy jutting out from the general mass of eddies that form the burst. The local humps appearing in profiles (b), (f), and (g) are due to the same cause, except that the eddies are smaller than those of profiles (a) and (d). It is interesting to note the same local character of the hump in the profile of figure 2(a). While the profile shapes are well established, the absolute values of thickness are less certain. A combination of diffraction and refraction of light rays passing through the boundary layer and close to the model body occurs, affecting the shadowgraph image. The diffraction fringe appearing in the shadowgraph obliterates the detail of the relatively thin laminar boundary layer. There is, therefore, some uncertainty as to how much of the thinner end portions of a burst are also obscured. The fringe is apparent in all of the shadowgraph figures and may be seen very clearly on the lower profile of the body in figure 6(b), which is an enlargement of a portion of a shadowgraph. Comparison of measured fringe widths with calculated values (ref. 11) of laminar boundary-layer thickness at the upstream edges of

bursts indicates that the ratio of fringe width to boundary-layer thickness varies between approximately 1.2 and 3. To give a comparison with burst thickness the calculated laminar boundary-layer thickness at the upstream edge of each burst is indicated in figure 5.

In measuring thickness distribution on one burst profile ((d) in fig. 5), three variations in technique were tried in order to assess the accuracy of the measurements. The first, which was used for most of the measurements, employed direct measurement by means of a drafting scale, with the aid of a magnifying glass of about 2 power, on contact prints of the shadowgraph negatives. To define the model surface under the burst the inside edge of the diffraction fringe was located at each end of the burst and extended under it with a straight edge. Measurements made in this manner are represented in figure 5 by circle symbols. A second variation of this technique was to use the same procedure on positive enlargements of about 8X to 10X made directly from the shadowgraph negatives. Examples of such enlargements, but to a lower magnification in order to accommodate them to page size, are shown in figure 6. Figure 6(a) is an enlargement of the burst of figure 2(b), and corresponds to profile (d) of figure 5. Thickness measurements from these enlargements are represented by square symbols in figure 5. The third variation involved accounting for the effects of diffraction and refraction by noting the difference between the apparent body diameter and the known body diameter. The body axis is located on the shadowgraph from symmetry. Measurements are then made from the axis to the outer profile of the burst and the true body radius is subtracted. It was anticipated that this method would be the most accurate. However, large differences in the amount of refraction occurring in the boundary layers of bodies of different diameter were found. On the pencil model the correction to the apparent body radius was about equal to the width of the diffraction fringe and appeared to be compatible with the visible portion of the burst profile. On the hollow-tube models this correction in most cases was nearly equal to the maximum thickness of the burst and therefore did not appear to be compatible with the visible portion of the burst profile. The triangular-symbol curve of profile (d) is the result of applying this procedure to a burst on the pencil model. The three curves of profile (d) show good repeatability of shape representation but differ in absolute thickness by more than 20 percent of the maximum value. This is approximately equal to the width of the diffraction fringe in figure 2(b). For other profiles of figure 5, a reasonable value of absolute thickness should be obtained by adding the laminar boundary-layer thickness to the ordinate of the profile. The average maximum thickness, including this  $\delta$  correction, of the ten profiles of figure 5 is found to be about 4 percent of the burst length.

It is clear that the present data cannot define the shape of the burst profile within the thickness of the diffraction fringe. This thickness is of the same order of magnitude as the laminar boundary-layer thickness in all cases encountered in this study. The position of the upstream end of a burst is usually well defined by its shock wave (cf. fig. 6). Thus, the finite thickness indicated at this point in many of the profiles suggests

that the profile shape is the same as that found at the upstream end of a burst in low-speed flow (cf. fig. 2(a)). No conclusions can be drawn concerning the profile shape at the downstream end. It will be assumed, for present purposes, that the shape is similar to that for low-speed flow and that the intersection of the extrapolated burst profile with the diffraction fringe marks its point of "maximum advance" as noted in figure 2(a).

#### Burst Plan Form and Transverse Growth

Four developed plan-form plots, which typify the results of this phase of the study, appear in figure 7. The model tip, or leading edge, is at the left, the direction of air flow being from left to right. The horizontal lines mark the edges of the body cylinder observed in the shadowgraph profiles. All bursts for which plan forms could be drawn were situated on the cylindrical portions of the model bodies. Therefore no distortion is introduced by plotting these plan forms as if the flow were on a flat plate. No evaluation of the effects of longitudinal and transverse curvature of the real model surface on burst plan form can be made with the present data. The extremities of the observed profiles are marked on the appropriate edges which correspond to meridians and the plan form is faired through these points. From the better defined plan forms, the general shape and symmetry of the outline were established. This knowledge was used as a guide in the fairing of other outlines which, taken individually, were poorly defined. The burst of figure 7(a), observed on the straight tube, is shown in the shadowgraphs of figures 4(d) and 4(e). Since these shadowgraphs were obtained with conical light fields, the observed meridians are not quite equally spaced around the circumference of the body cylinder. The burst plan form is seen to extend across two meridians and come almost tangent to a third. The third and fourth meridians show laminar flow. The burst of figure 7(b) was observed on the pencil model (fig. 6(b)). Its plan form extends across three meridians, with the fourth still showing laminar flow. The free-stream Mach numbers at which these bursts were observed were 3.9 and 3.5, respectively. The corresponding values of unit Reynolds number were  $2.3 \times 10^6$  per inch and  $2.0 \times 10^6$  per inch. The wall to free-stream static-temperature ratio was 1.0 for both. These plan forms, particularly the latter, closely resemble the burst plan form observed by Schubauer and Klebanoff in low-speed flow (ref. 5) which is reproduced in figure 2(a). The small differences between the plan form of figure 2(a) and those of figures 7(a) and 7(b) appear no greater than the differences between the latter two plan forms themselves. This comparison indicates that the general characteristics of the shape of a turbulent spot, or burst, remain unaffected by large changes in Mach number, unit Reynolds number, or heat-transfer rate. The main points of difference, which again appear to be small, are the slenderness, the indentation of the upstream end, and the transverse and longitudinal rates of growth.

The slenderness of a burst may be characterized by the angle between the two relatively straight sides which form the downstream-end wedge. The half-angle,  $\theta$ , of this wedge is found to be  $18\text{--}1/2^\circ$  for the plan form of figure 7(a) and  $10^\circ$  for the plan form of figure 7(b) as compared to  $15.3^\circ$  reported in reference 5 for a burst in low-speed flow (fig. 2(a)). It can not be definitely established whether the difference between the values of  $\theta$  for the bursts of figures 7(a) and 7(b) represents scatter due to errors of measurement or whether it is caused by the difference in body shape between the straight tube and the pencil model. A source of error in the experimental technique, which stems from the fact that two sources of light are used to produce the two shadowgraphs from which these plots are made, could slightly distort the observed burst plan form and may account for all or part of this difference. Although care is used to initiate at the same instant the sparks which form these light sources, it is known that a time difference of a few microseconds can exist between exposures. Because of the motion of a burst with respect to the model, such a time difference in effect can cause a parallel shift of alternate meridians in the plot - hence distortion of the plan form. The maximum possible shift which could occur in the plots of figure 7 is calculated to be about 3 or 4 percent of the length of the models. A shift of this magnitude would be enough to obscure the indentation in the upstream end of the plan form of figure 7(a), and enough to account for appreciable variation in  $\theta$ . The possibility of the difference in  $\theta$  between the plan forms of figures 7(a) and 7(b) being due to body shape is discussed later in this section.

A characteristic of transverse burst growth in low-speed flow noted in reference 5 is that, after a burst is initiated, it moves downstream a short distance before transverse spread begins, after which the transverse growth proceeds at a constant rate. To obtain a measure of the transverse growth of a burst on a purely cylindrical model such as the straight tube, straight lines may be drawn passing through the point at which transverse growth begins and tangent to the burst plan form. For a burst with constant transverse growth rate, the lines thus drawn form its growth envelope. Since neither the point of beginning of transverse growth nor the constancy of the transverse growth rate could be directly established from the present data, it was necessary to make the best assumptions possible with the available knowledge. It was shown in reference 5 that a lag in the transverse growth of a burst in low-speed flow occurs at Reynolds numbers below approximately 450 based on the displacement thickness of the laminar boundary layer. This is the Reynolds number below which complete stability is predicted on the basis of small perturbation theory. Similar delays in the transverse spread of turbulence in supersonic flow at  $M = 5.8$  are observed in the data of reference 12. In the latter case, however, the displacement-thickness Reynolds numbers for commencement of transverse spread are of the order of 10 to 20 times the critical value of 450 for low-speed flow. For the test conditions under which the bursts of figure 7 were observed, values were calculated of the distance,  $r_0$ , from the burst origin to the point at which transverse spread begins, corresponding to displacement-thickness Reynolds numbers

of 450 and 4500. These values of  $r_0$  were, respectively, 0.04 inch and 4 inches. The latter value clearly does not fit the conditions of figure 7 since all of these bursts were observed at positions less than 4 inches from their points of origin. From an inspection of burst waves and burst positions in a number of the shadowgraphs it appears that a value of  $r_0$  as large as 0.5 inch, or half the nose length of the pencil model, is possible. Therefore, for the present case  $r_0$  was taken to have a value between 0.04 inch and 0.5 inch. A constant rate of transverse contamination of the laminar boundary layer by turbulence from a continuous source has been observed in subsonic flow (refs. 5 and 13) and supersonic flow (ref. 12) as well as for an individual burst in subsonic flow (ref. 5). It is assumed here, therefore, that the same behavior is characteristic of an individual burst in supersonic flow. (The validity of this assumption appears to be in doubt with regard to bursts on the pencil model.)

Based on these considerations, two growth envelopes are drawn for the burst of figure 7(a), with the burst origin being at the leading edge of the cylinder. These envelopes correspond to the assumed limiting values of  $r_0$ . The envelope corresponding to  $r_0 = 0.04$  inch subtends a half-angle,  $\alpha$ , of  $11^\circ$ . For the envelope corresponding to  $r_0 = 0.5$  inch,  $\alpha$  is equal to  $12-1/2^\circ$ . In the case of the hollow tube, then, the uncertainty in  $\alpha$  due to the uncertainty in  $r_0$  is no more than the probable error of measurement. Contrary to what might be expected, the average value of  $\alpha$  of  $11.8^\circ$  agrees more closely with the  $11.3^\circ$  for low-speed flow reported in reference 5 than with the angle of  $5^\circ$  for transverse spread of turbulence from a continuous source at Mach number 5.8 reported in reference 12. Unfortunately, in the present case, the value of  $11.8^\circ$  is the result of measurement from only one burst plan form which may or may not be representative for the present flow conditions. On the basis of the variation encountered in similar measurements obtained from a larger number of bursts on the pencil model, however, it is not expected that other measurements of  $\alpha$  for bursts on the hollow tube would differ by more than about  $\pm 2^\circ$ . It should perhaps be pointed out that an important difference between the test conditions of reference 12 and those of the present results was in the rate of convective heat transfer. The surface of the plate of reference 12 was at recovery temperature, while the surface of the hollow tube was at free-stream static temperature. It is not unlikely that the heat-transfer conditions would have an important effect on the rate of transverse growth of a burst, as well as on the point at which transverse growth starts.

On a flat plate the transverse spread of turbulence is found to be constant in a direction normal to streamlines. If this condition applies also on the ogival nose of the pencil model, on which the streamlines diverge, it is clear that the growth envelope must curve as it crosses surface streamlines (meridians when the model is not pitched) in order to make a constant angle,  $\alpha$ , with each local streamline. If the ogival nose is approximated by its inscribed cone, which may be developed together

with the body cylinder, the envelope curve on the developed conical nose is described by a logarithmic spiral. On the developed body cylinder it becomes a straight line. A growth envelope which meets these conditions is drawn for the burst of figure 7(b). In this case the uncertainty in  $r_0$  has a greater effect on the determination of  $\alpha$ . For this plan form, when  $r_0 = 0.04$  inch,  $\alpha$  is calculated to be  $3.0^\circ$ ; when  $r_0 = 0.5$  inch,  $\alpha$  is  $6.1^\circ$ . Thus, the uncertainty in  $r_0$  introduces an uncertainty in  $\alpha$  of the order of magnitude of  $\alpha$  itself. These values of  $\alpha$  are considerably lower than that found for the burst on the straight tube (fig. 7(a)) and would seem to indicate a lower rate of transverse growth on the pencil model than on the straight tube. This result also appears to be consistent with the comparative slenderness exhibited by the two bursts of figures 7(a) and 7(b). On the other hand, from the geometry of the growth envelope in figure 7(b) it can be seen that while the burst is on the model nose its rate of transverse spread with respect to its own plane of symmetry increases as the burst moves downstream. For a constant longitudinal growth rate, then, the burst plan-form shape would not remain similar as it grows, but would become less and less slender as it moves downstream. The low values of  $\alpha$  obtained for the plan form of figure 7(b), therefore, do not appear to explain its relative slenderness in comparison with that of figure 7(a). A possible reason for this relative slenderness is found from examination of figure 7(c).

In all, it was possible to define, with varying degrees of precision, eight burst plan forms: one from shadowgraphs of the straight tube (fig. 7(a)) and seven from shadowgraphs of the pencil model, including that of figure 7(b). Figure 7(c) is a composite of this group of plan forms superimposed on a single meridian. Each outline is positioned on the figure at the observed longitudinal position. The dotted lines represent the lateral extremities of the developed cylinder of the pencil model. They indicate the limit of transverse growth which a burst can undergo on this body before the edges of the burst begin to merge with each other on the opposite side of the body. Comparison of the seven plan forms from the pencil model with these dotted lines suggests that on the body cylinder of this model little or no transverse growth takes place, but that longitudinal growth continues. It will be observed that the plan forms farthest from their point of origin are the most slender while the two nearest the origin are the least slender and compare most closely in shape with the plan form from the straight tube. The values of  $\theta$  for the seven plan forms vary from  $18^\circ$  for the first two to  $10^\circ$  for the two farthest back. For the first plan form the half-angle,  $\alpha$ , of the growth envelope is  $4.3^\circ$  when  $r_0 = 0.04$  inch and  $12.7^\circ$  when  $r_0 = 0.5$  inch. This latter value of  $\alpha$  and the value of  $\theta$  of  $18^\circ$  for this plan form are nearly identical to the values for these angles measured on the plan form from the straight tube. While remembering that figure 7(c) is a composite of several bursts observed on several models, one can visualize that these plan forms represent successive positions of a single burst moving downstream. It appears, therefore, that a burst originating at the tip of the pencil model grows transversely while on the nose, at a rate approaching that measured for the



straight tube, but for some reason stops, or nearly stops, its transverse growth upon reaching the body cylinder. With such sketchy evidence, of course, it is not certain that this indicated growth behavior actually occurs, nor is it clear why transverse growth on the body cylinder should slow down or stop. The large lateral curvature of the body surface may be a factor. The possibility of upwash effects due to slight pitching of the models in flight was investigated and found to be negligible. The relations of the burst center lines to the pitching planes of the models were entirely random, and no correlation was found between the relative position of a burst on the model body and its relative width. This is not to say that no effects of upwash are to be expected. The angles of pitch of the models for which data are presented in table I and figure 7 were all small -  $1^\circ$  or less. On other models at higher pitch angles a definite effect of upwash on burst thickness and length was observed.

From the evidence available it does appear that for a burst on a slender body such as the pencil model, both  $\theta$  and  $\alpha$  vary with distance of the burst from its point of origin, tending to become smaller as the burst moves downstream.

Figure 7(d) illustrates the type of burst distribution most often encountered on the hollow-tube models. This figure is plotted from measurements made on the shadowgraphs of figures 4(j) and 4(k) which do not adequately define the outlines of the many small or partially merged bursts. A considerable degree of artistic license is required in the fairing of figure 7(d); however, the figure does serve to portray the intermediate step in the transition process between the formation and initial growth of isolated bursts and their eventual merging to form a continuum of turbulent boundary layer. Related observations of burst formation and growth made throughout this study have tended to substantiate at least the general features of the model of boundary-layer transition hypothesized by Emmons and Bryson in reference 4.

### Three-Dimensional Burst Shape

The two bursts of figures 7(b) and 7(a) were defined in sufficient detail to permit three-dimensional representation. Contour maps of the developed plan forms of these bursts are presented in figures 8 and 9, respectively. The profiles from which the elevations were taken are also shown. These profiles were determined by the second method described in the section "Burst Thickness Profiles." The number of profiles in figure 8 and their disposition with respect to the plan form indicates the degree of accuracy of the contour map. As discussed previously, the true elevation of the zero contour is somewhat in doubt, but it is known to be approximately equal to the laminar boundary-layer thickness. The relationship of the contours among themselves, however, is well defined. The contour interval is 0.010 inch. The sides of the burst are seen to rise steeply from the surface to a V-shaped ridge whose legs run parallel to

the side edges. The upstream end of the burst rises much more gradually and funnels into a valley which is bounded by the V-shaped ridge. The back of the ridge then slopes downward toward the downstream end of the burst. The highest elevation is 0.053 inch (above the zero contour) at a point above the  $\phi = 0$  meridian. A short distance downstream of this point is another smaller peak. In the shadowgraphs these peaks are seen to be the heads of relatively large eddies which protrude above their neighbors. Similar peaks appear in the contour map of figure 9. Exclusive of the local peaks, the highest elevation occurs at a point in the center plane about 70 percent of the burst length from the upstream edge. It is now apparent that the indented shape so characteristic of the upstream end of a burst plan form is simply the beginning of the central valley of the burst. The formation of this valley may be due to the fact that the burst, being much thicker than the surrounding laminar boundary layer and moving more slowly than the stream, is subjected to a dynamic pressure from the stream which forces a pocket into the upstream slope of the burst much as it would do to a water droplet on a solid surface. Because only two profiles of the burst of figure 9 were available, it was necessary to assume a general similarity to the contour shape of figure 8 in order to complete the fairing. It can be seen, however, that any radically different symmetrical and internally consistent fairing would be difficult to devise. It may also be observed that while indentation of the upstream end of the burst is not shown at the zero elevation, it is present in the contours of higher elevation. A small shift to the right of the  $\phi = 85^\circ$  meridian profile, which might be justified, as mentioned earlier, by the possibility of a small difference in time of the spark discharges, would result in an indented upstream edge and a somewhat more slender plan form.

Before leaving the subject of burst shape it is of interest to note the similarity of shape between the thickness profiles at different meridian positions in both figures 8 and 9. Thickness distribution is shown to be virtually independent of both the length of the profile and its meridian position. The effect of this similarity is of course reflected in the three-dimensional shape of the burst. This characteristic also permits the profiles of figure 5 to be properly compared even though their meridian positions are not precisely known.

#### Burst Upstream-Edge Velocity

The velocity and longitudinal growth characteristics of the bursts on these models were determined, as previously outlined, by obtaining upstream-edge velocity, and ratio of burst length to distance moved, directly from the data, and then using equation (4) to calculate the downstream-edge velocity. The determination of these variables and their dependence on some of the environmental conditions are discussed in this and the two following sections. Measured values of these variables, together with the corresponding flow and surface roughness conditions, are tabulated in table I.

In measuring wave angles from which to determine  $M_1/M_e$ , it was found that reasonably good repeatability was obtained even with some of the more obscure shadowgraphs. The maximum error was estimated to be  $\pm 2^\circ$ , which at the highest Mach numbers corresponds to an uncertainty in  $M_1/M_e$  of about  $\pm 0.05$ . The uncertainty in most of the measurements, however, is believed to be no more than half of this figure.

Effects of Mach number and Reynolds number.— Values of  $M_1/M_e$  are plotted in figures 10(a) and 10(b) against local Mach number,  $M_e$ . Data for the quasi-two-dimensional flow on the hollow tubes, together with the low-speed results from references 5 and 10, are shown in figure 10(a). Data for flow on the pencil model, and the result from reference 4, are shown in figure 10(b). The data for the pencil and tube models are all for a reasonably restricted range of Reynolds number per unit length. The data from references 4, 5, and 10 are for lower values of Reynolds number per unit length. Values of  $M_1/M_e$  obtained on relatively rough surfaces are distinguished from those obtained on smoother surfaces by the solid symbols. (The measure of roughness will be discussed in the following section.) Values of  $M_1/M_e$  are seen to be systematically increased by surface roughness. Straight lines are faired through the data to indicate trends. The dashed lines indicate 20-percent deviation from the trend lines. There appears to be a significant effect of Mach number on the rate at which the upstream edge of a burst moves downstream.

Three sets of data points from the hollow tubes and the A-4 model permit an estimate to be made of the effect of Reynolds number on  $M_1/M_e$ . Figure 11 shows these data plotted with Reynolds number per unit length, or "unit Reynolds number,"  $U_e/\nu$ , as the independent variable. Each set of data was obtained from models of similar roughness. The Reynolds number trend indicated for the straight tube when  $M_e \approx \text{constant}$  (the solid lines) is one of increasing  $M_1/M_e$  with increasing unit Reynolds number. This trend is defined by only four data points and is considered to be only qualitative. Two sets of data (the dashed lines) show the effect of simultaneously increasing unit Reynolds number and Mach number. The Mach number effect is seen to be stronger than the simultaneous Reynolds number effect. It appears significant, however, that if these two sets of points are plotted against  $M_e$ , the indicated trends of  $M_1/M_e$  with  $M_e$  have slopes which are less negative than those shown in figure 10. This result supports the trend indicated in figure 11 by the solid lines. It can be tentatively concluded that the gross effect of Reynolds number on  $M_1/M_e$  is one of increasing  $M_1/M_e$  with increasing  $U_e/\nu$ , and the gross effect of Mach number is one of decreasing  $M_1/M_e$  with increasing  $M_e$ .

Effect of surface roughness.— Fortunately, the surface conditions on the hollow tubes and on the pencil model were carefully controlled and quantitatively measured. It was thus possible with these models to examine the effects of distributed surface roughness on  $M_1$ . The types of roughness used consisted either of a fine continuous screw thread or of a

circumferentially or longitudinally applied scratch polish. A detailed description of these surfaces is contained in reference 8. The roughness dimension was taken as the maximum peak-to-valley distance,  $H$ , of the screw thread or scratch cross section. Within this group of models, values of  $H$  varied between 10 microinches for the smoothest surface to 2100 microinches for the roughest. The nondimensional parameter  $(H/\delta)\sqrt{R_x}$  proposed by Seiff was used to correlate the roughness data. The ratio  $\delta/\sqrt{R_x}$  is independent of  $x$  for laminar flow on a flat or conical surface, so that the use of this parameter has the advantage of eliminating  $x$  as an implicit variable in correlating the effects of distributed (uniform) roughness on such surfaces. The parameter  $(H/\delta)\sqrt{R_x}$  may be put into the form  $R_H/c$ , in which  $R_H$  is the Reynolds number based on  $H$  and  $c$  is the nondimensional laminar boundary-layer thickness defined by Van Driest (ref. 11). This form is more convenient for use. For the purpose of figure 10, models having  $R_H/c$  greater than 120 were considered to have relatively rough surfaces. Data from these models are plotted with the solid symbols. The effect of surface roughness on burst upstream-edge Mach number is shown in figure 12, where  $M_u/M_e$  is plotted against  $R_H/c$  for the tube models and the pencil model. Lines are faired through the data points in each Mach number group. The solid lines indicate the trend of  $M_u/M_e$  with  $R_H/c$  for the tube models; the dashed lines indicate this trend for the pencil model. The variation of unit Reynolds number among these data is relatively small and so should not contribute significantly to the trends observed. At Mach numbers between 2.7 and 4.1 surface roughness has a marked influence on the burst upstream-edge Mach number. As might be suspected intuitively, the effect of increasing roughness is to reduce the velocity at which a burst passes over the surface. At higher Mach numbers the effect of roughness appears to decrease.

With the limited number of data available which will permit consideration of one variable at a time, very little further improvement of these correlations is possible. However, for a value of the roughness parameter,  $R_H/c$ , of 150 a cross plot of the curves faired through the data of figure 12 can be made which indicates the improved correlation of  $M_u/M_e$  with Mach number effected by consideration of the roughness variable, and shows more clearly the strong Mach number dependence of burst upstream-edge velocity when roughness is present. Such a cross plot is shown in figure 13. (The curves for the two-dimensional surfaces is based on the data from both the contoured tube and straight tube, and is therefore marked with the double symbol.) It is seen that this curve and the corresponding curve from the pencil-model data, which are plotted for the same roughness condition, have virtually the same slope and indicate a nonlinear variation of  $M_u/M_e$  with  $M_e$ .

The data for the A-4 model, on which roughness was small, is included in the figure for comparison. While  $U_e/v$  increases with  $M_e$  for these data, the large difference in slope at the lower Mach numbers between the

curve for the A-4 and the other curves does not appear to be entirely due to this variation. Difference in body shape is not considered to be a factor since the slopes of the pencil-model and tube-model curves are nearly the same, and the pencil-model and A-4 bodies differ in shape only in the fineness ratio of the nose. However, a relatively large difference in surface roughness existed between these models. The comparison suggests that these curves are members of a family of curves, the initial slopes of which depend on the value of  $R_H/c$  and which converge with increasing Mach number, becoming asymptotic to some constant value of  $M_u/M_e$ . At the low Mach number end of the spectrum, it may be conjectured that the curve corresponding to some critical value of  $R_H/c$  will intersect the  $M_e = 0$  axis at  $M_u/M_e = 1$ , and that for lower values of  $R_H/c$  the curves will intersect the  $M_e = 0$  axis at lower values of  $M_u/M_e$ . Curves corresponding to increasing values of  $R_H/c$  above the critical will then intersect the line  $M_u/M_e = 1$  at increasing values of  $M_e$ . Data from references 4, 5, and 10 which are also plotted in figure 13 appear to be consistent with the above interpretation of the curves of this figure.

#### Burst Longitudinal Growth Rate

Practical use of the method previously outlined for locating points of burst origin leaves much to be desired in the way of precision. Uncertainties arise from numerous causes. Wave ends are not clearly defined and it is sometimes difficult to distinguish between a truly oblique wave and an impulse wave from a turbulence eddy. Attenuation of initial wave segments in an expanding flow field and deterioration of wave strength with time, together with the sensitivity limitations of the shadowgraph, can result in the visible wave end not corresponding to the initial position of its source. The burst must grow to finite size before it can form a shock wave of visible strength. Allowance must be made for the curvature of Mach lines in the flow fields of curved bodies. Most of the uncertainties encountered result in potential errors which are systematic in causing points of burst origin located by this method to lie aft of their true locations. It was significant, therefore, that almost without exception, measurements on this large group of shadowgraphs showed the points of burst origin to lie close to the leading edges of the models. On the contoured tubes and pencil models projections of the burst wave ends most often intersected the body profiles at the nose-body juncture, or shoulder; on the straight tubes the great majority of the projections intersected the body profiles within a body diameter of the leading edge; and on the cones the burst wave ends invariably coincided with the bow wave, indicating the cone apex to be the burst source. Indeed, on the pencil model evidence of burst formation well forward of the shoulder was observed in a number of shadowgraphs (cf. figs. 4(q), 4(s), and 4(u)). These findings strongly suggest that all of the bursts originated at the leading edge, or tip, but moved downstream an appreciable distance before

reaching a size sufficient to produce visible shock waves. Since a burst remains quite thin before it begins to grow transversely, it is not unlikely that the distance a burst moves before producing a shock wave is equal to  $r_0$ . As a result of these considerations it was concluded that the bursts on all of the models studied in this analysis originated at the leading edge, and measurements of  $x_u$  were made from this point.

With the exception of measurements made on the plan forms of figure 7(c), accurate measurements of burst length,  $L$ , were hampered because the proximity of the burst center line to the plane of the shadowgraph, or silhouette plane, could not be reliably determined. In consequence, a potential systematic error in  $L$  of negative sign existed, which could affect values of  $L/x_u$ . Considerable scatter is present in the data presumably, in part at least, from this cause.

Effect of Mach number.— Experimental values of  $L/x_u$  are plotted against local Mach number,  $M_e$ , in figure 14. The large scatter in  $L/x_u$  is apparent as is the poor distribution of the data with respect to  $M_e$ . The fact that these data are for models of different roughness contributes to the scatter in this figure. Note, however, that the solid symbols, which represent data from the plan forms of figure 7(c), show less scatter than do the rest of the data. An upper bound for  $L/x_u$  can be obtained from equation (4) by setting  $M_d/M_e$  equal to zero (downstream end of the burst moving at stream velocity) and substituting the value of  $M_u/M_e$  from figure 12 or 13. Limiting curves of  $L/x_u$  versus  $M_e$  are shown in figure 14 for the two-dimensional and three-dimensional surfaces for  $R_H/c$  equal to 150. All of the data points fall below their respective limiting curves and, in spite of the scatter, appear to substantiate the Mach number trend indicated by the curves.

Examination of equation (4) shows that  $L/x_u$  must follow the same general trend with respect to Mach number and surface roughness as does  $M_u/M_e$ . This means that the  $L/x_u$  data of figure 14 should correlate to a family of curves in a manner similar to that postulated for figure 13. Also,  $L/x_u$  should correlate on the basis of surface roughness in a fashion similar to that of figure 12. The poor distribution of the variables in the existing data precludes any refinement of figure 14. The situation with regard to surface roughness, however, is somewhat better.

Effect of surface roughness.— Figures 15(a) and 15(b) show the effect on  $L/x_u$  of varying surface roughness on the tube models and on the pencil model, respectively. Curves are faired through the data points for the tube models at mean Mach numbers of 3.7 and 6.7, and through the data points for the pencil model at a mean Mach number of 3.7. Limiting curves for  $M_e = 3.7$  based on equation (4) and figure 12 are also shown in each figure. A comparison of the plots of figures 15(a) and 15(b) with that

of figure 12 shows that  $L/x_1$  exhibits the same trends with respect to surface roughness, surface shape, and Mach number, as does  $M_d/M_e$ . On the basis of equation (4), therefore, the two sets of data are mutually consistent.

#### Burst Downstream-Edge Velocity

For a very few specific Mach number and surface roughness conditions, paired data are simultaneously available from figures 12 and 15 which can be used to calculate burst downstream-edge Mach number by substitution into equation (4). Values of  $M_d/M_e$  obtained in this manner are plotted against local Mach number,  $M_e$ , in figure 16(a), and against roughness parameter  $R_H/c$  in figure 16(b). Due to the uncertainties involved in defining and in locating the downstream end of the burst in the shadowgraph, it cannot be said whether these values of  $M_d/M_e$  apply at the point of maximum advance, as defined by Schubauer and Klebanoff (see fig. 2(a)), or at some point a small distance upstream of it. The sign of the potential systematic error associated with locating the downstream end of the burst in the shadowgraph would seem to favor the latter. In addition, due to the potential errors encountered in determining  $L/x_1$ , the probability of overestimating  $M_d/M_e$  is greater than the probability of underestimating. Hence, the calculated values of  $M_d/M_e$  may be more nearly correct for a point of small distance upstream than for the point of maximum advance.

The values obtained with minimum surface roughness are about the same as those which were measured in low-speed flow. Surface roughness conditions were not reported for the low-speed tests; but when the comparative scales involved are considered, it seems probable that the roughness parameter,  $R_H/c$ , for those tests would approximate the lowest values encountered here. The variation of  $M_d/M_e$  with Mach number and surface roughness follows qualitatively the same trends as does  $M_u/M_e$ . The ratio decreases with increasing Mach number and increases with increasing surface roughness. In terms of motion with respect to the surface, the burst velocity increases as the stream velocity increases but decreases as surface roughness increases.

#### Burst Formation Rate

Since bursts are being continuously swept downstream by the main flow, the number of bursts distributed over the surface and the distance they must travel before merging into a continuously turbulent boundary layer are dependent upon the rate at which the bursts are formed. The shadowgraphs were examined from this point of view and found to yield some

interesting results in regard to the frequency of burst formation. Before presenting these results it is of interest to consider the significance of the observed wave spacing from the standpoint of the shadowgraph itself.

It may be observed in many of the shadowgraphs of figure 4 that the spacing of the burst waves tends to be regular. A regular spacing implies a periodic discharge of bursts from a body-fixed source. Moreover, the fact that such a phenomenon can be clearly seen in the shadowgraphs indicates that, at least in these tests, burst sources are not randomly disposed over the surface for if they were, even though all sources were discharging at the same frequency, random phase relationships would result in the appearance of randomly spaced waves. Therefore, all burst sources must be located at the same body station. It already has been concluded that this station is the leading edge.

Once the location of burst sources has been restricted to the leading edge, the appearance of regular wave spacing in the shadowgraphs further indicates that one (or both) of two situations must exist: (1) Formation of bursts at sources distributed on the leading edge must occur in synchronism or with harmonic phase relationship (phase shift equal to an integer fraction of the period); or (2) the shadowgraph itself must effectively filter out the waves of bursts whose sources or center lines are not close to the plane of the silhouette. In the case of the hollow tube, there is evidence, of the type shown in figure 7(d), that the burst spacing tends to be regular along meridians, but random in a lateral direction, and that synchronism does not occur between adjacent sources. On the other hand, there is evidence that on the pencil model more than one source can exist at the tip and that the discharge of bursts from these sources is harmonically phased. From an intuitive viewpoint, one can more easily conceive of a harmonic phase coupling between sources in very close proximity, such as on the apex of a pointed body, than between sources which are distributed along a two-dimensional leading edge. That there can be multiple sources at the tip is indicated in several of the shadowgraphs in which waves associated with different bursts can be seen moving along opposite meridians (cf. figs. 2(b), 4(s), and 4(t)). That there might be synchronism between these sources was strongly suggested by a few plan-form plots similar to those of figure 7 in each of which was observed the presence of two bursts of nearly equal size and at nearly the same station but on opposite sides of the body. This was interpreted to mean that the two bursts originated at the same instant at two different sources. Indications of synchronism are found in figures 2(b), 4(r), and 4(x), in which the paired burst waves are known from plan-form plots to be associated with different bursts.

As to the effectiveness of the shadowgraph in filtering out the waves of bursts whose center lines are not close to the plane of the silhouette, it is clear that if the plane of symmetry of the wave envelope is allowed for the moment to rotate about the body axis in a direction away from the plane of the silhouette, the light rays of the shadowgraph will pass tangent to progressively weaker elements of the wave envelope and hence



encounter smaller density gradients. The sensitivity of the shadowgraph to a burst wave of given strength would thus decrease as the plane of symmetry of the wave departed from the plane of the silhouette. It will be remembered, however, from the transverse growth characteristics of a burst that, after having moved a certain distance downstream from its source, a burst will completely (or nearly so) encompass the model. Based on figure 7, this distance is estimated to be about 70 percent of the body length for the tube models and between 25 and 50 percent of the body length for the pencil model. Therefore, a burst moving along any meridian on the body will have intersected the silhouette plane at least by the time it has moved 35 percent of the body length on the tube models, or 12-1/2 to 25 percent of the body length on the pencil model. Downstream of these stations it could be expected that the shock waves of all bursts would begin to appear, but with intensities decreasing with the distance of the burst center lines from the plane of the silhouette, and increasing with the distance downstream. These characteristics are exhibited to more or less degree in many of the shadowgraphs. The variation of apparent wave intensity with distance of the burst center line from the plane of the silhouette is particularly well illustrated by the burst wave of figures 4(d) and 4(e). The two shadowgraphs are orthogonal views of the same wave at the same instant. In figure 4(d) the center line of the burst is approximately 15° from the plane of the silhouette. In figure 4(e) the center line of the burst is approximately 75° from the plane of the silhouette. In the second figure the shock wave appears much weaker than in the first.

From the foregoing discussion it may be concluded that the majority of the waves observed on a given side of the body in any particular shadowgraph belong to bursts all of which originated at the same source located at the leading edge or tip. The wave spacing is therefore a measure of the frequency of burst formation at that source. To be sure, some of the waves are undoubtedly those of bursts which originated at other sources which, in turn, may or may not be harmonically phased with the first. To weight properly such uncertainties, as well as those arising from "accidental" variation of wave spacing, the frequency data were treated in a statistical manner. Measurements of wave spacing were made on the 19° included-angle cone, pencil model, and hollow cylinders.

In terms of the wave spacing,  $\lambda$ , the frequency,  $f$ , with which bursts are formed at a source is given by

$$f = \left(1 - \frac{M_u}{M_e}\right) \frac{M_e a_e}{\lambda} \quad (5)$$

where  $\lambda$  is measured along a streamline. Frequencies were calculated, using equation (5), for as many wave spacings as could be found in order to provide as many observations in each statistical sample as possible. The attempt was made to separate the effects of such variables as Mach number, Reynolds number, surface roughness, and leading-edge bluntness

by choosing each sample in such a way that all variables but one were as nearly constant as possible. This of course necessitated a compromise between the desire to keep the limits of parameter variation reasonably small and the necessity of keeping the sample reasonably large.

The data of each sample were tabulated in terms of the burst formation frequency,  $f$ . The optimum class intervals,  $\Delta f$ , were determined by trial and were taken to be 50 kilocycles per second for the data from the  $19^\circ$  included-angle cone, and 10 kilocycles per second for data from the pencil model and hollow tubes. It was found that by making two tabulations for each sample, using the same class interval for both but shifting the class boundaries for the second tabulation by one-half of the class interval, the same data could in effect be used twice to obtain better definition of the frequency curves. The results are presented in the form of frequency spectrums in figures 17, 18, and 19 for the cone, pencil model, and hollow tubes, respectively. The ordinate,  $n\Delta f/N$ , which might be termed the "frequency probability," is the ratio of the number of observations within a class to the total number of observations in the sample. The value of  $N$  for each curve is noted in the figure. The plotted points show the value of  $n\Delta f/N$  at each class mark, there being two points for each interval because of the double tabulation.

The general characteristics exhibited by these curves are a number of favored frequencies which bear harmonic relationship, with the fundamental frequency usually being the most favored, that is, having the highest frequency probability. The presence of the harmonics, particularly numerous for the pointed bodies, lends further support to the concept of harmonically phased multiple sources at the tip. In the case of the hollow tubes the presence of harmonics, much less prominent relative to the fundamental than those for the pointed bodies, is more likely to mean multiple-frequency burst discharge from a single source. This of course could occur also on the pointed bodies in conjunction with multiple-source discharge. However, the data are incapable of resolving the one condition from the other.

The curves of figures 17, 18, and 19 have been examined to determine the qualitative effects on burst formation frequency of a number of variables.

Effect of Mach number.- In figure 17(a) curves are drawn for two Mach number ranges at an essentially constant unit Reynolds number of approximately  $3 \times 10^6$  per inch. The average Mach number for the solid curve is approximately 4, and for the dashed curve is approximately 5. The effect of an increase in Mach number from 4 to 5 is seen to be small. However, there does appear to be a small net shift to higher frequencies, with new harmonics appearing at 600 and 700 kilocycles per second.

Effect of Reynolds number.- The effect of varying the Reynolds number is shown in figures 17(b) and 18. In figure 18, for an average Mach number of about 3.7 on the pencil model, the effect of approximately doubling the

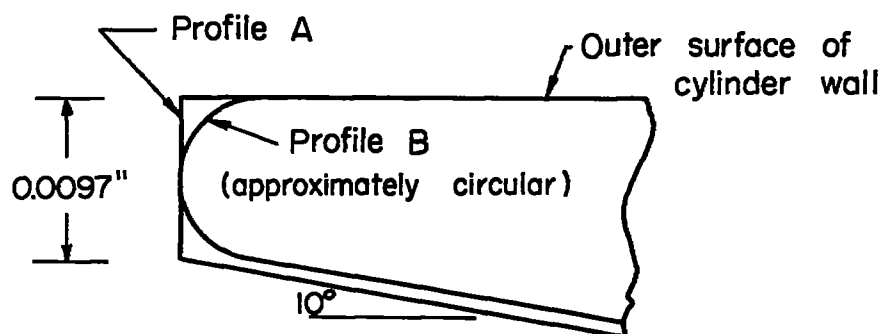
unit Reynolds number from roughly  $2.1 \times 10^6$  per inch to  $3.8 \times 10^6$  per inch is seen to increase the fundamental frequency of burst formation by roughly 40 percent and to produce a number of harmonics. Similar results are shown for the cone data in figure 17(b). Some variation of Mach number is present in these data as is indicated in the figure. However, the effect of Mach number variation in this range is shown to be small in figure 17(a). The appreciable increase in frequency of burst formation with the simultaneous increase in Mach number and unit Reynolds number shown in figure 17(b) can therefore be attributed primarily to the Reynolds number increase. It is seen that roughly a two and one-half fold increase in  $U_e/\nu$  produced a two and one-half fold increase in the fundamental preferred frequency of burst formation. It will be observed that the effect of increasing  $U_e/\nu$  from  $2 \times 10^6$  per inch to  $3 \times 10^6$  per inch is characterized by an increase in the number and prominence of harmonics with no change in the frequency of the fundamental, while the effect of increasing  $U_e/\nu$  from  $3 \times 10^6$  per inch to  $5 \times 10^6$  per inch is characterized by a large increase in the frequency and frequency probability of the fundamental and a reduction in the number of harmonics. The reason for this behavior is not clear.

Effect of surface roughness.— The effect of surface roughness could not be explicitly determined. Variation of surface roughness is present to more or less degree in all of the data, although data from the roughest models were excluded from the samples. The largest variation in roughness height,  $H$ , from 10 to 600 microinches, or 4 to 195 in terms of  $R_H/c$ , occurred in the hollow-tube data. In these data no correlation between formation frequency and roughness could be found. The relation of frequency to roughness appeared to be purely random. This result was to be expected in view of the fact that burst sources situated at the leading edge could not be influenced by roughness downstream. Had burst formation frequency been affected by surface roughness, the curve of figure 19 would have been much less distinctly defined.

Effect of leading-edge geometry.— For approximately the same conditions of Mach number and unit Reynolds number the fundamental frequencies of burst formation differ between the three model types. For an average Mach number of about 3.5 and an average unit Reynolds number,  $U_e/\nu$ , of about  $2 \times 10^6$  per inch, the favored fundamental formation frequencies on the cone, the pencil model, and the hollow tube are 115, 20, and 11 kilocycles per second, respectively. The high frequency of formation on the cone as compared to that on the pencil model might seem at first surprising since the flow conditions were nearly the same in the two sets, and the apex geometry does not differ greatly between the cone and the ogive - at least in a macroscopic sense. However, this large difference in frequency serves to emphasize that since the bursts originate at the model tip, their rate of discharge can be strongly influenced by the local geometry of the tip. This fact was noted in reference 8, and it was observed there that the greatest number of bursts were produced by abrupt changes in slope of the tip profile. These conditions appear to have been responsible for the

relatively high rate of burst formation on the cones of reference 7 as well. An examination under the microscope was made of the tips of some of the unfired cone models left over from the tests of reference 7. These models were well preserved, and no evidence of corrosion or physical damage during storage could be detected. Marked irregularities in tip profile were observed. Photomicrographs of two such tips, which are believed to be representative of those used in the tests, are compared in figure 20 with the typical tip profile of the pencil models on which burst formation frequencies were measured. The roughly truncated shape shown in figure 20(a) was a frequently observed characteristic of these models. Tips such as this provide conditions conducive to local flow separation or the production of large transverse entropy gradients, either of which could induce turbulent eddy formation. In the course of testing in the Ames supersonic free-flight wind tunnel it has been observed generally that a slight truncation of the tip of a pointed model produces numerous bursts. On the other hand, a careful rounding of the tip profile to eliminate abrupt changes in slope is found to result usually in relatively low frequencies of burst formation. It was noted in reference 7 that fewer bursts were observed on the blunted models than on the cones. The pencil model on which the burst of figure 8 was observed had an approximately hemispherically blunted tip, the radius of which was equal to 20 percent of the body radius. The burst formation frequency on this model was too low to be measured.

The same qualitative effect of leading-edge geometry observed on the pointed bodies was also observed for the two-dimensional leading edge. A rather spectacular demonstration of the influence of leading-edge geometry was made during the tests on the hollow-cylinder models. Two models of the straight tube, identical except for leading-edge geometry, were fired at a Mach number of 3.9 in still air. The leading-edge profiles of these models are shown in the sketch. Profile A had a flat forward facing



surface with a sharp  $90^\circ$  corner to the outer surface of the cylinder. To produce profile B, this corner was rounded off to give an approximately circular profile tangent to the outer and inner surfaces of the cylinder. With profile A, the burst formation frequencies varied between 30 and 100 kilocycles per second. With profile B, the maximum frequency was less

than 5 kilocycles per second. Figures 4(c) and 4(d) are shadowgraphs of these models having profile A and profile B, respectively. Data from these models were not included in figure 19.

#### Further Observations From the Shadowgraphs

Aside from the characteristics of burst shape and formation and growth discussed in the foregoing sections, many other features of burst behavior could be observed in various shadowgraphs. Taken individually these observations would not perhaps provide any evidence of startling significance. Considered as a whole, however, they all tended to support further the concept of boundary-layer transition as it is presently understood and, in a few cases, to supply additional details.

For example, one can infer something about the velocity history of the upstream edge of a burst from the shape of its shock wave. Most of the isolated and well-defined burst shock waves on the hollow-tube models are nearly straight, indicating a nearly constant velocity for the upstream edge of the burst. This observation provides a basis for the assumption of constant velocity in postulating equation (1). There is some indication of a slight concavity in these waves (e.g., the wave on the lower profile of fig. 4(l)), suggesting the possibility that bursts slow down gradually as they increase in size. There is also an occasional wave which shows pulsations of some sort occurring at the upstream end of the burst. Such a wave is illustrated by the shock wave of the downstream burst on the lower profile of figure 4(a). This pulsing could be interpreted as a fluctuation in the velocity of the upstream edge, or as pulsing of a particularly large eddy, or eddies, located at the upstream edge of the burst. The frequency of the phenomenon was measured to be 40 kilocycles per second. Of course, one must use care in attempting to draw conclusions from wave shape since this shape can be affected not only by the velocity history of the burst upstream edge but also by pressure gradient or streamline curvature as the wave negotiates the outer flow field.

In many instances it is possible to determine at what point on the body surface a burst has been overrun by the downstream end of the following burst. When the upstream edge of a burst is overrun it ceases to be a shock-wave source; hence, the wave ceases to be formed and the inner end becomes a moving point of reference. Figure 4(k) is a good example of this situation. A pair of bursts on each profile of the body may be seen to have merged shortly before the shadowgraph was taken. The separate identities of the bursts are still apparent from their profiles. The points at which the downstream bursts were overrun can be approximately located by projecting the inner ends of their shock waves upstream along Mach lines. In a case such as that of figure 4(c) the transition region can be approximately defined by wave-end projection. Here the waves are

so closely spaced that the projection is readily visualized. The length of the transition region is found to be less than two body diameters. In contrast, the extent of the transition region on the body of figure 4(d) is seen to be greater than the length of the model. Comparison of these two shadowgraphs suggests that the rate of burst formation has a large influence on the extent of the transition region.

A phenomenon which was occasionally observed on the pencil model was the appearance of a circular shock-wave segment which intersected a burst shock wave at one end and came nearly tangent to the model bow wave at the other (see figs. 2(b), 4(r), and 4(t), for example). The circular nature of this wave and its position relative to the burst wave indicate that it must have been associated with an impulsive disturbance occurring at the time of formation of the burst. If a burst forms with an initial eddy, it appears that the formation of the eddy may be of an explosive nature. The impulsive discharge of an eddy from a local separated flow region at the model tip could be such a disturbance. That this circular wave was produced by such an eddy discharge is suggested by the similarity of shape between it and the circular (spherical) impulse waves emanating from eddies within bursts and within the fully developed turbulent boundary layer. For example, compare the circular waves in figure 2(b) with the impulse waves above the two bursts in that figure. Compare also the impulse waves above the turbulent boundary layer in figure 4(g).

An effect of angle of attack on burst growth is observable qualitatively in the shadowgraphs. In figure 4(x) the four prominent burst profiles were ascertained with reasonable, though not conclusive, certainty from a developed plan-form plot to be nearly center-line profiles of four independent bursts. The thicknesses of the profiles on the leeward side of the body are conspicuously greater than of those on the windward side. Further, it was found for the upstream pair that, although apparently initiated first, the windward burst was shorter than the leeward burst. Thus it appears that the combined effects of pressure gradient and upwash due to angle of attack influence the thickness and longitudinal growth of a burst. A favorable pressure gradient and diverging streamlines (windward side) tend to retard growth in both thickness and length, while an adverse gradient and converging streamlines (leeward side) tend to accelerate the growth. No conclusions could be drawn concerning the effects on transverse growth although it is clear that, if burst shape is to be preserved, the transverse growth rate must vary in proportion to the longitudinal rate. One is tempted to speculate, however, that the crossflow pressure gradient and upwash would tend to accelerate transverse growth on the windward side and retard it on the leeward side; that is, the effect on transverse growth would be opposite to that observed on longitudinal and thickness growth. If such were the case, then burst shape ( $\theta$ ) as well as  $\alpha$  would be a function of angle of attack, and bursts formed on the sides of a body would have nonsymmetrical plan forms.

Throughout the present study the growth and spread of turbulence, subsequent to burst formation, has been observed to be closely similar

to that reported in reference 5. The mechanism (or mechanisms) by which the formation of bursts is initiated, however, is still not understood. Perhaps a brief bit of conjecture is permissible concerning observations made during this study as they relate to this phase of the transition process.

When burst formation was observed to occur at the leading edge, the rate of formation was relatively very low and the transition region relatively very long. On the other hand, when burst formation was observed to occur at any downstream point on the body the rate of formation was very high and the transition region very short. Consequently, under the latter conditions discrete or developed burst profiles were never observed. Compare figures 4(c) and 4(d) with figure 4(y). In figure 4(y) the transition region on the upper profile is very short. The burst formation rate is so high and the life of an individual burst so brief that the spacing of their shock waves is close to the resolution boundary of the shadowgraph, and the waves appear as nearly circular (spherical) impulse waves.

Various sources of disturbance leading to flow breakdown can be hypothesized. Three of the more probable can be listed as follows:

1. Local flow separation at the leading edge or tip
2. Roughness elements at the leading edge or on the body surface
3. Görtler instability at the leading edge or along the body surface

It is presumed that for a model in free flight through still air, stream disturbances are nil. The large differences observed in the frequency of burst formation at the leading edge and at downstream points lead to speculation that differences exist in the disturbances which cause the transition. At the leading edge, burst formation may simply be eddy discharge from a separated region or from behind a roughness element at rates peculiar to eddy discharge. In either case, no disturbance amplification would be required. On the straight-tube models there is frequent evidence, in the form of double bow waves, that local flow separation exists at the leading edge. At downstream stations burst formation may be the result of higher frequency disturbances, perhaps introduced at the leading edge, by roughness along the surface, or feeding in from the external flow, which are selectively amplified in the manner confirmed by the experiments of reference 2.

The differences in the location of burst formation and in the extent of the transition region also pose an interesting question: Should not the effects of such parameters as pressure gradient, heat transfer, and surface roughness on the transition from laminar to turbulent flow be expected to vary significantly as the location of burst formation and the extent of the transition region vary? It seems possible that the effects of these parameters on the stability of the laminar boundary layer prior to burst formation can be quite different from their effects on the

remaining portions of laminar boundary layer between bursts within the transition region. The "calming effect" observed in reference 5 indicates that this is certainly true within very limited regions upstream of each burst. Concurrently, the effects on burst growth and velocity could significantly alter the extent of the transition region. Such a question, therefore, seems worthy of further consideration. Transition due to burst formation at the leading edges and tips of models of diverse sizes and shapes, at least within the range of scale tested in the Ames supersonic free-flight wind tunnel, has proven difficult to eliminate, and in that sense may be considered to be "natural" transition.

### SUMMARY OF RESULTS

Shadowgraphs showing turbulent bursts on the surfaces of bodies in supersonic free flight were analyzed. The plan forms and thickness profiles of bursts in supersonic flow generally resemble those measured in low subsonic flow by other investigators. It was found possible to define the three-dimensional geometry of a burst from shadowgraphs. The geometries of two discrete bursts were so determined.

The velocity at which a burst moves downstream over the surface was found to increase with increasing Mach number and decrease with increasing surface roughness. The effect of Mach number on burst velocity appears to be strongly dependent on the degree of surface roughness present. In terms of distance traveled, the longitudinal growth rate of a burst was found to decrease with increasing Mach number but increase with increasing surface roughness.

For a given configuration under the flow conditions encountered in the present analysis (viz., body-fixed disturbance source at the leading edge) the greatest number of bursts tended to form at some preferred frequency, while lesser numbers formed at harmonics of this frequency. This fundamental preferred frequency was found to vary with unit Reynolds number and increased as unit Reynolds number increased. However, local geometry of the leading edge appeared to have the strongest influence on the preferred formation frequency.

Ames Aeronautical Laboratory  
National Advisory Committee for Aeronautics  
Moffett Field, Calif., Jan. 24, 1958



## REFERENCES

1. Dryden, Hugh L.: Recent Investigations of the Problem of Transition. Zeitschrift für Flugwissenschaften, 4 Jahrgang, Heft 3/4, März/April 1956, pp. 89-95.
2. Schubauer, G. B., and Skramstad, H. K.: Laminar-Boundary-Layer Oscillations and Transition on a Flat Plate. NACA Rep. 909, 1948. (Supersedes NACA WR W-8)
3. Dryden, Hugh L.: Air Flow in the Boundary Layer Near a Plate. NACA Rep. 562, 1936.
4. Emmons, Howard W., and Bryson, A. E.: Transition in a Boundary Layer. Res. and Dev. Labs. Tech. Memo. 245, Hughes Aircraft Co., Sept. 1950.
5. Schubauer, G. B., and Klebanoff, P. S.: Contributions on the Mechanics of Boundary-Layer Transition. NACA TN 3489, 1955.
6. Görtler, H.: Über eine dreidimensionale Instabilität laminarer Grenzschichten an Konkaven Wänden. Gesellschaft der Wissenschaften zu Göttingen, Nachrichten, Mathematik, vol. 2, no. 1, 1940. (Also available as NACA TM 1375, 1954)
7. Sommer, Simon C., and Stark, James A.: The Effect of Bluntness on the Drag of Spherical-Tipped Truncated Cones of Fineness Ratio 3 at Mach Numbers 1.2 to 7.4. NACA RM A52B13, 1952.
8. Jedlicka, James R., Wilkins, Max E., and Seiff, Alvin: Experimental Determination of Boundary-Layer Transition on a Body of Revolution at  $M = 3.5$ . NACA TN 3342, 1954. (Supersedes NACA RM A53L18)
9. Seiff, Alvin: A Free-Flight Wind Tunnel for Aerodynamic Testing at Hypersonic Speeds. NACA Rep. 1222, 1955. (Supersedes NACA RM A52A24)
10. Mitchner, Morton: Propagation of Turbulence From an Instantaneous Point Disturbance. Readers' Forum, Jour. Aero. Sci., vol. 21, no. 5, May 1954, pp. 350-351.
11. Van Driest, E. R.: Investigation of Laminar Boundary Layer in Compressible Fluids using the Crocco Method. NACA TN 2597, 1952.
12. Korkegi, Robert H.: Transition Studies and Skin-Friction Measurements on an Insulated Flat Plate at a Mach Number of 5.8. Jour. Aero. Sci., vol. 23, no. 2, Feb. 1956, pp. 97-107.
13. Charters, Alex C., Jr.: Transition Between Laminar and Turbulent Flow by Transverse Contamination. NACA TN 891, 1943.

TABLE I.- PRIMARY DATA

Configuration	$M_e$	$T_w/T_\infty$	$U_e/\nu$ , in. <sup>-1</sup> × 10 <sup>-6</sup>	$M_u/M_e$	$x_{u1}$ , in.	$L/x_{u1}$	$H$ , in. × 10 <sup>-6</sup>	$R_H/c$
Straight tube	2.72	1.0	2.45	0.58	2.32	0.93	---	~3
Straight tube	2.72		2.45	.58	2.16	.73	---	~3
Contoured tube	3.10		1.78	.74	---	---	600	171
	3.67		2.19	---	2.07	.58	440	144
				.58	3.49	.80		
				.60	---	---		
				.62	2.32	1.12		
				---	1.49	.62		
				.62	2.36	1.01		
				.60	---	---		
	3.72		2.07	---	1.39	.53	100	30.7
	3.72		2.07	.51	2.19	.74	100	30.7
	3.72		2.07	---	3.15	.70	100	30.7
	3.78		2.19	.74	---	---	600	193
Straight tube	3.80		2.24	.54	---	---	50	16.5
	3.80		2.24	.54	---	---	50	16.5
	3.80		2.24	.56	---	---	50	16.5
	3.80		2.84	---	3.05	.89	300	99.6
	3.89		2.29	.46	3.52	.60	50	16.6
	3.89		2.29	.50	---	---		16.6
	3.91		2.30	.55	2.01	.60		16.7
	3.91		2.30	.56	2.80	.87		16.7
	3.91		2.30	.63	2.83	.51		16.7
	3.94		2.32	.44	---	---		16.7
Contoured tube	4.06		3.11	.56	1.80	1.05	300	133
Straight tube	4.44	1.8	2.84	.37	---	---	300	100.5
Straight tube	4.44		2.84	.53	---	---	300	100.5
Straight tube	4.44		2.84	.47	---	---	300	100.5
Contoured tube	4.78		2.99	.48	---	---	960	326
Straight tube	5.06		3.03	.47	---	---	300	100.5
	5.06		3.03	.44	---	---	300	100.5
	6.48		2.94	---	3.10	.26	500	141
	6.48		2.94	.44	4.50	.36	500	141
	6.71		5.86	.54	---	---	300	165
	6.71		5.86	.48	---	---	300	165
Contoured tube	6.81		3.00	.45	---	---	2100	584
Straight tube	6.81		3.05	.32	---	---	300	84.7
Contoured tube	6.96		3.18	---	2.75	.47	1500	435
Contoured tube	6.96		3.18	.42	4.30	.52	1500	435
Pencil model	2.70	1.0	2.27	.72	---	---	400	151
	2.70		2.27	.72	---	---	400	151
	2.70		2.27	.72	---	---	400	151
	3.45		4.01	.47	---	---	10	6.2
	3.46		2.00	---	2.55	.24	130	39.9
	3.46		2.00	---	3.20	.39	130	39.9
	3.46		2.00	.47	3.15	.36	130	39.9
	3.49		2.05	.46	2.02	.26	150	46.9
				---	2.31	.33		
				---	3.06	.27		
				---	3.79	.30		
				---	2.55	.44		
				---	2.97	.46		
				.47	2.48	.29		

<sup>a</sup>Ratio of wall temperature to free-stream temperature.

TABLE I.- PRIMARY DATA - Concluded

Configuration	$M_e$	$T_w/T_\infty$	$U_e/\nu$ , in. <sup>-1</sup> × 10 <sup>-6</sup>	$M_u/M_e$	$x_u$ , in.	$L/x_u$	$H$ , in. × 10 <sup>-6</sup>	$R_H/c$
Pencil model	3.50	1.0	2.11	0.45	---	---	10	3.2
	3.50		2.11	---	1.40	0.63		3.2
	3.50		2.11	---	1.32	.45		3.2
	3.54		2.04	.39	3.60	.35		3.6
	3.54			---	2.18	.29		3.6
	3.54			.40	2.21	.56		3.6
	3.54			---	2.17	.59		3.6
	3.57			---	2.54	.18		3.1
				---	3.18	.17		
				---	3.64	.21		
				---	4.28	.23		
				---	2.19	.29		
				---	2.74	.27		
				---	1.90	.32		
				---	2.75	.47		
				---	2.62	.55		
	3.58		2.05	---	2.18	.50		
	3.59		3.62	---	1.95	.46	5	2.7
				.40	3.14	.47		
				---	1.78	.37		
				.42	2.34	.46		
				---	1.74	.37		
				---	2.28	.52		
				---	2.84	.50		
				.43	2.00	.37		
				.43	---	---		
				.46	---	---		
	3.60		3.71	---	2.05	.54	10	5.6
	3.61		2.11	.42	---	---	150	47.5
	3.92		2.24	---	1.10	.78	700	227
				.58	2.82	.79		
				.53	1.87	.75		
				.53	1.63	.64		
				.58	---	---		
				.58	2.14	1.02		
	3.95		2.28	.62	---	---		230
	3.95		2.28	.60	2.14	1.02		230
	4.05		2.34	.58	---	---	600	201
	4.05		2.34	.51	---	---	600	201
	4.36		2.55	.59	---	---	700	244
	4.36		2.55	.61	---	---	700	244
	4.56		2.69	.50	---	---	700	251
	4.56		2.69	.54	---	---	700	251
	5.03	1.8	2.53	.31	---	---	130	36.7
	5.03		2.53	.34	---	---	130	36.7
	5.79		4.48	.29	---	---	130	59.6
	6.79		2.20	.25	---	---	700	143
A-4	2.9	1.0	1.73	.36	---	---	---	<30, estimated
	3.2		1.97	.30	---	---	---	
	3.2		1.97	.33	---	---	---	
	6.0	1.8	4.46	.27	---	---	---	
	6.0		4.46	.30	---	---	---	
	8.7		6.34	.21	---	---	---	
10° included-angle cone	7.7		3.9	.30	1.90	.17	---	---
RM-10	3.0	1.0	1.82	.37	---	---	---	---
RM-10	3.0	1.0	1.82	.38	---	---	---	---

<sup>a</sup>Ratio of wall temperature to free-stream temperature.

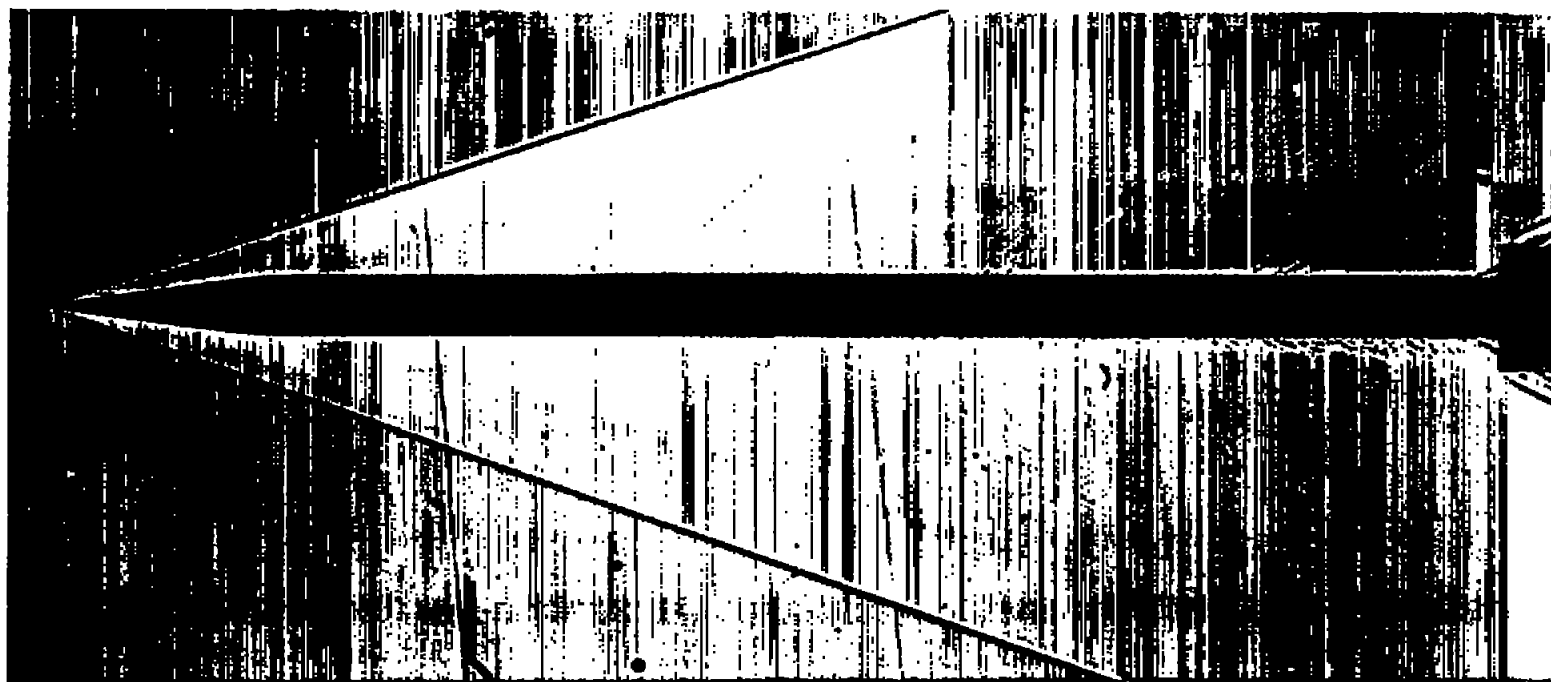
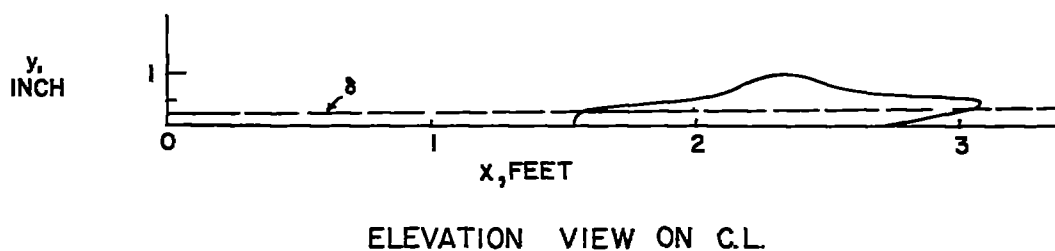
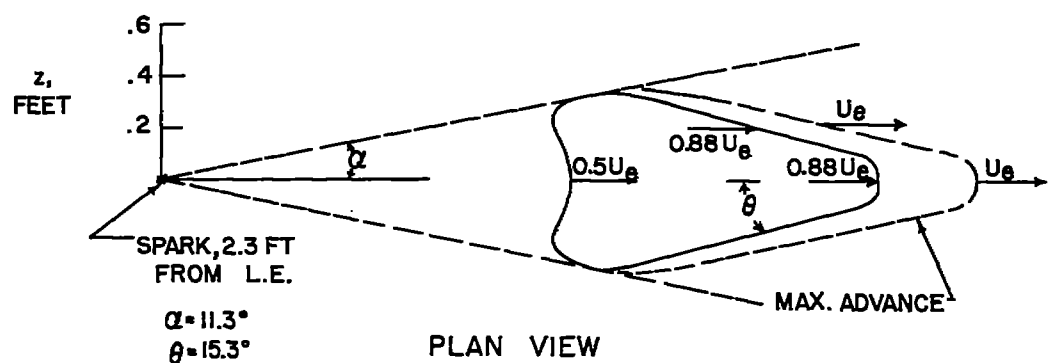
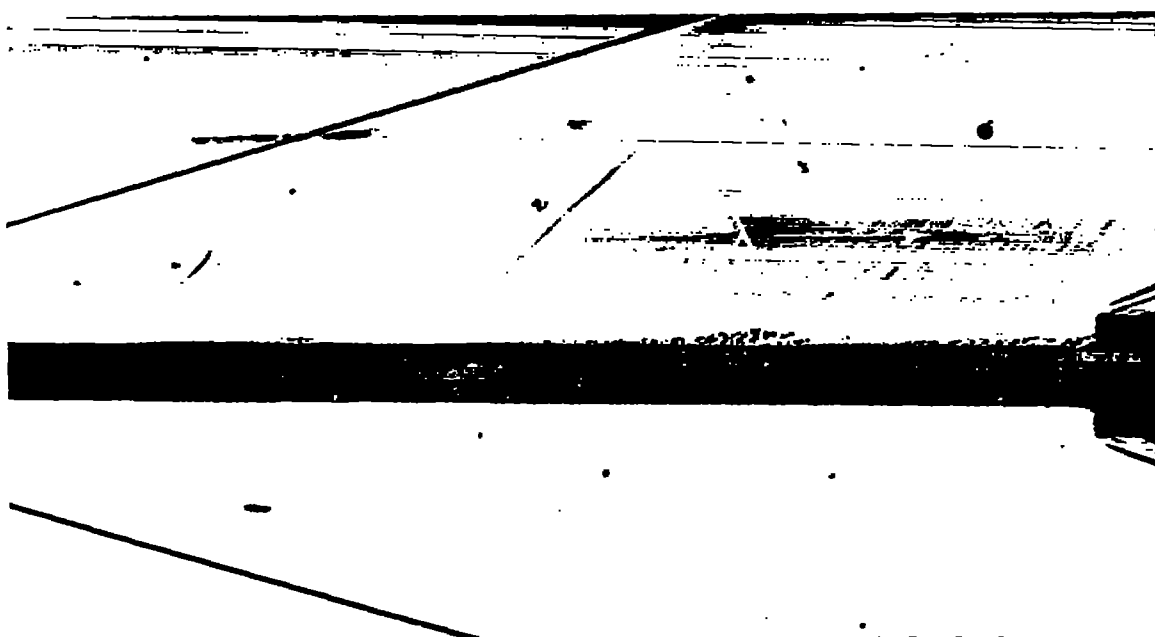


Figure 1.- Shadowgraph of conical-nosed cylinder model in free flight;  $M_\infty = 3.5$ ;  $U_e/\nu = 2.1 \times 10^6$  per inch;  $H = 150 \mu\text{in.}$ ; wind tunnel "air-off"; conical light field.

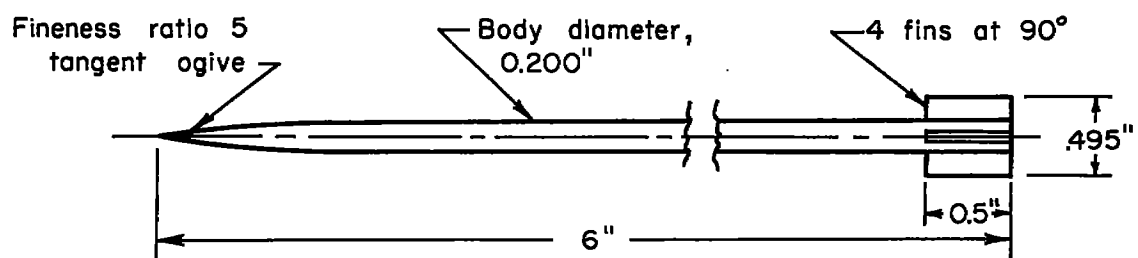


(a) Burst geometry and growth deduced from hot-wire measurements by Schubauer and Klebanoff (portion of fig. 6, ref. 5);  $M_\infty \approx 0.03$ ;  $U_e/\nu \approx 1.5 \times 10^4/\text{in.}$

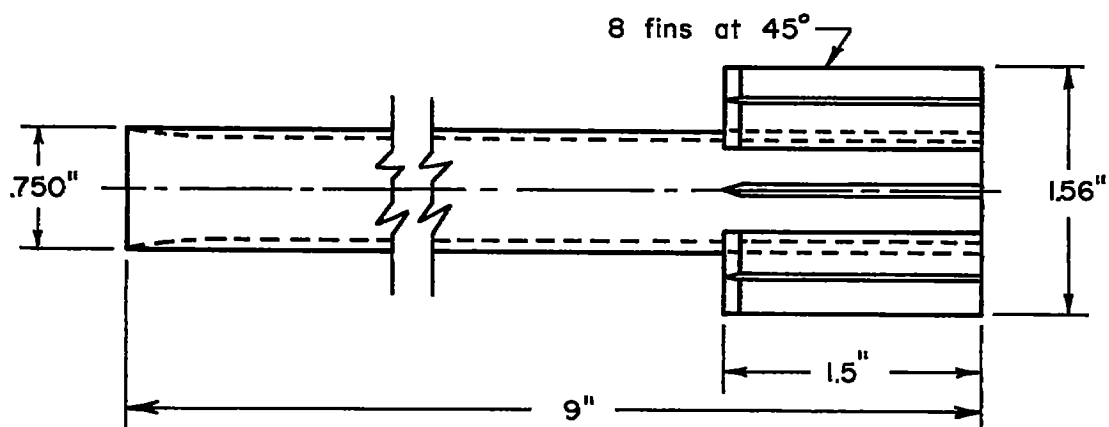


(b) Bursts on a slender ogive-cylinder (pencil model) in free flight;  $M_\infty = 3.6$ ;  $U_e/\nu = 3.6 \times 10^8/\text{in.}$ ; wind tunnel air-off; conical light field.

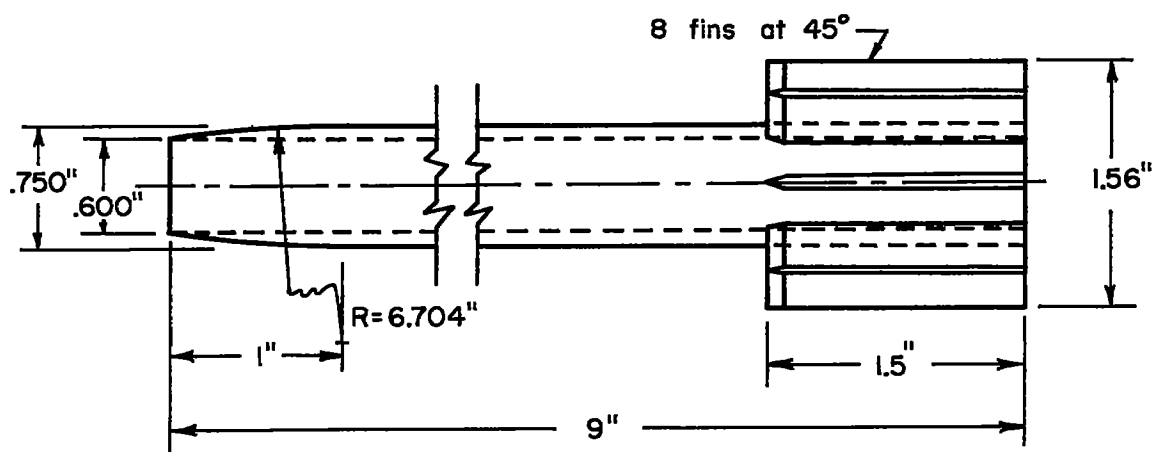
Figure 2.- Comparison of geometric characteristics of bursts observed under widely different flow conditions.



(a) Pencil model

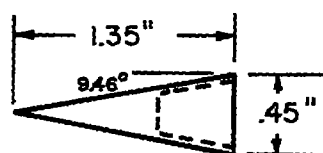


(b) Straight tube

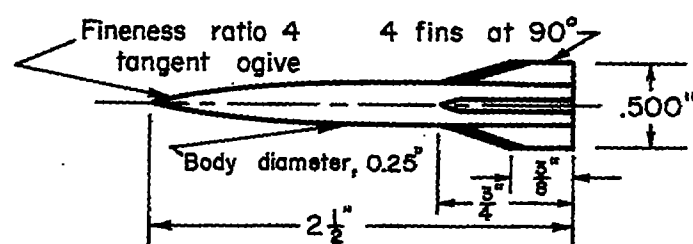


(c) Contoured tube

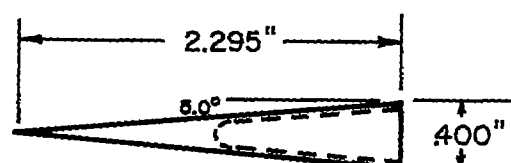
Figure 3.- Model geometries.



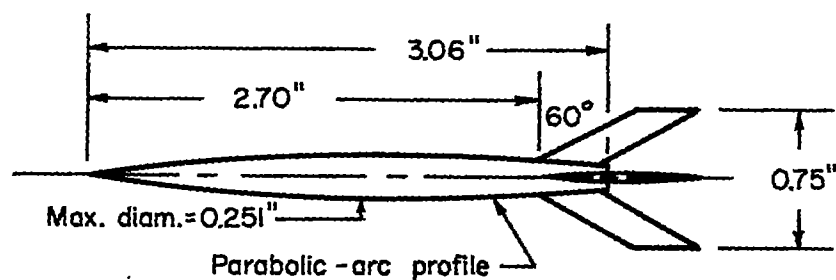
(d) 19° included-angle cone



(e) A-4

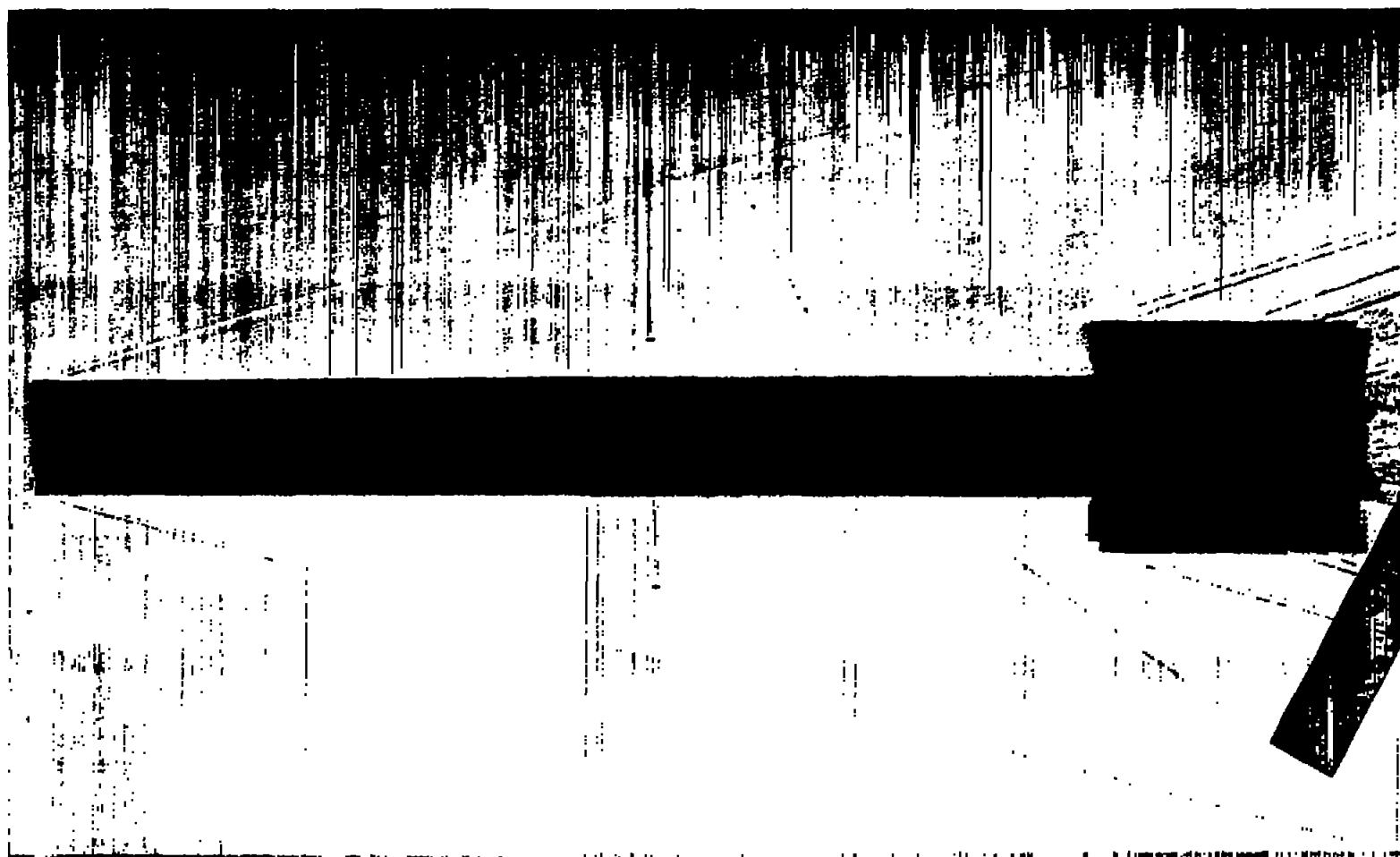


(f) 10° included-angle cone



(g) NACA RM-10

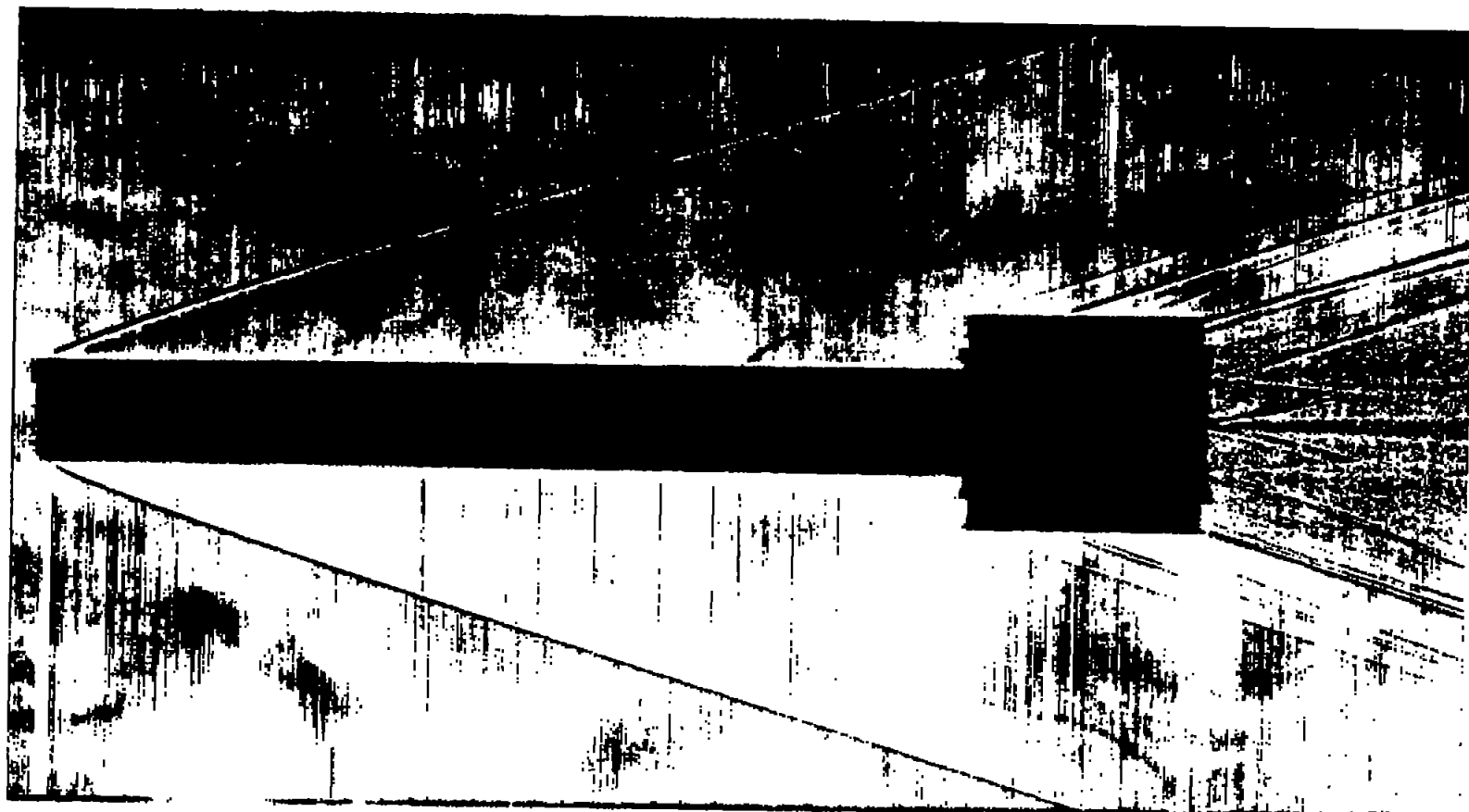
Figure 3.- Concluded.



(a) Straight tube;  $M_\infty = 3.9$ ;  $U_\infty/\nu = 2.3 \times 10^6/\text{in.}$ ;  $H = 50 \mu\text{in.}$ ; aeroballistic range; conical light field.

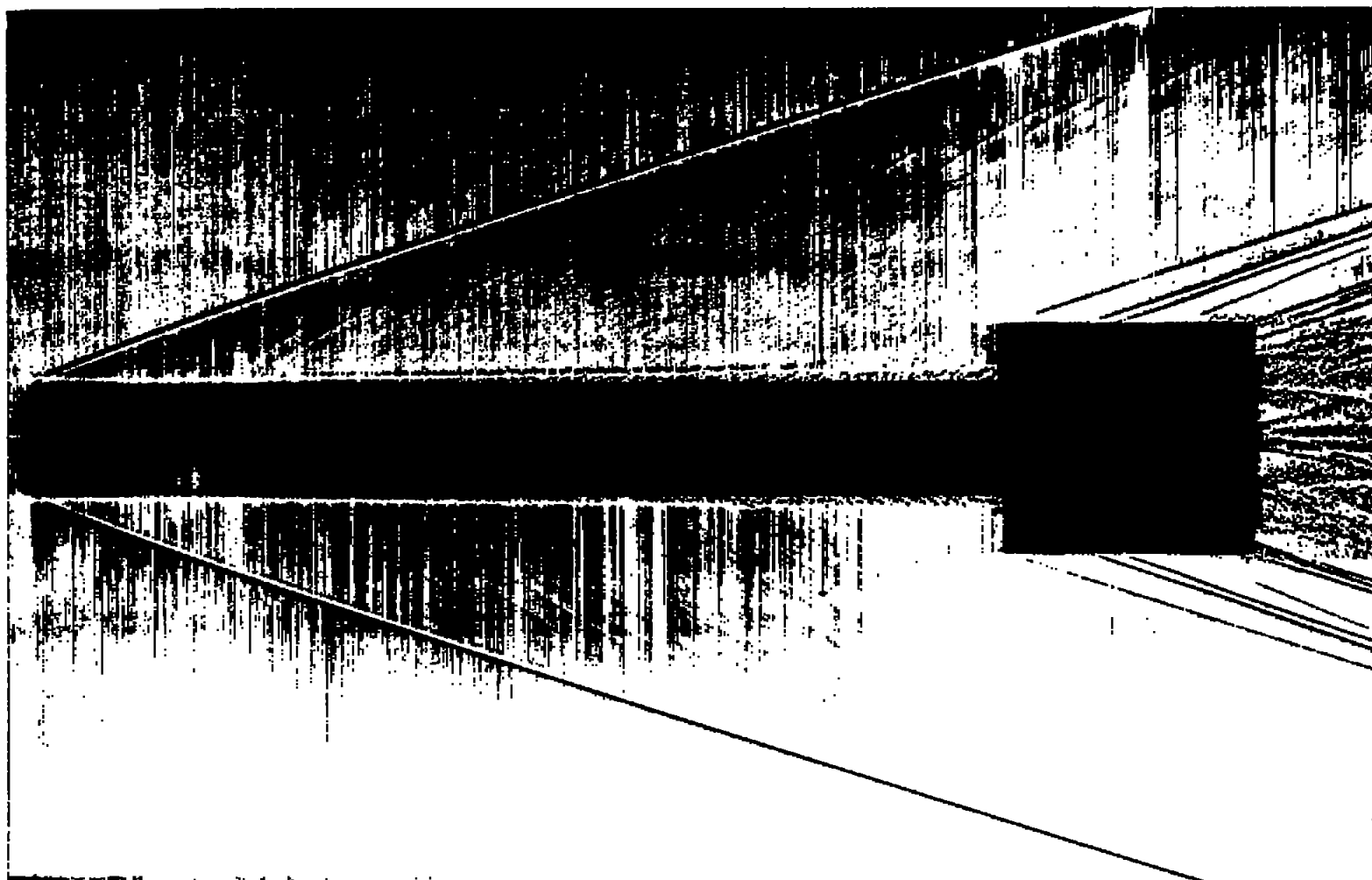
Figure 4.- Shadowgraphs of model in free flight.





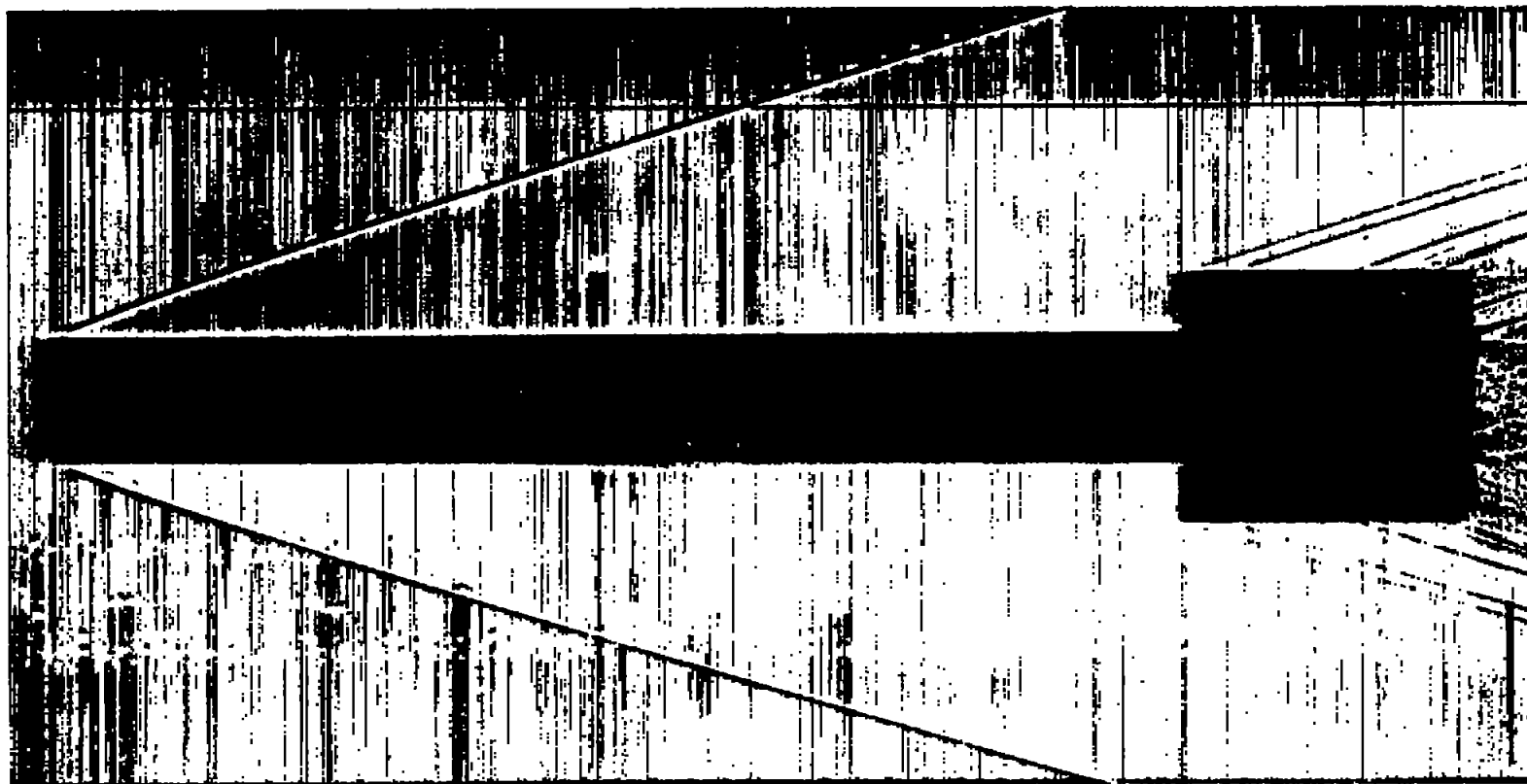
(b) Straight tube;  $M_{\infty} = 3.9$ ;  $U_e/v = 2.3 \times 10^6/\text{in.}$ ;  $H = 50 \mu\text{in.}$ ; aeroballistic range; conical light field.

Figure 4.- Continued.



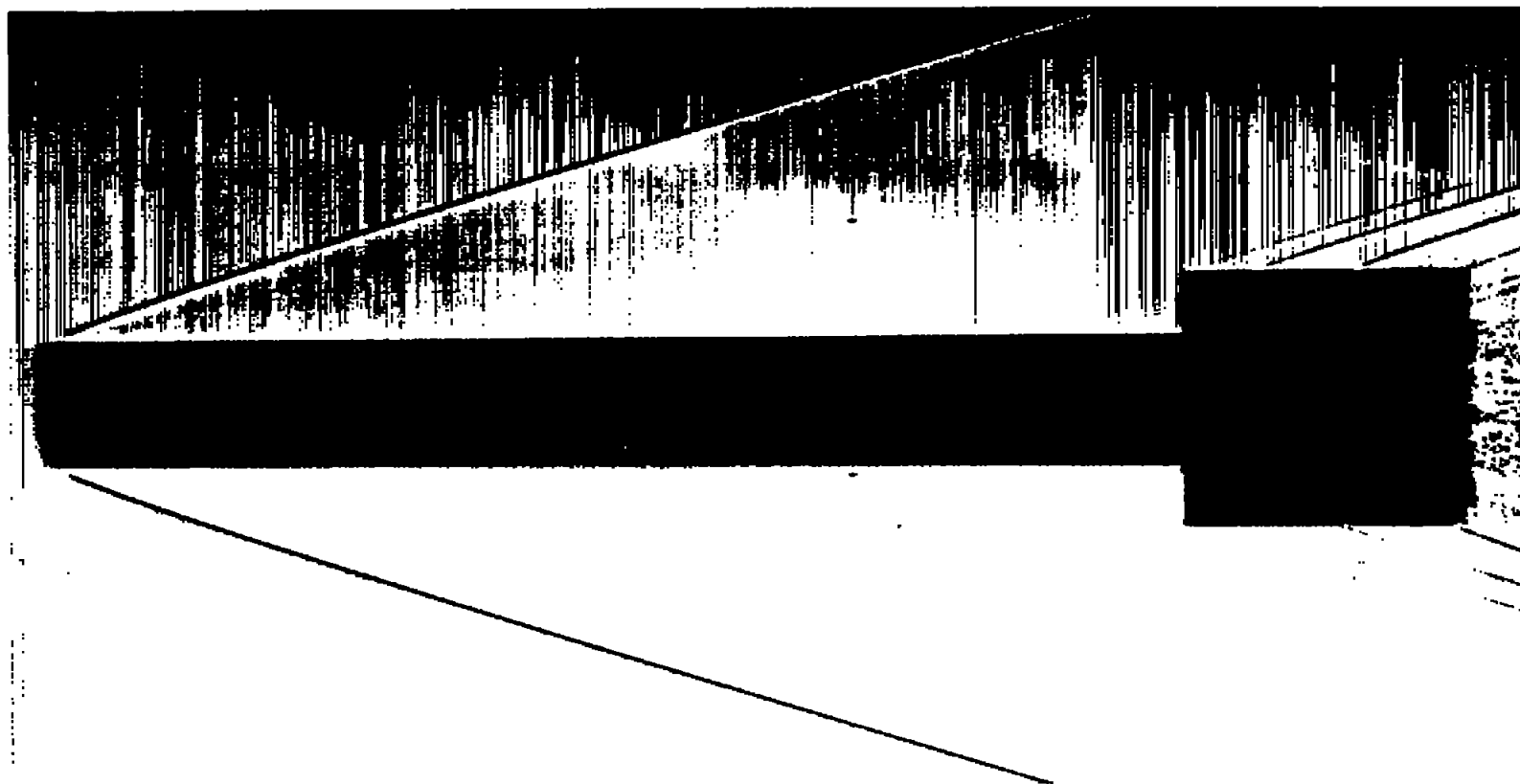
(c) Straight tube;  $M_{\infty} = 3.8$ ;  $U_e/v = 2.2 \times 10^8/\text{in.}$ ;  $H = 50 \mu\text{in.}$ ; aeroballistic range; conical light field.

Figure 4.- Continued.



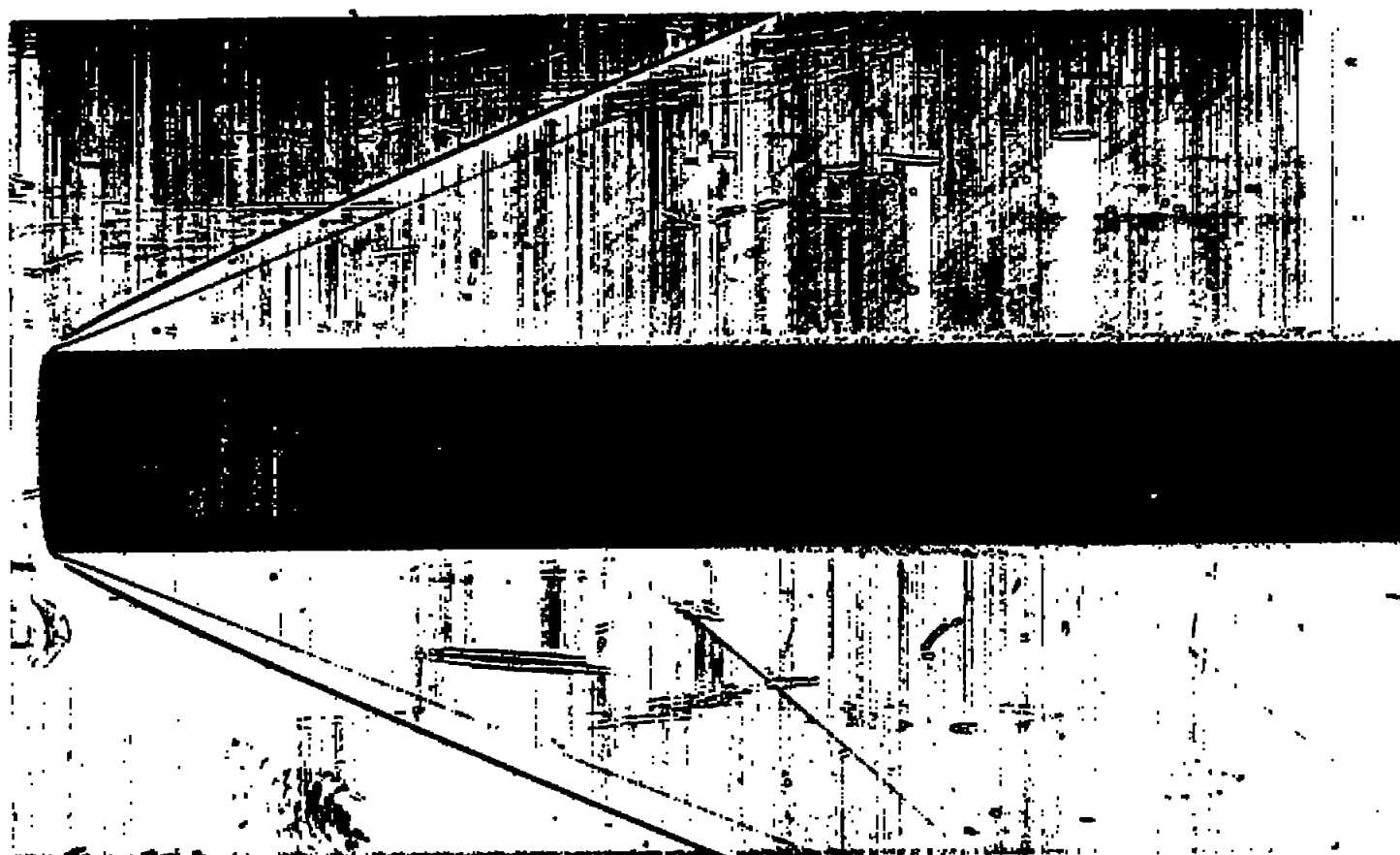
(d) Straight tube;  $M_\infty = 3.9$ ;  $U_e/v = 2.3 \times 10^6/\text{in.}$ ;  $H = 50 \mu\text{in.}$ ; aeroballistic range; conical light field. Orthogonal view of same model as fig. 4(e) at same instant.

Figure 4.- Continued.



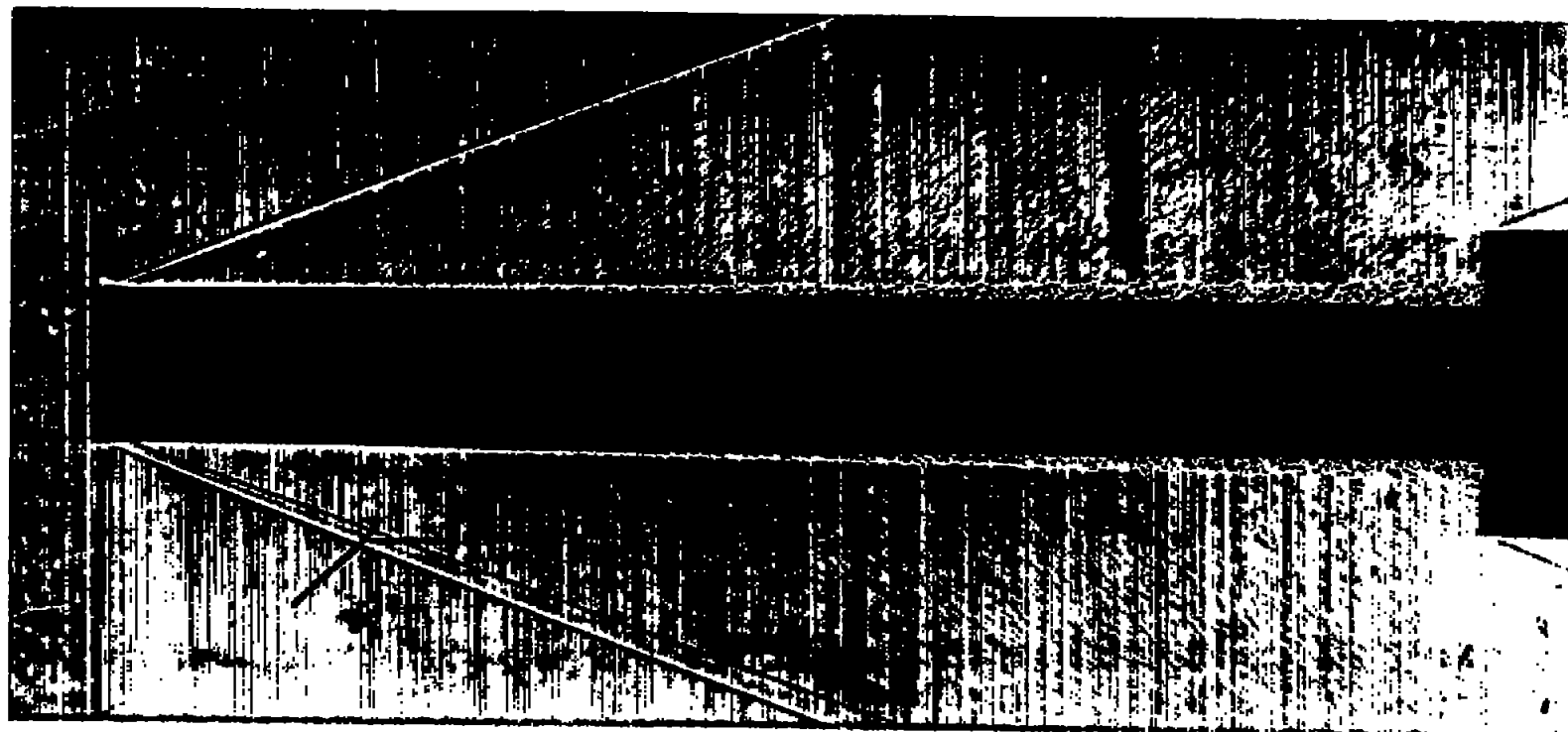
(e) Straight tube;  $M_\infty = 3.9$ ;  $U_e/v = 2.3 \times 10^6/\text{in.}$ ;  $H = 50 \text{ } \mu\text{in.}$ ; aeroballistic range; conical light field. Orthogonal view of same model as fig. 4(d) at same instant.

Figure 4.- Continued.



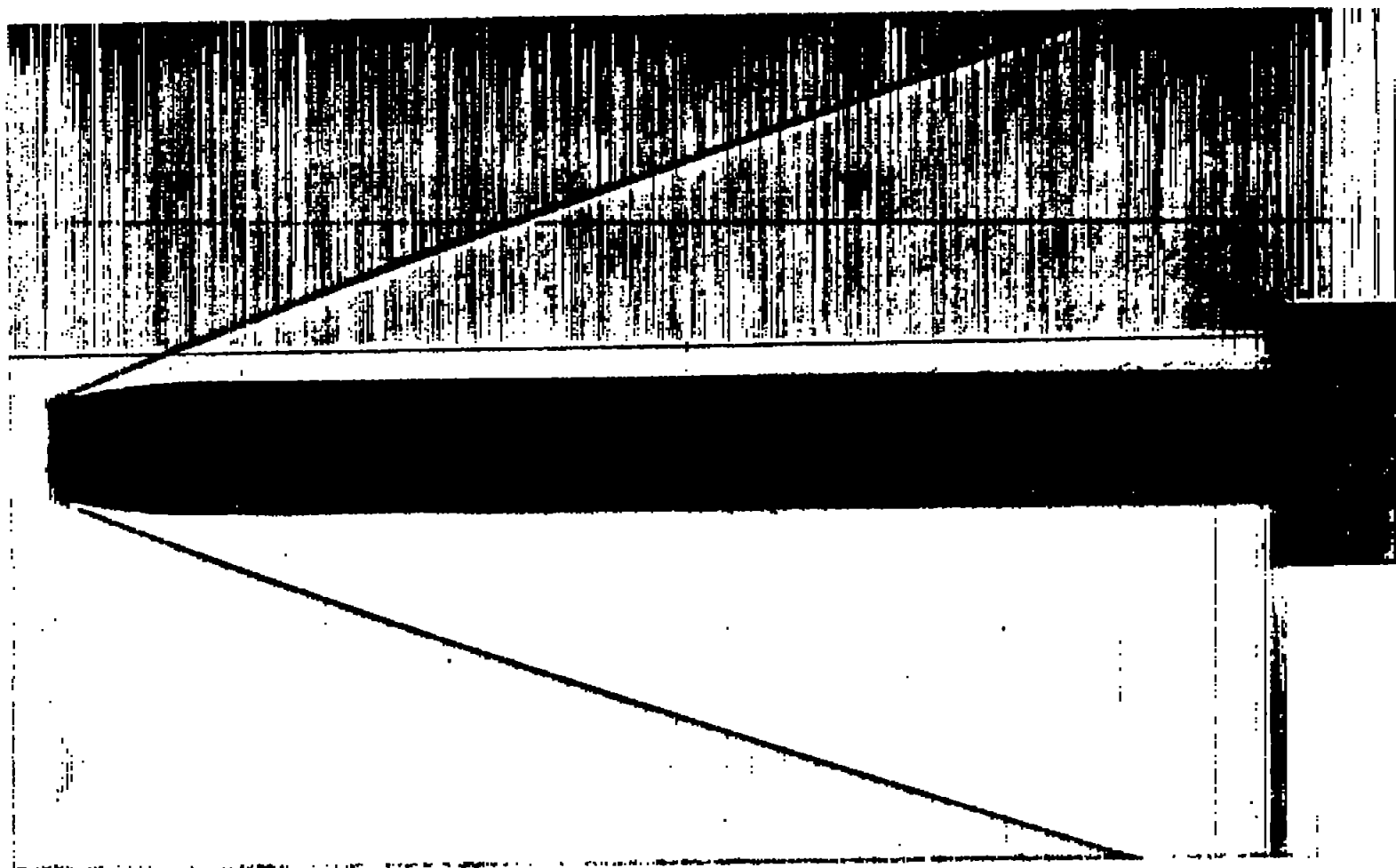
(f) Straight tube;  $M_\infty = 2.7$ ;  $U_e/\nu = 2.4 \times 10^6/\text{in.}$ ;  $H = 10 \mu\text{in.}$ ; wind tunnel air-off; conical light field; choked internal flow.

Figure 4.- Continued.



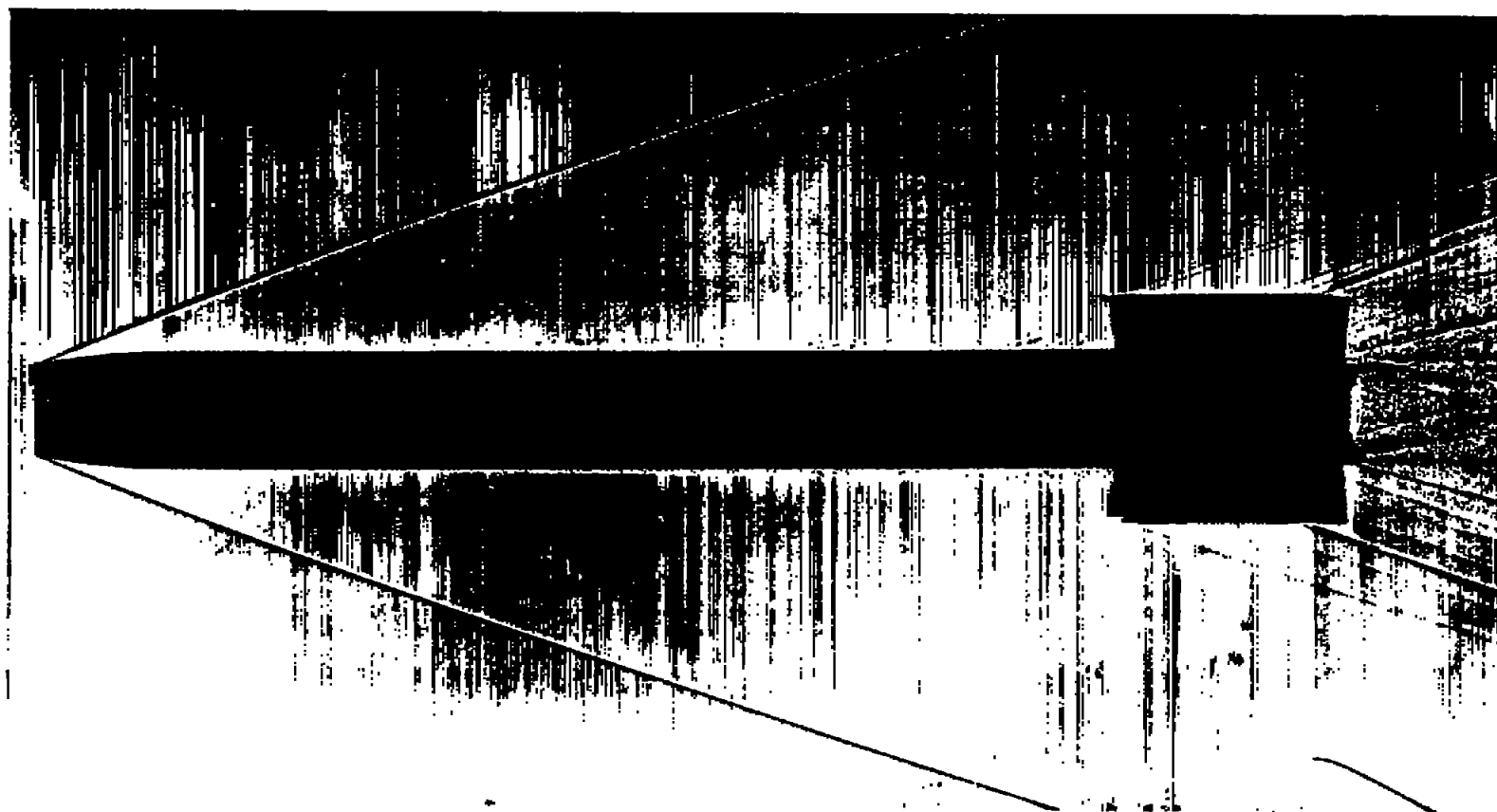
(g) Straight tube;  $M_\infty = 3.1$ ;  $U_e/\nu = 3.1 \times 10^6/\text{in.}$ ;  $H = 500 \mu\text{in.}$ ; wind tunnel air-off; parallel light field.

Figure 4.- Continued.



(h) Contoured tube;  $M_\infty = 3.7$ ;  $U_e/v = 2.2 \times 10^6/\text{in.}$ ;  $H = 440 \text{ } \mu\text{in.}$ ; aeroballistic range; conical light field. Same view of same model as fig. 4(i), but 0.0048 second earlier.

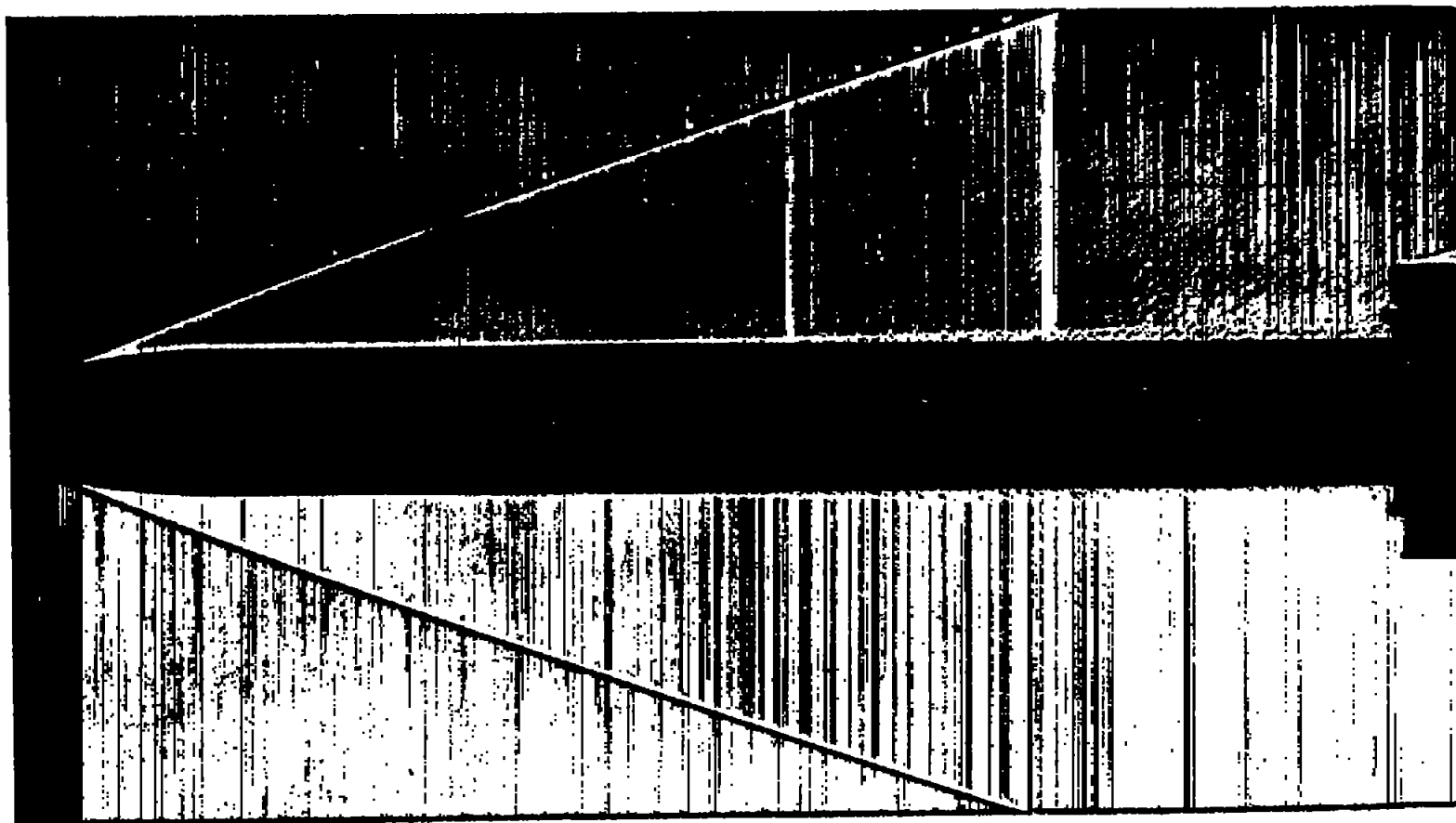
Figure 4.- Continued.



(1) Contoured tube;  $M_\infty = 3.7$ ;  $U_e/v = 2.2 \times 10^6/\text{in.}$ ;  $H = 440 \mu\text{in.}$ ; aeroballistic range; conical light field. Same view of same model as fig. 4(h), but 0.0048 second later.

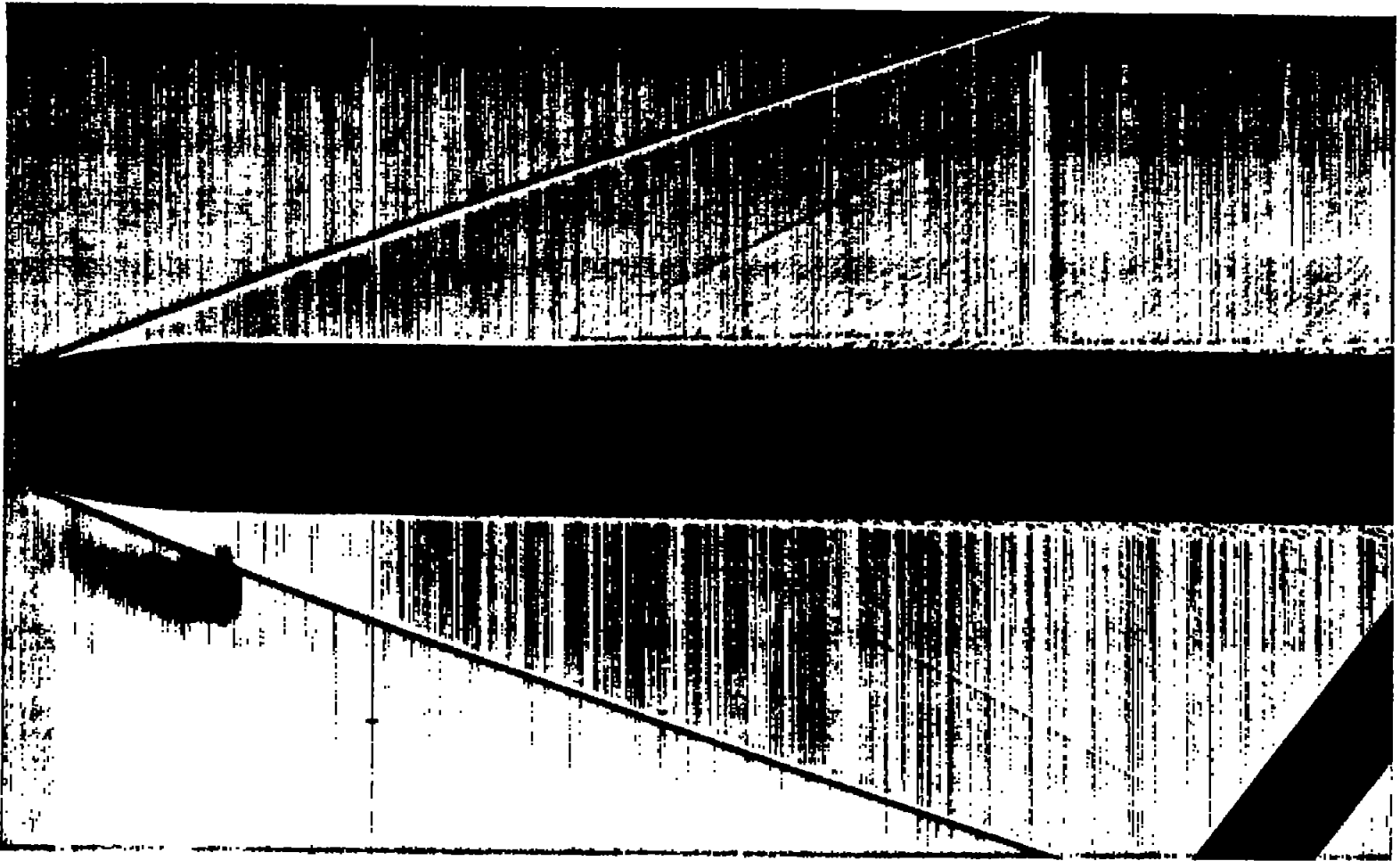
Figure 4.- Continued.





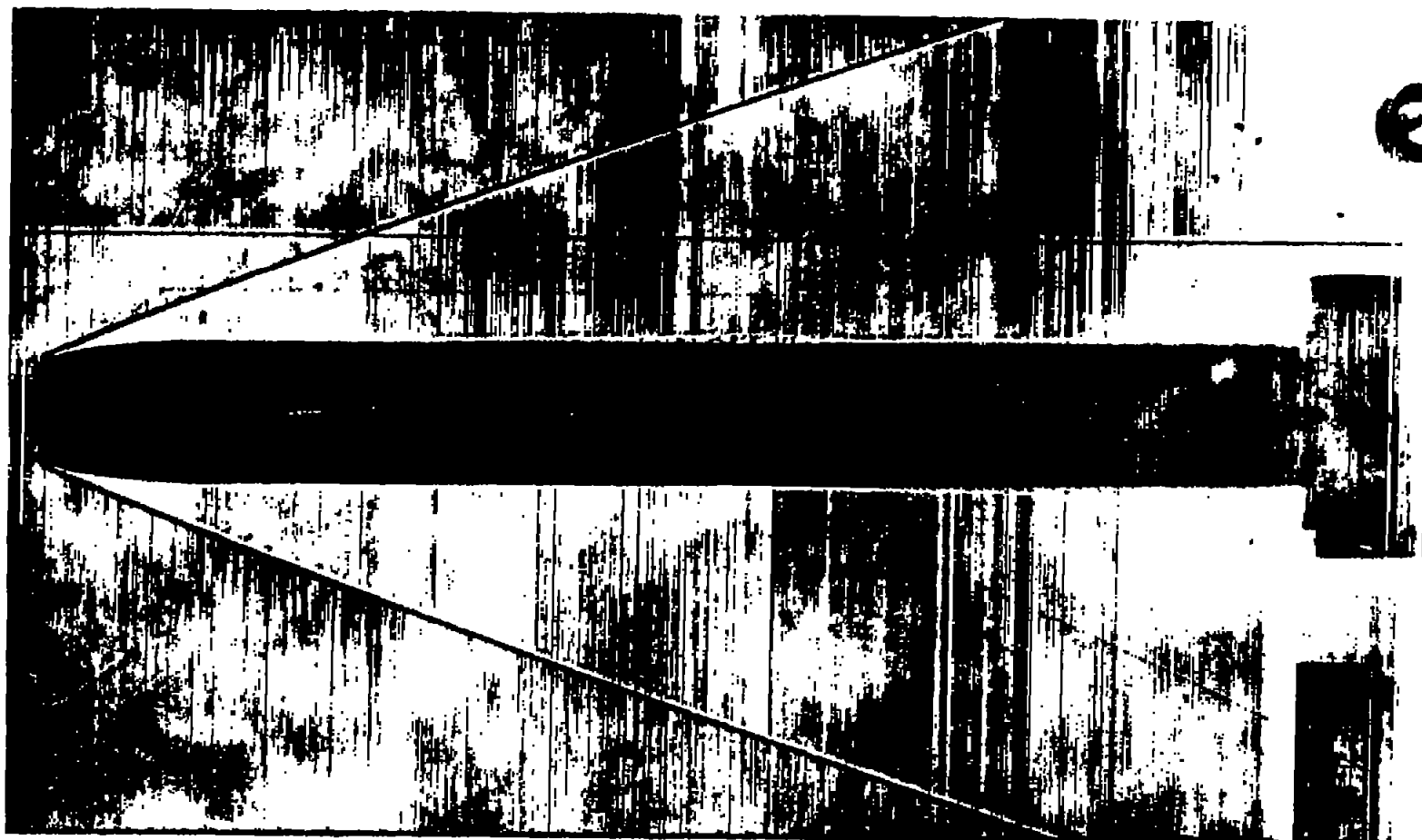
(j) Contoured tube;  $M_\infty = 3.7$ ;  $U_e/v = 2.2 \times 10^8/\text{in.}$ ;  $H = 440 \mu\text{in.}$ ; aeroballistic range; conical light field. Orthogonal view of same model as fig. 4(k) at same instant.

Figure 4.- Continued.



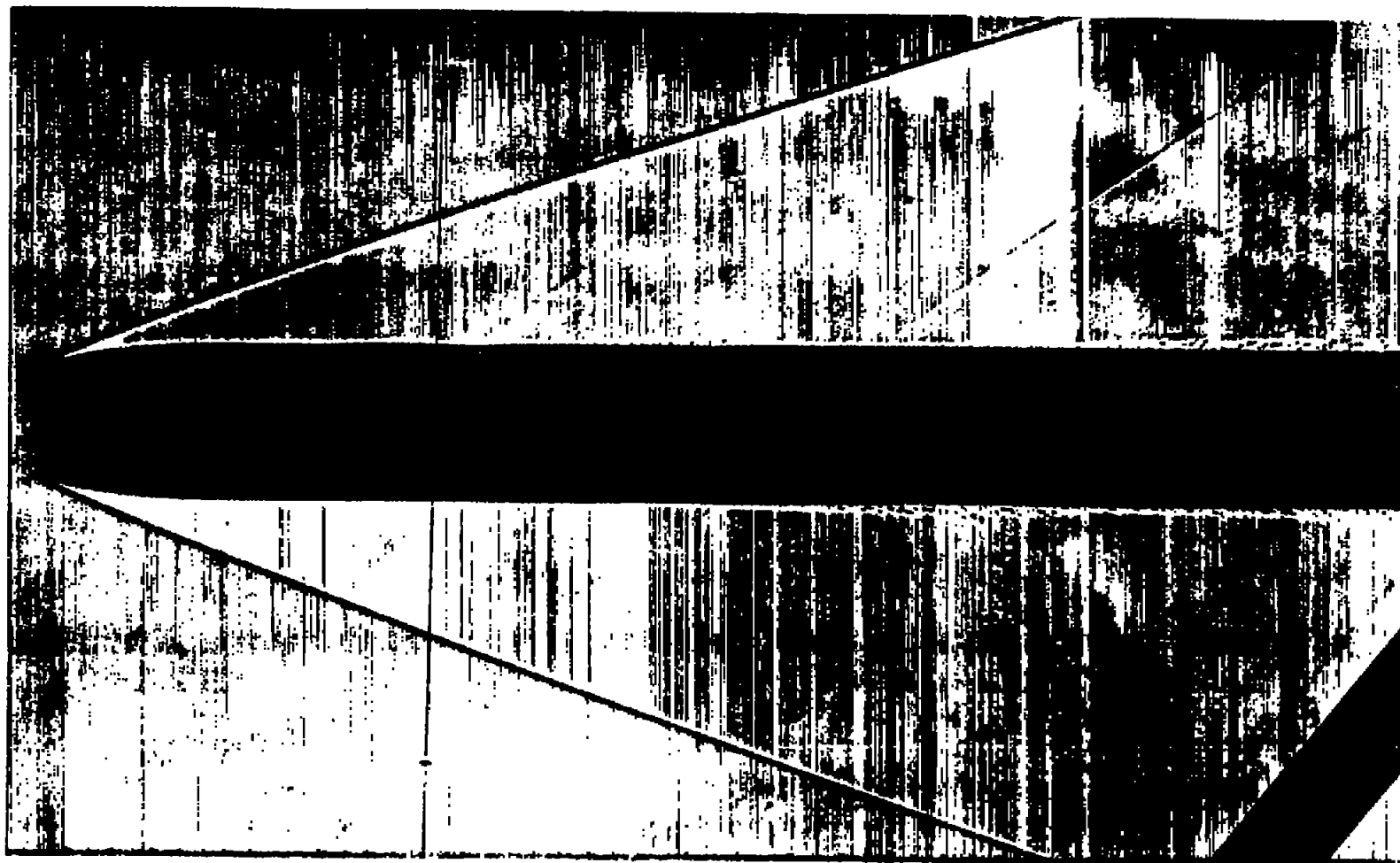
(k) Contoured tube;  $M_\infty = 3.7$ ;  $U_e/v = 2.2 \times 10^6/\text{in.}$ ;  $H = 440 \mu\text{in.}$ ; aeroballistic range; conical light field. Orthogonal view of same model as fig. 4(j) at same instant.

Figure 4.- Continued.



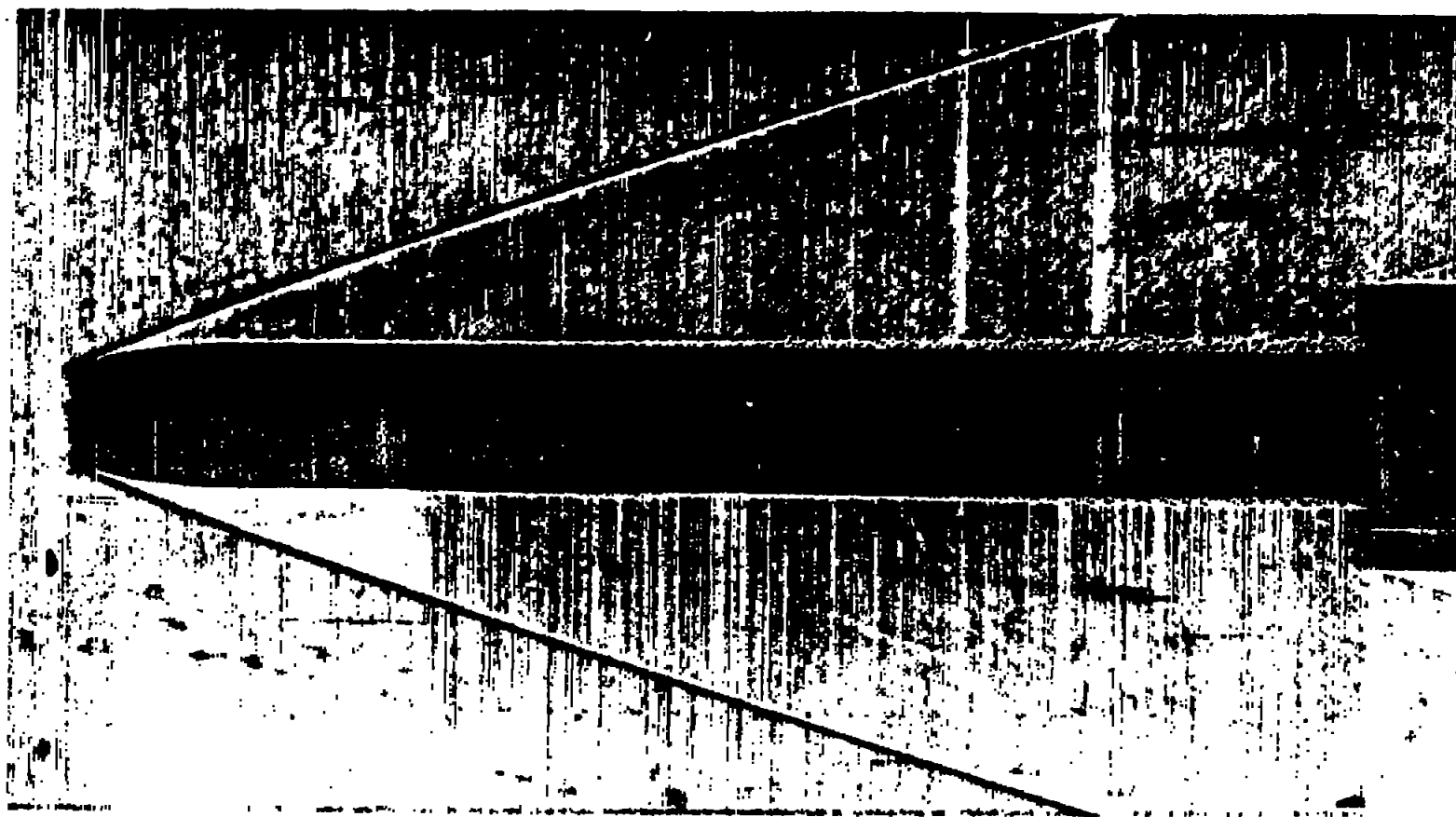
(2) Contoured tube;  $M_{\infty} = 3.7$ ;  $U_e/v = 2.2 \times 10^6/\text{in.}$ ;  $H = 440 \mu\text{in.}$ ; aeroballistic range; conical light field. Same view of same model as fig. 4(j) but 0.0132 second later.

Figure 4.- Continued.



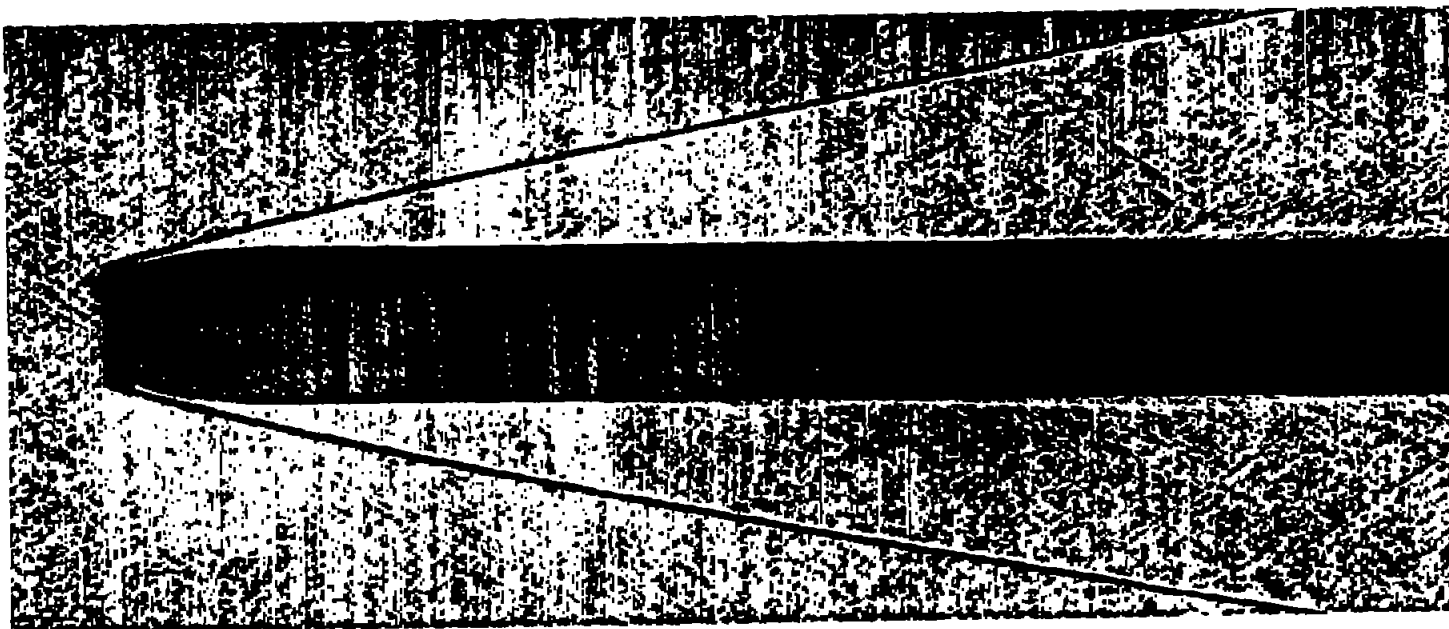
(m) Contoured tube;  $M_{\infty} = 3.7$ ;  $U_e/\nu = 2.1 \times 10^8/\text{in.}$ ;  $H = 100 \mu\text{in.}$ ; aeroballistic range; conical light field.

Figure 4.- Continued.



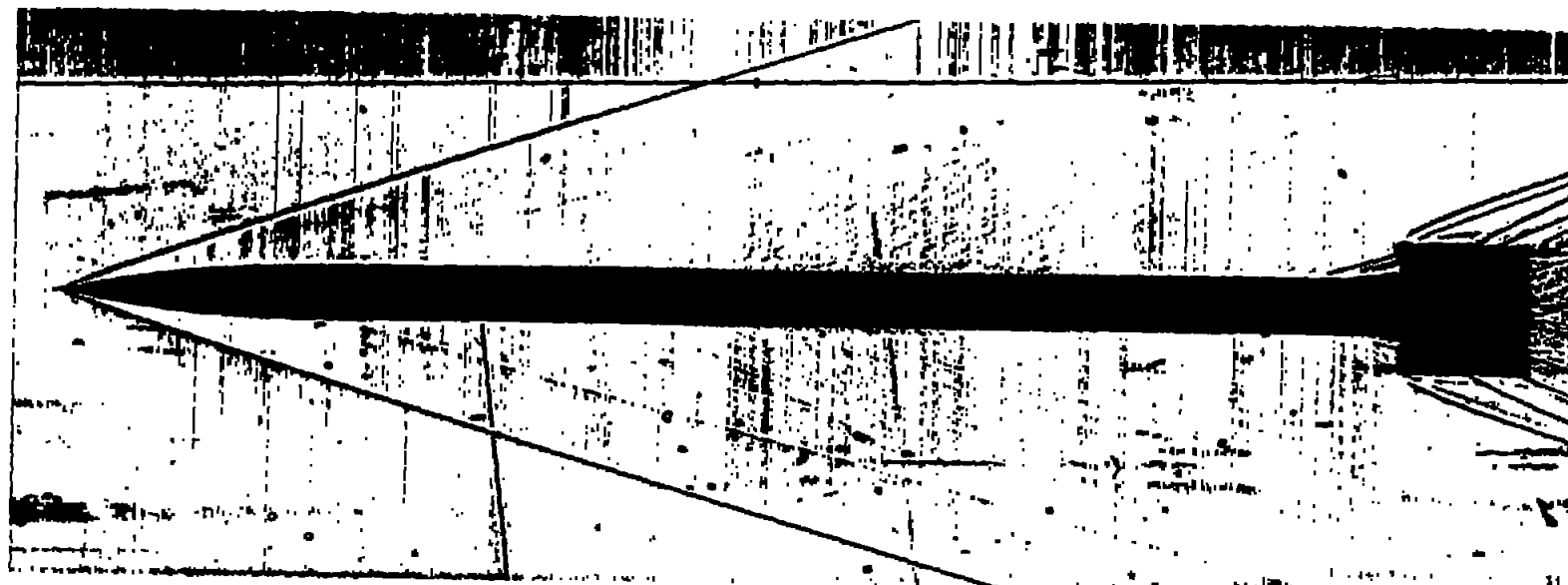
(n) Contoured tube;  $M_{\infty} = 4.1$ ;  $U_e/v = 3.1 \times 10^6/\text{in.}$ ;  $H = 300 \mu\text{in.}$ ; wind tunnel air-off; parallel light field.

Figure 4.- Continued.



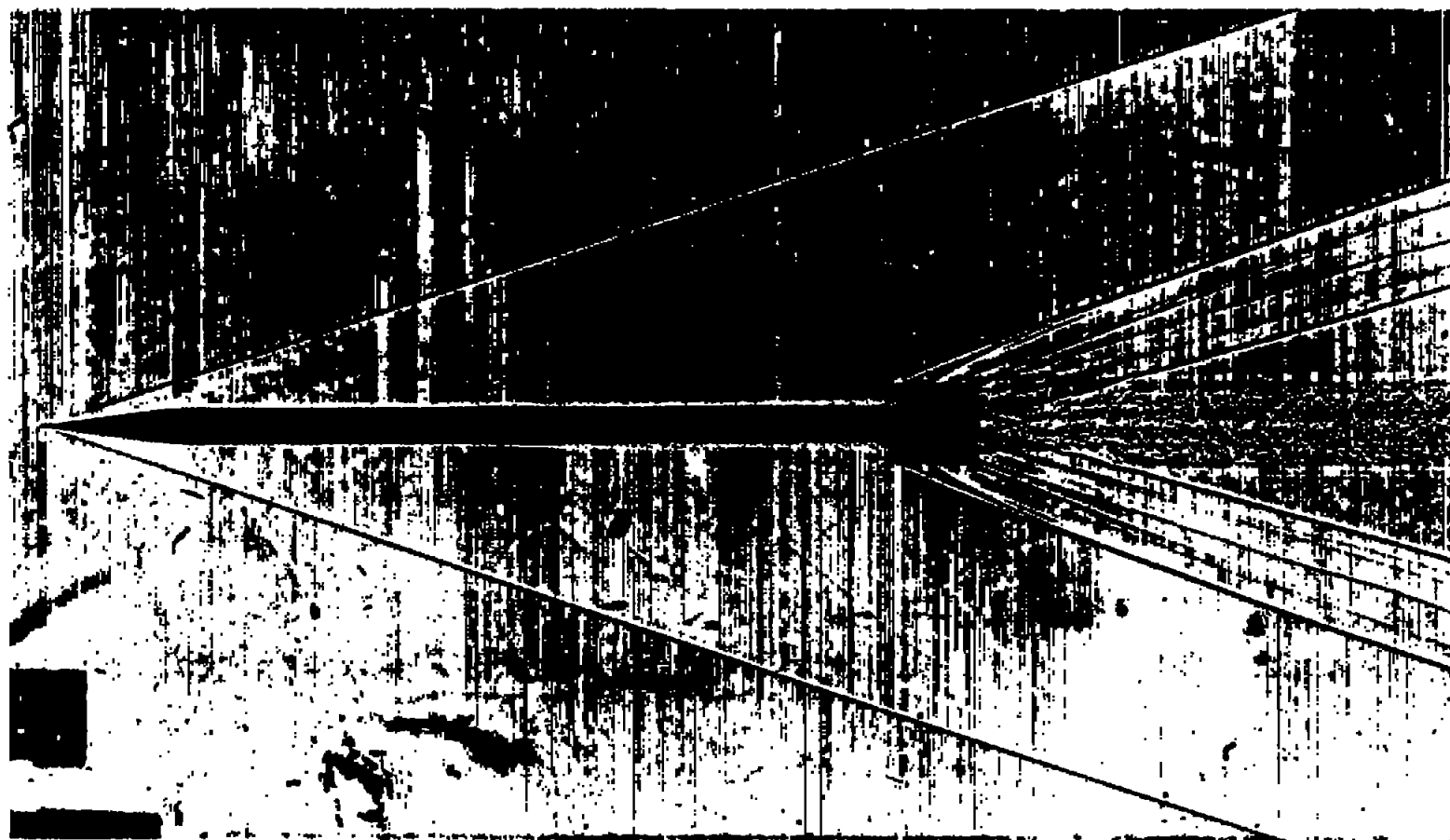
(o) Contoured tube;  $M_\infty = 7.0$ ;  $U_e/\nu = 3.2 \times 10^6/\text{in.}$ ;  $H = 1500 \mu\text{in.}$ ; wind tunnel air-on; parallel light field.

Figure 4.- Continued.



(p) Pencil model;  $M_\infty = 3.9$ ;  $U_e/v = 2.2 \times 10^6/\text{in.}$ ;  $H = 700 \mu\text{in.}$ ; wind tunnel air-off; conical light field.

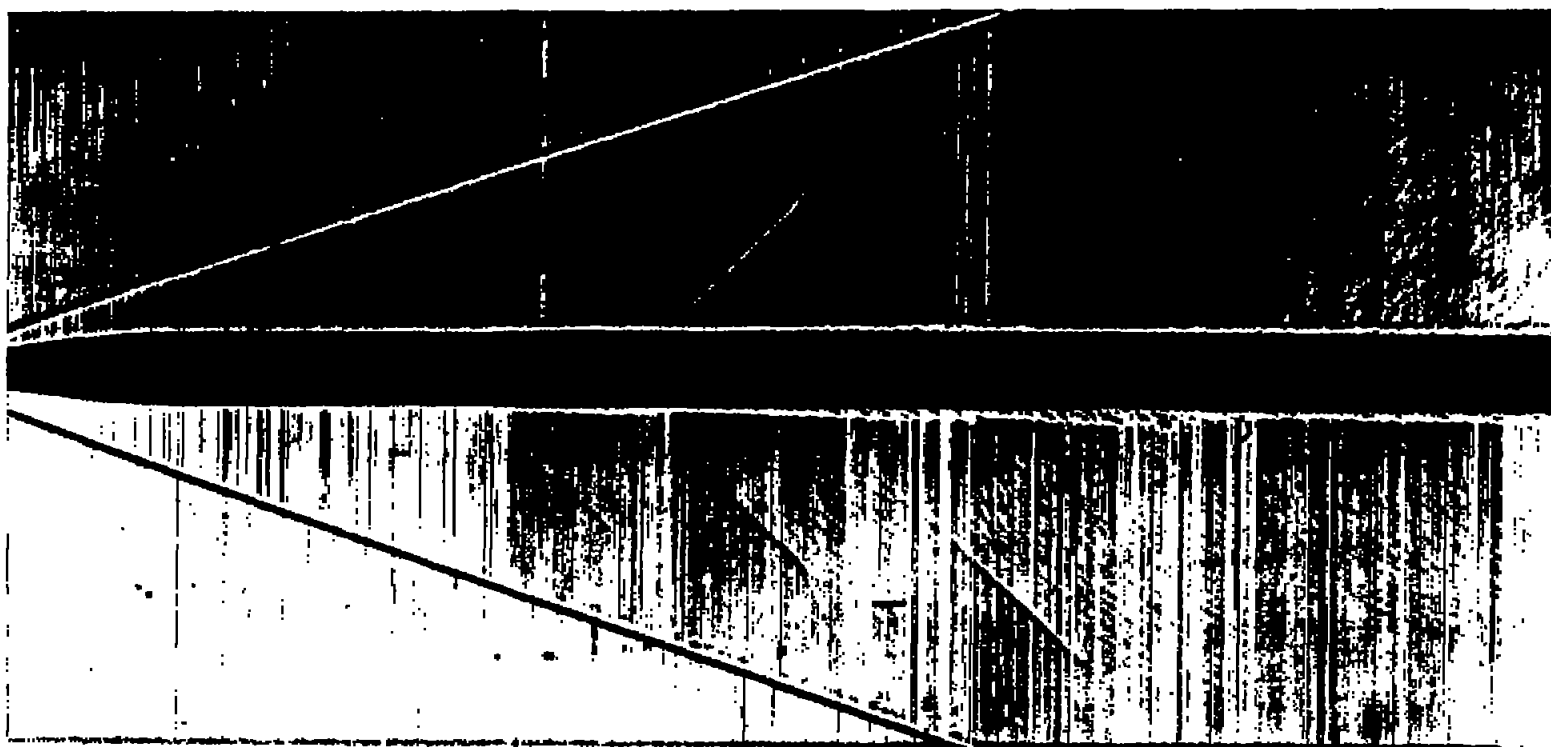
Figure 4.- Continued.



(q) Pencil model (conical nose);  $M_\infty = 3.5$ ;  $U_e/\nu = 2.1 \times 10^6/\text{in.}$ ;  $H = 150 \mu\text{in.}$ ; wind tunnel air-off parallel light field.

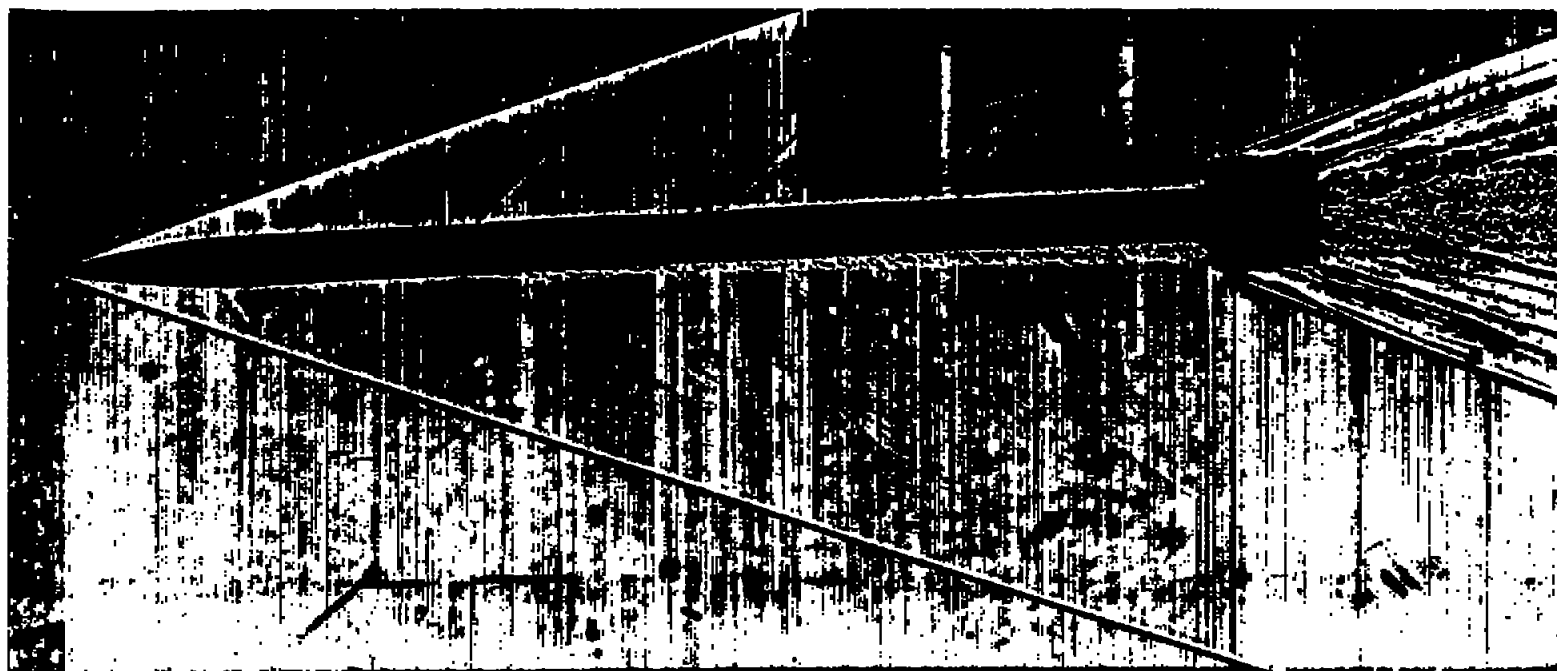
Figure 4.- Continued.





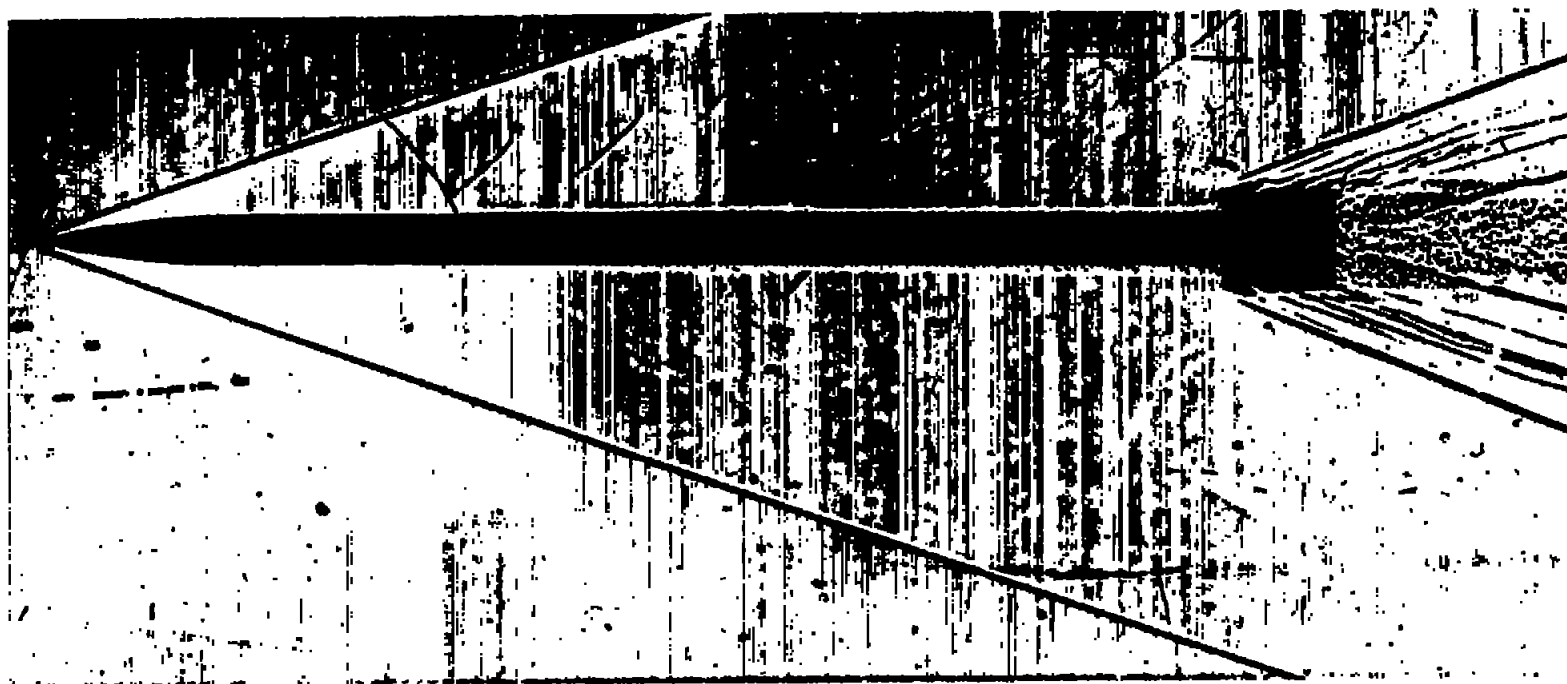
(r) Pencil model;  $M_\infty = 3.6$ ;  $U_e/\nu = 3.6 \times 10^6/\text{in.}$ ;  $H = 5 \mu\text{in.}$ ; wind tunnel air-off; conical light field.

Figure 4.- Continued.



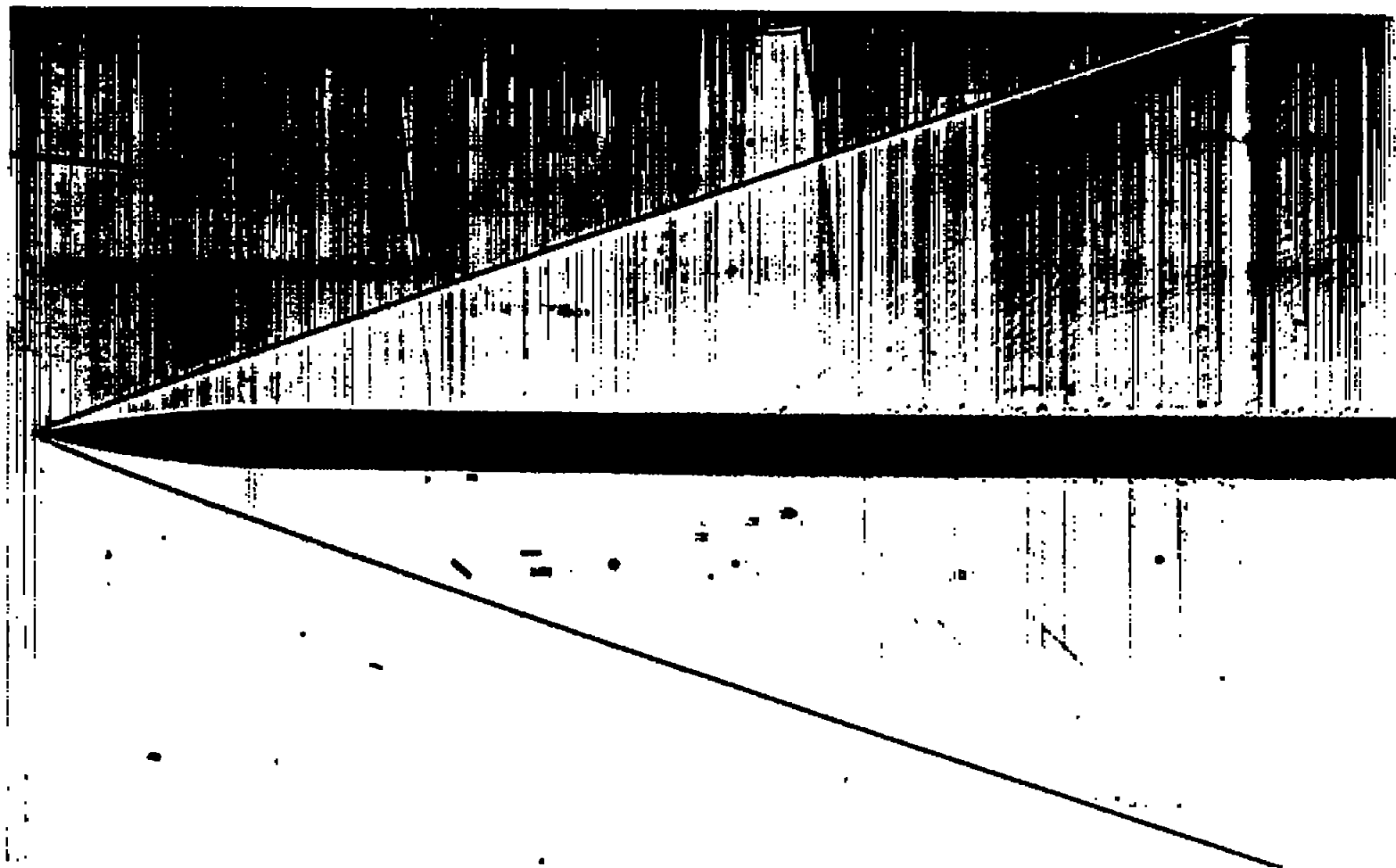
(s) Pencil model;  $M_\infty = 3.6$ ;  $U_e/\nu = 3.6 \times 10^6/\text{in.}$ ;  $H = 5 \text{ } \mu\text{in.}$ ; wind tunnel air-off; parallel light field. Model is slightly bent.

Figure 4.- Continued.



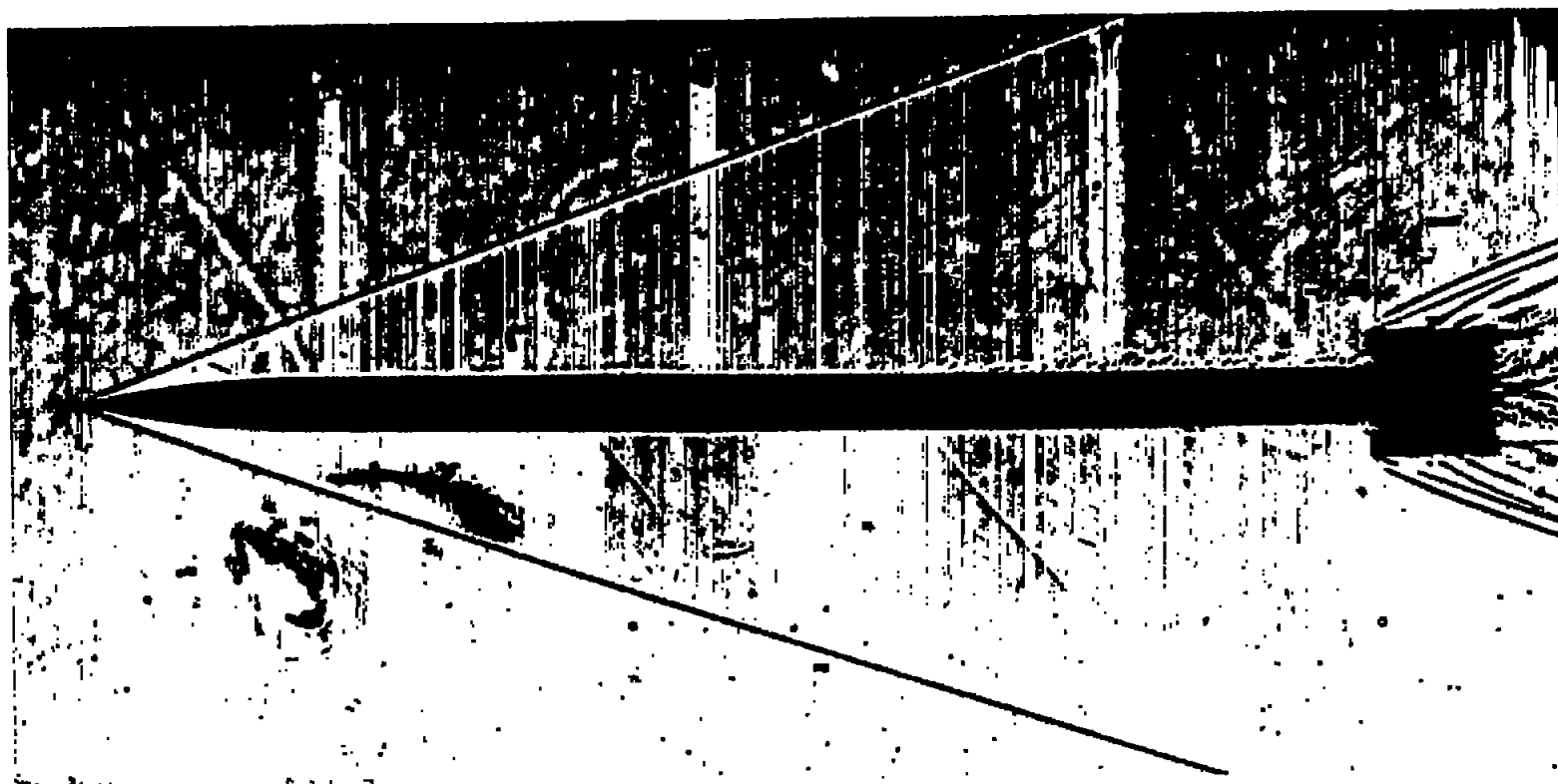
(t) Pencil model;  $M_{\infty} = 3.6$ ;  $U_e/v = 3.6 \times 10^6/\text{in.}$ ;  $H = 5 \mu\text{in.}$ ; wind tunnel air-off; parallel light field.

Figure 4.- Continued.



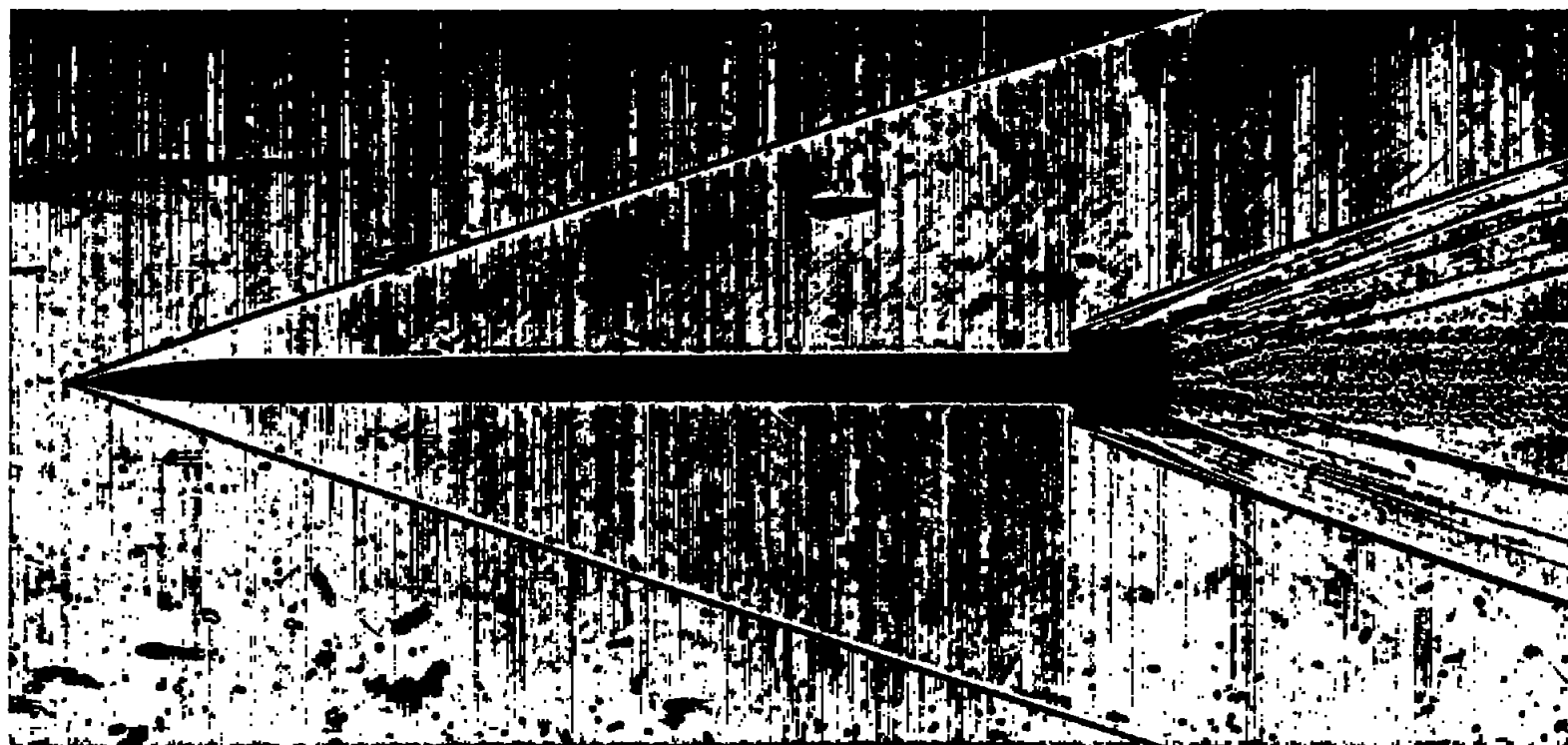
(u) Pencil model;  $M_{\infty} = 3.5$ ;  $U_e/v = 2.1 \times 10^8/\text{in.}$ ;  $H = 10 \text{ } \mu\text{in.}$ ; wind tunnel air-off; conical light field.

Figure 4.- Continued.



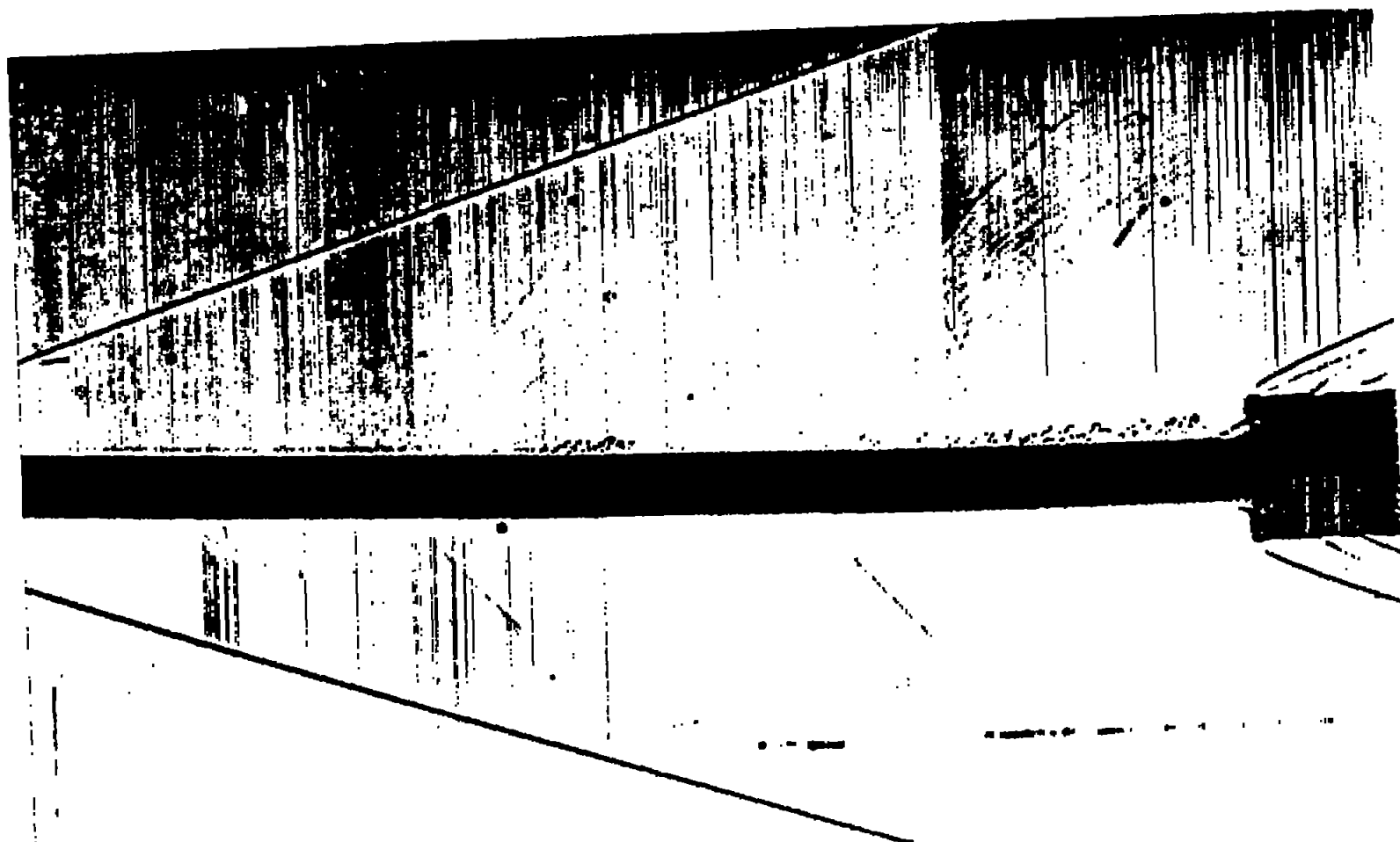
(v) Pencil model;  $M_\infty = 3.5$ ;  $U_e/\nu = 2.0 \times 10^6/\text{in.}$ ;  $H = 10 \text{ } \mu\text{in.}$ ; wind tunnel air-off; parallel light field. Model is slightly bent.

Figure 4.- Continued.



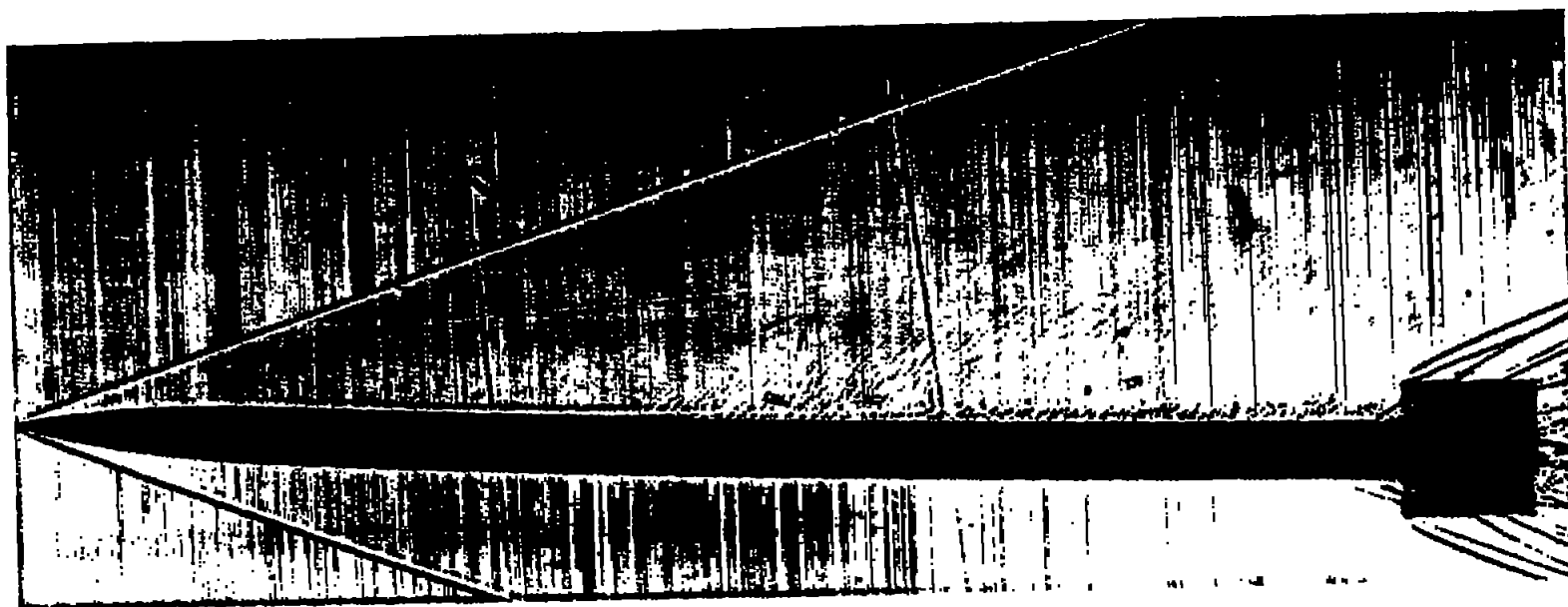
(w) Pencil model;  $M_{\infty} = 3.6$ ;  $U_e/\nu = 3.7 \times 10^6/\text{in.}$ ;  $H = 10 \mu\text{in.}$ ; wind tunnel air-off; parallel light field.

Figure 4.- Continued.



(x) Pencil model;  $M_{\infty} = 3.5$ ;  $U_e/\nu = 2.0 \times 10^6/\text{in.}$ ;  $H = 10 \mu\text{in.}$ ; wind tunnel air-off; conical light field. Model is bent.

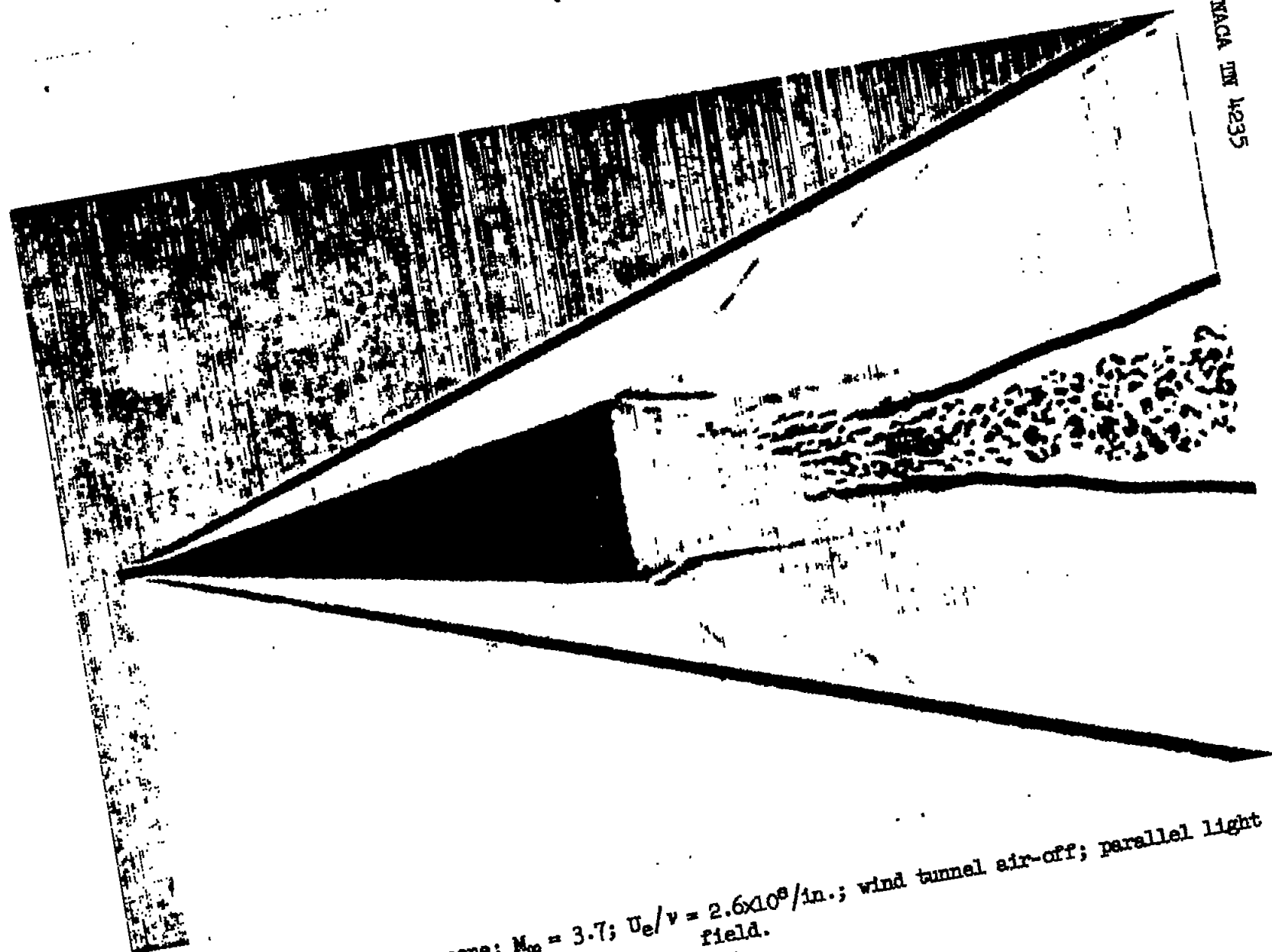
Figure 4.- Continued.



(y) Pencil model;  $M_{\infty} = 3.5$ ;  $U_e/\nu = 2.0 \times 10^8/\text{in.}$ ;  $H = 10 \mu\text{in.}$ ; wind tunnel air-off; conical light field. Model is bent.

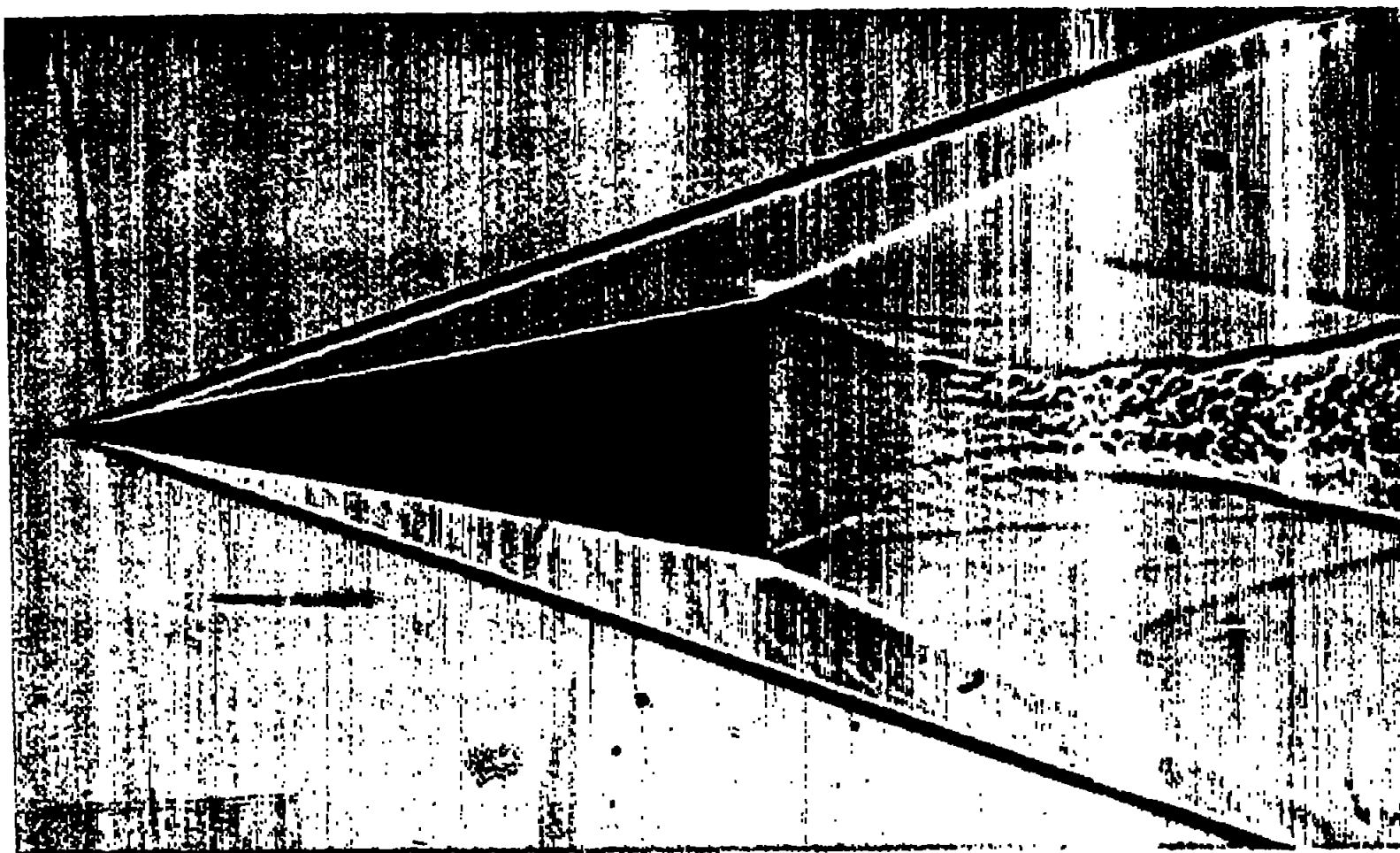
Figure 4.- Continued.





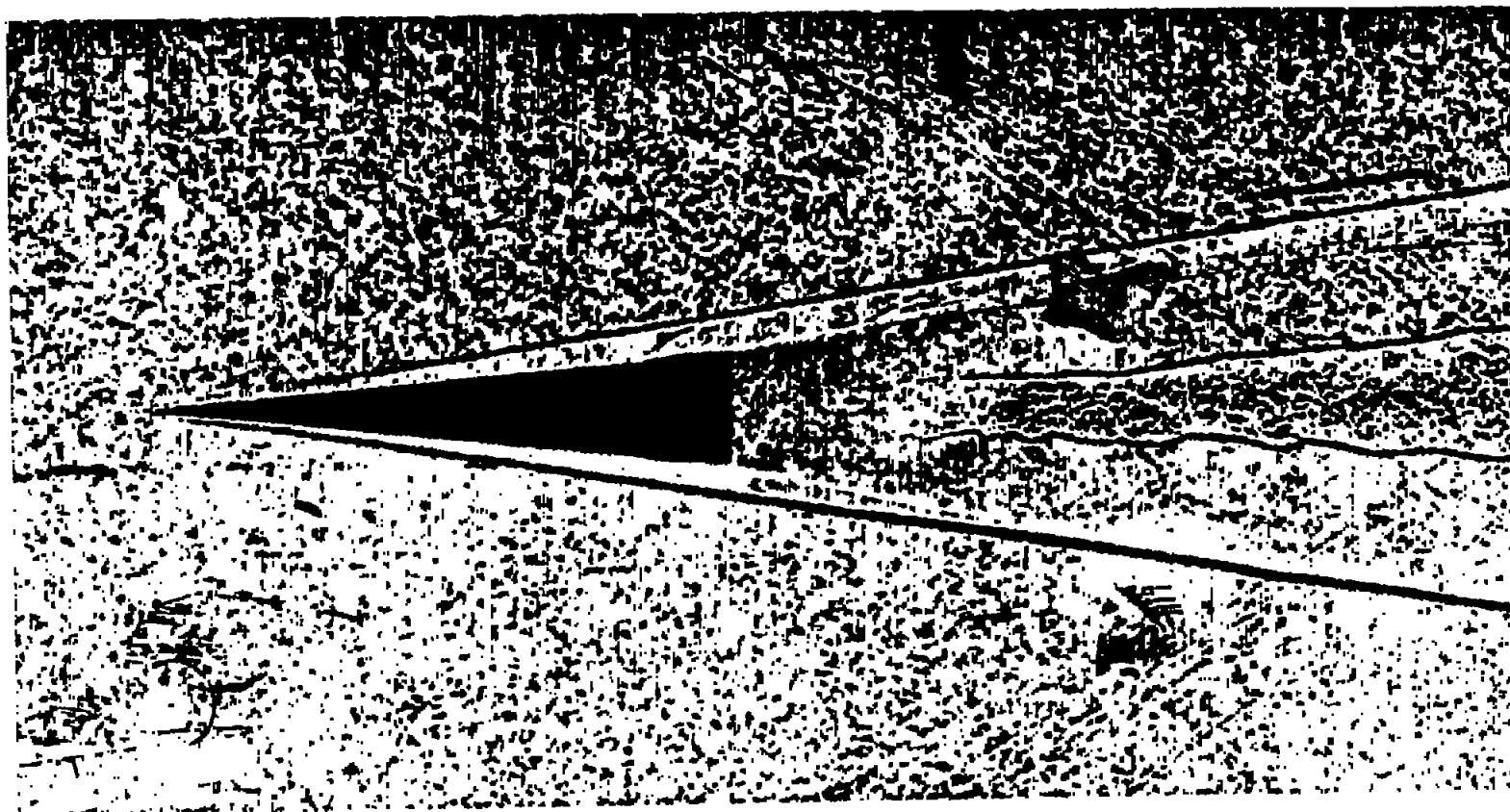
(z)  $19^\circ$  included-angle cone;  $M_\infty = 3.7$ ;  $U_e/v = 2.6 \times 10^8/\text{in.}$ ; wind tunnel air-off; parallel light field.

Figure 4.-- Continued.



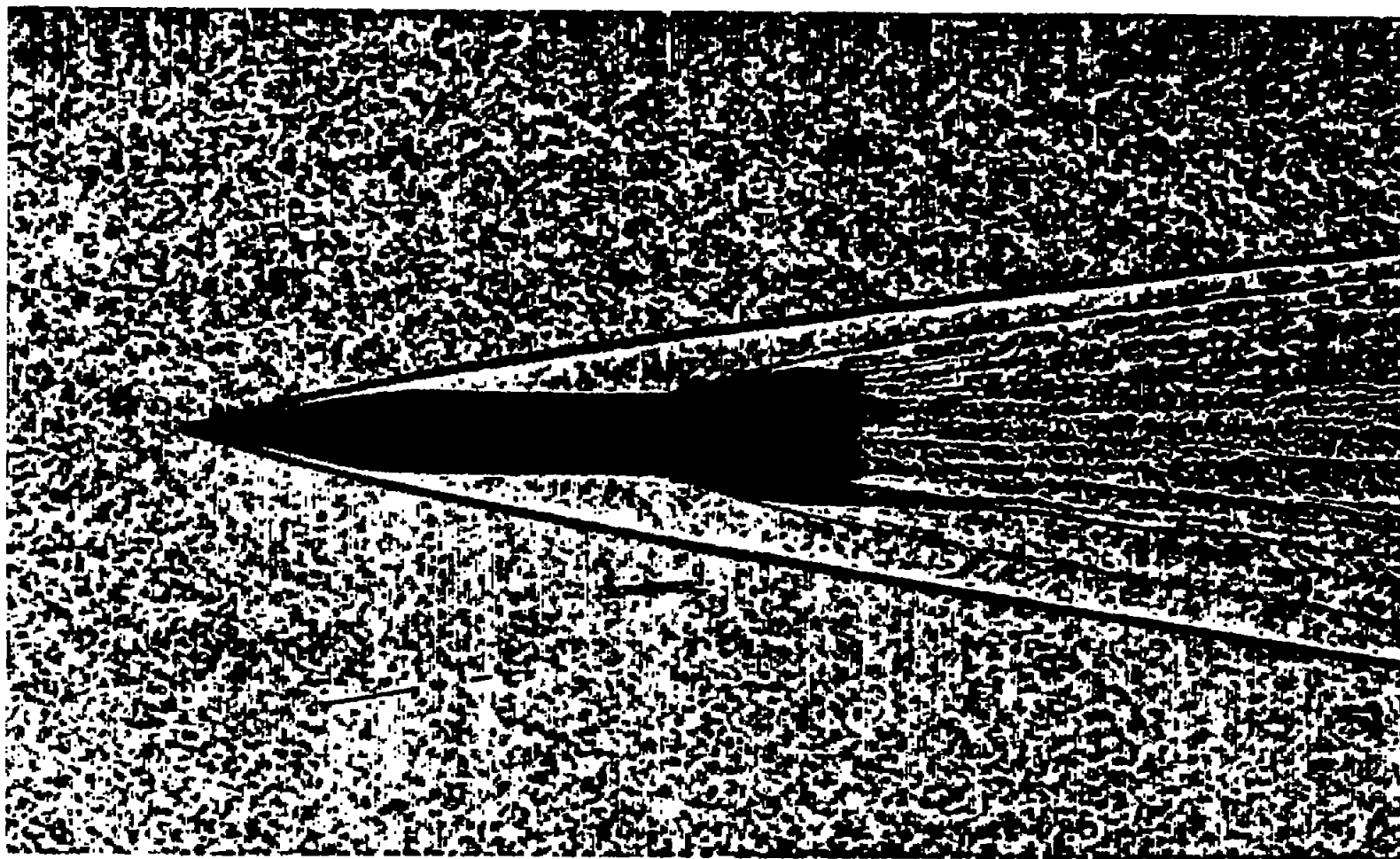
(sa)  $19^\circ$  included-angle cone;  $M_\infty = 3.8$ ;  $U_e/v = 2.3 \times 10^8/\text{in.}$ ; wind tunnel air-off; conical light field.

Figure 4.- Continued.



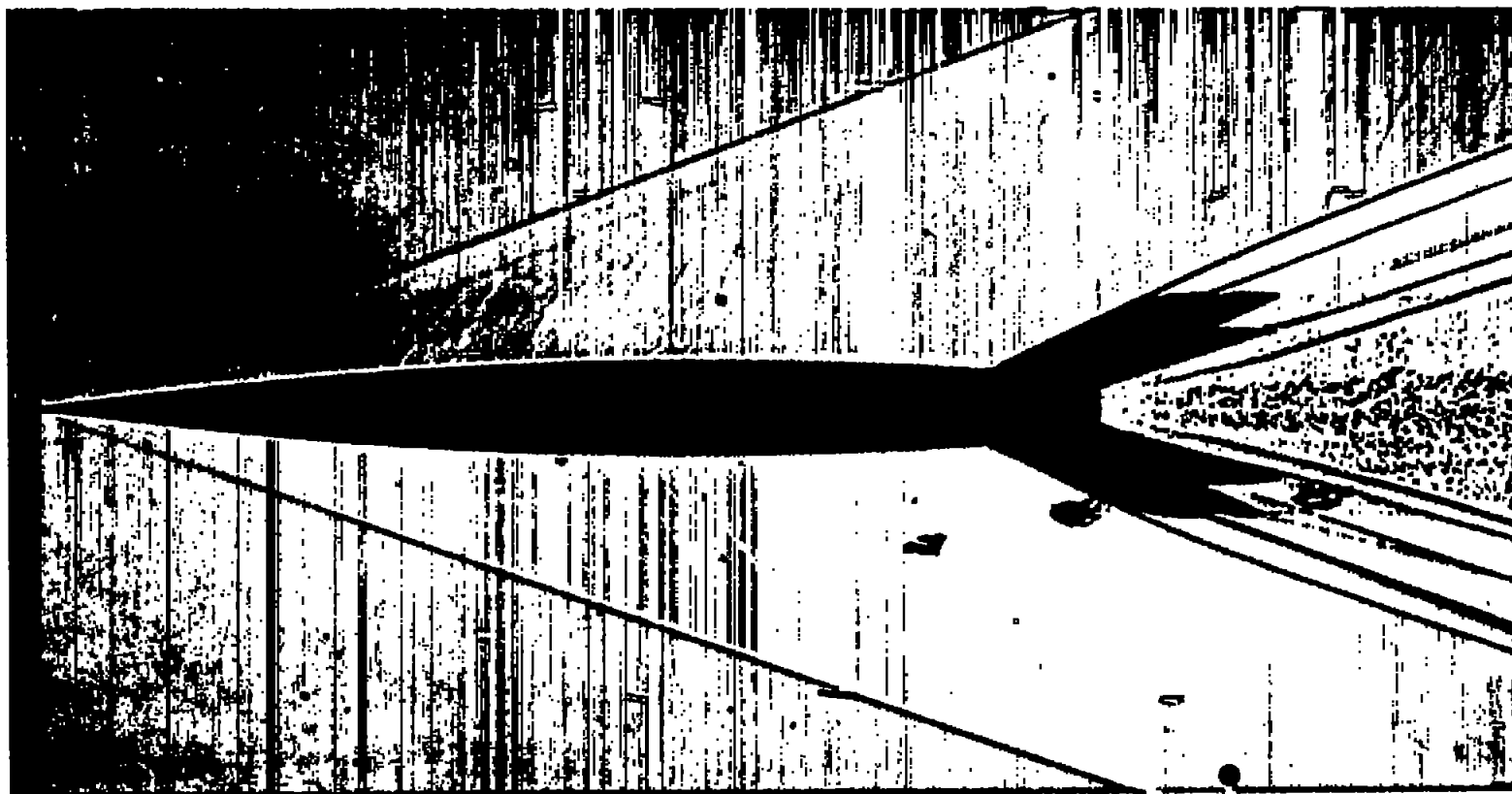
(bb)  $10^\circ$  included-angle cone;  $M_\infty = 10$ ;  $U_\infty/\nu = 3.9 \times 10^6/\text{in.}$ ; wind tunnel air-on; parallel light field.

Figure 4.- Continued.



(cc) A-4;  $M_\infty = 10.0$ ;  $U_e/v = 6.35 \times 10^6/\text{in.}$ ; wind tunnel air-on; parallel light field.

Figure 4.- Continued.



(dd) RM-10;  $M_{\infty} = 3.1$ ;  $U_e/v = 1.8 \times 10^6/\text{in.}$ ; wind tunnel air-off; conical light field.

Figure 4.- Concluded.

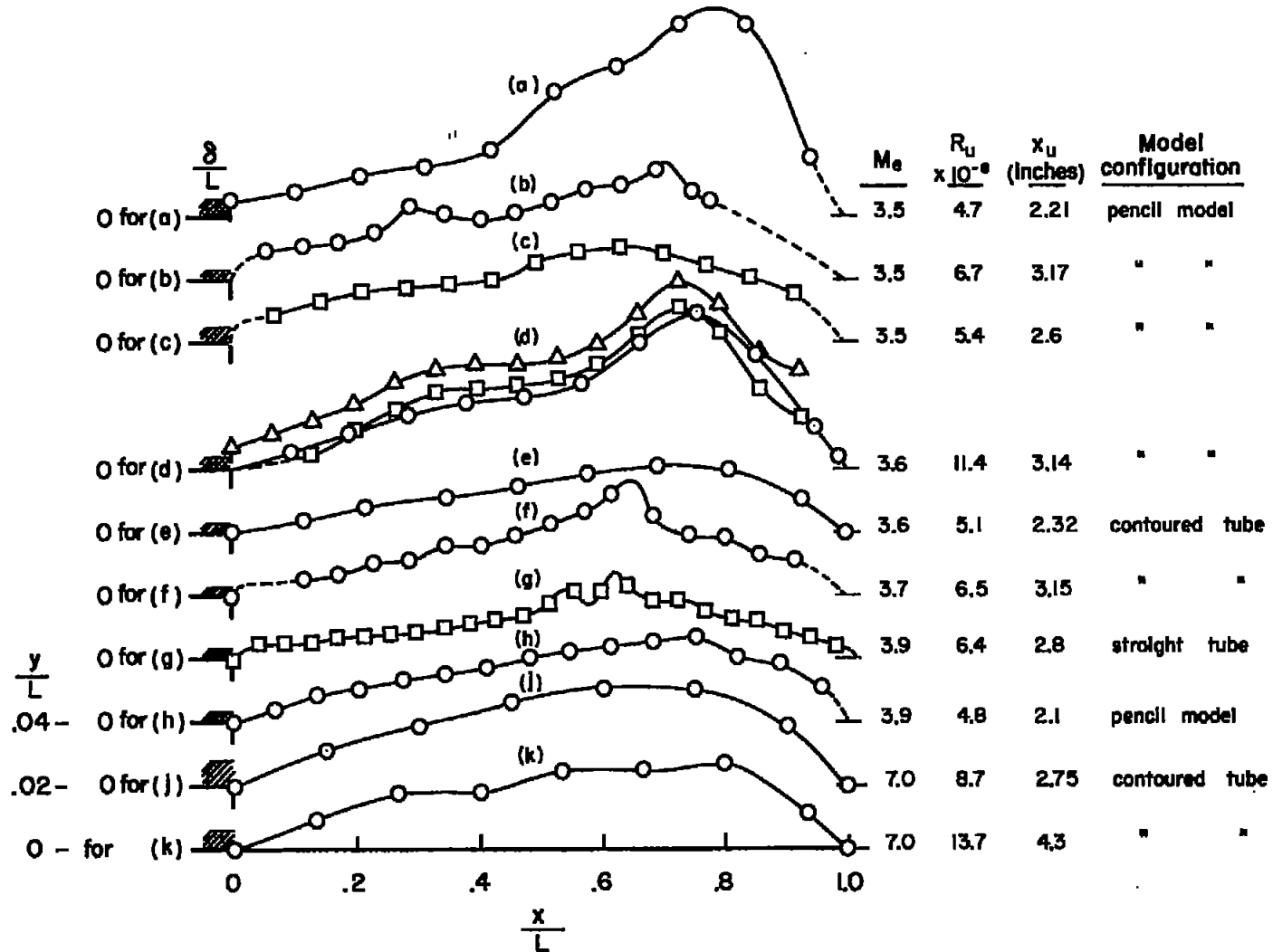
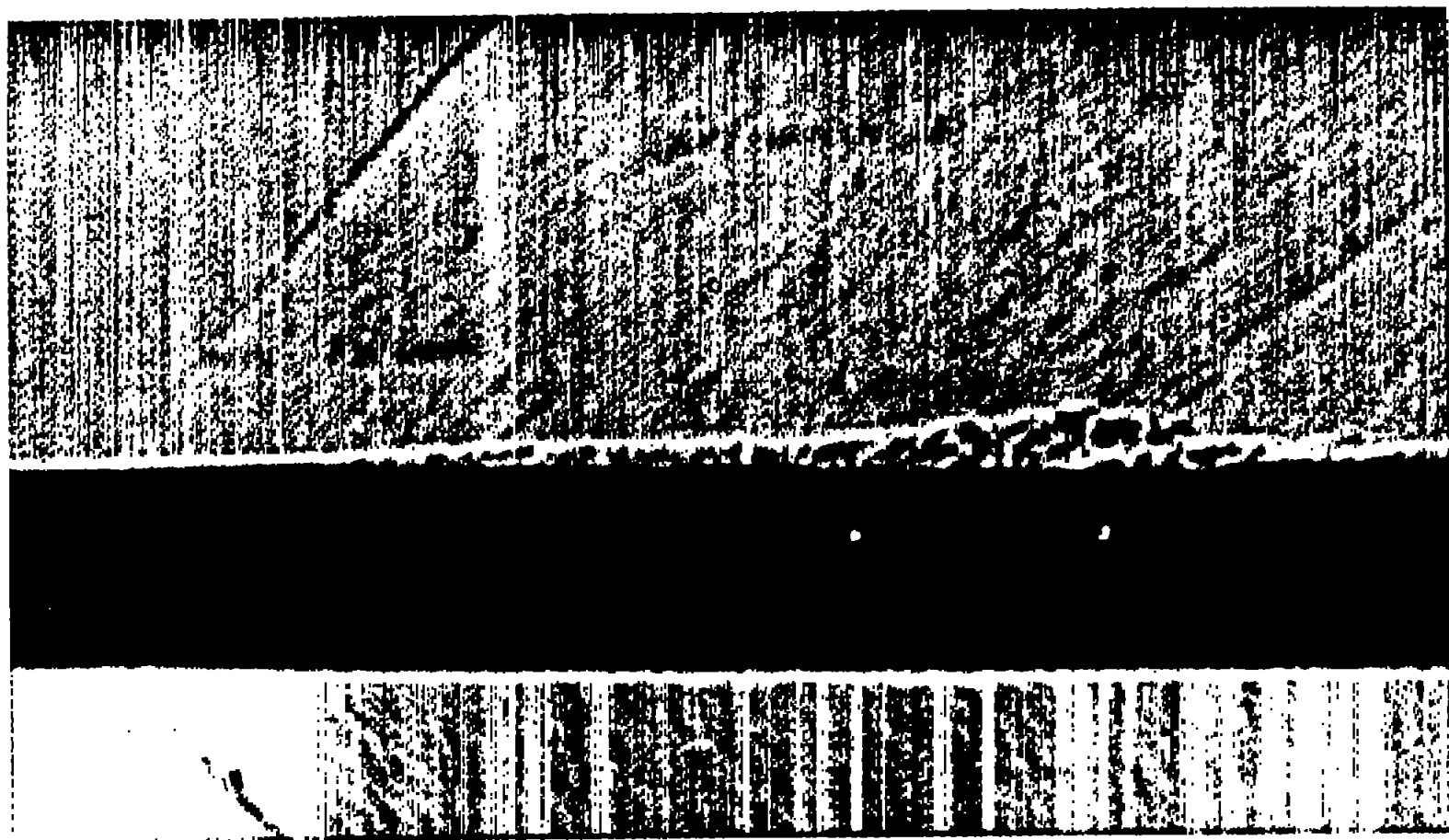
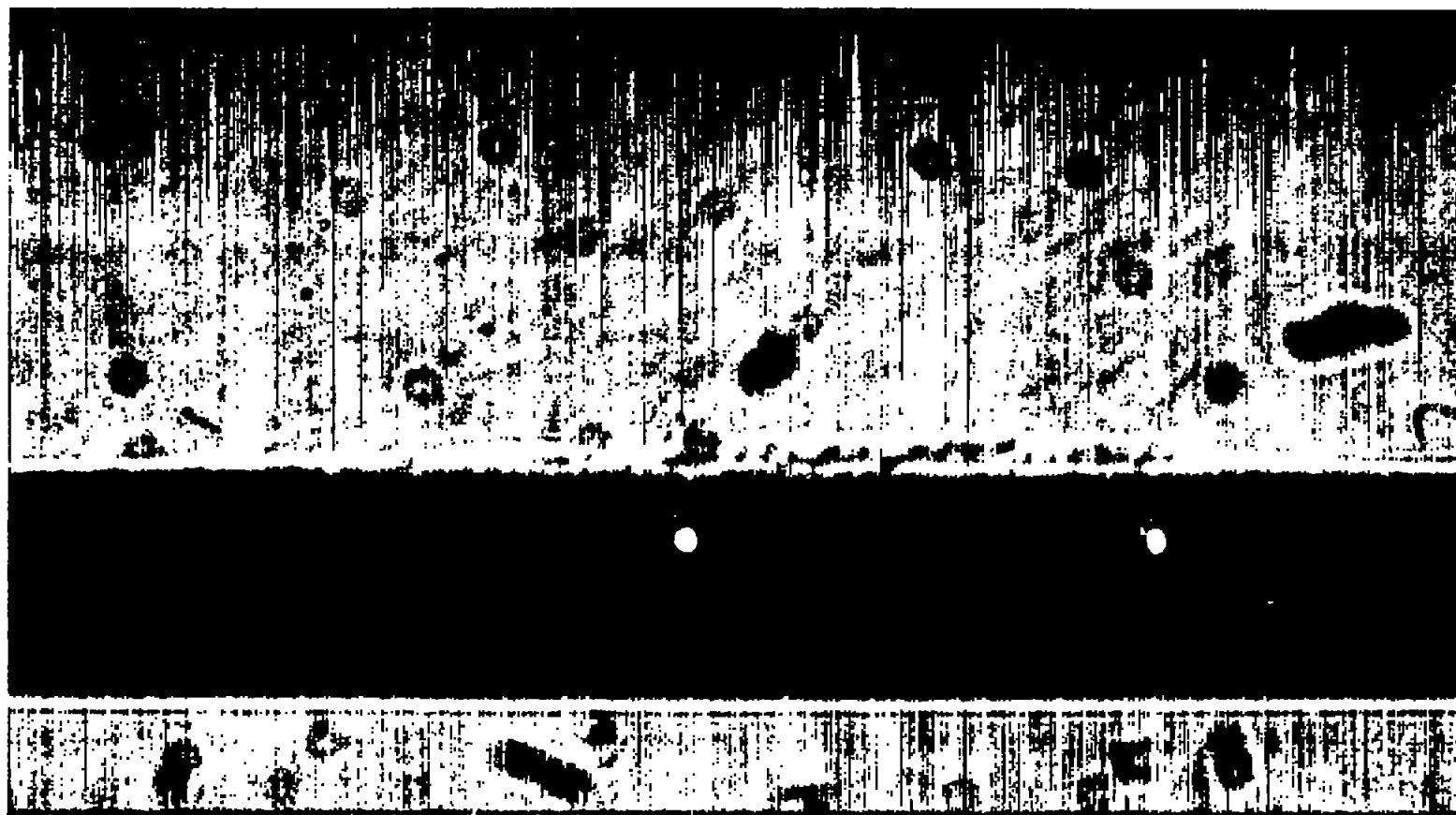


Figure 5.- Center-line thickness distributions of bursts.



(a) Burst on pencil model; 5X.

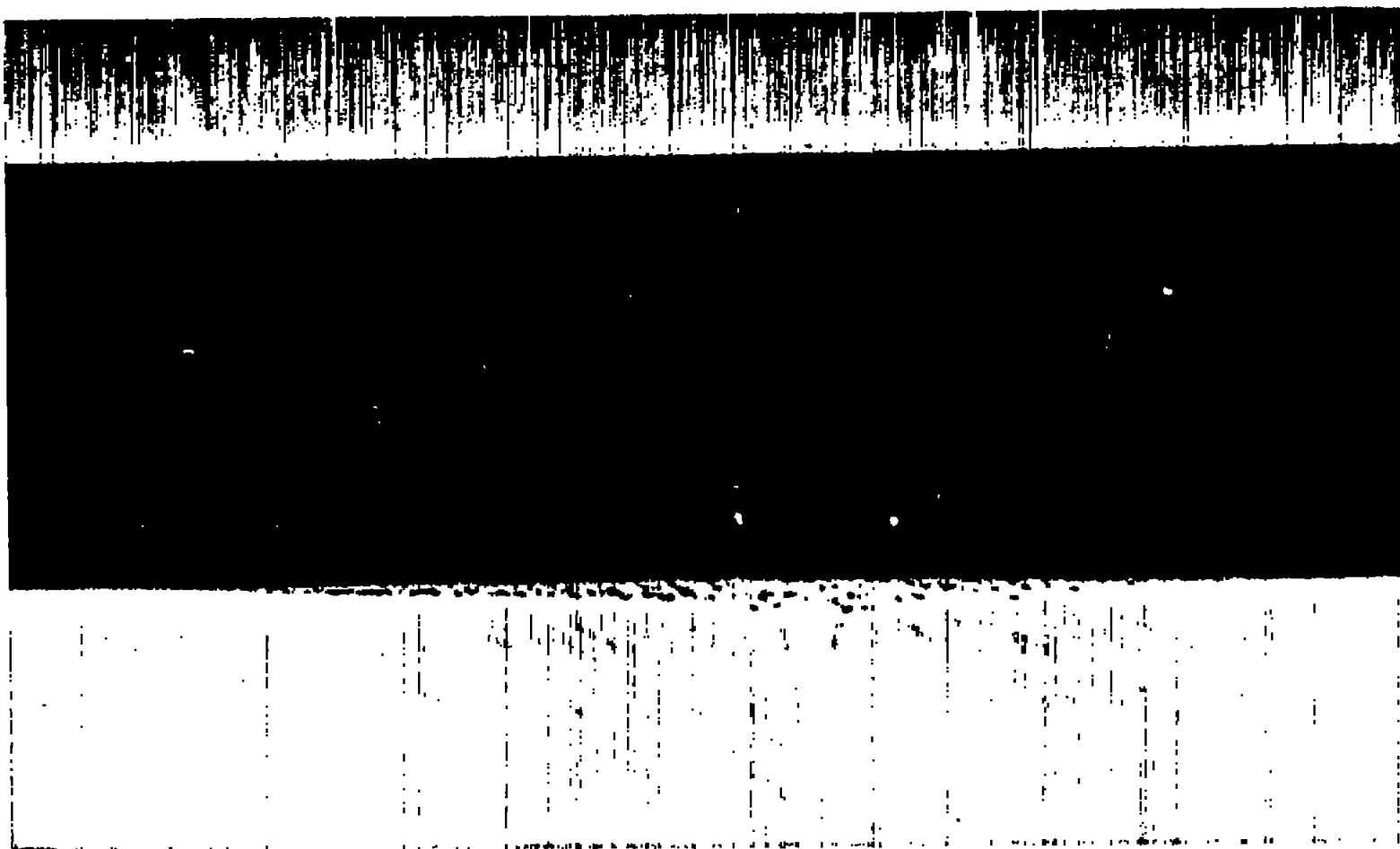
Figure 6.- Enlarged shadowgraph profiles of bursts.



(b) Burst on pencil model; 5.5X.

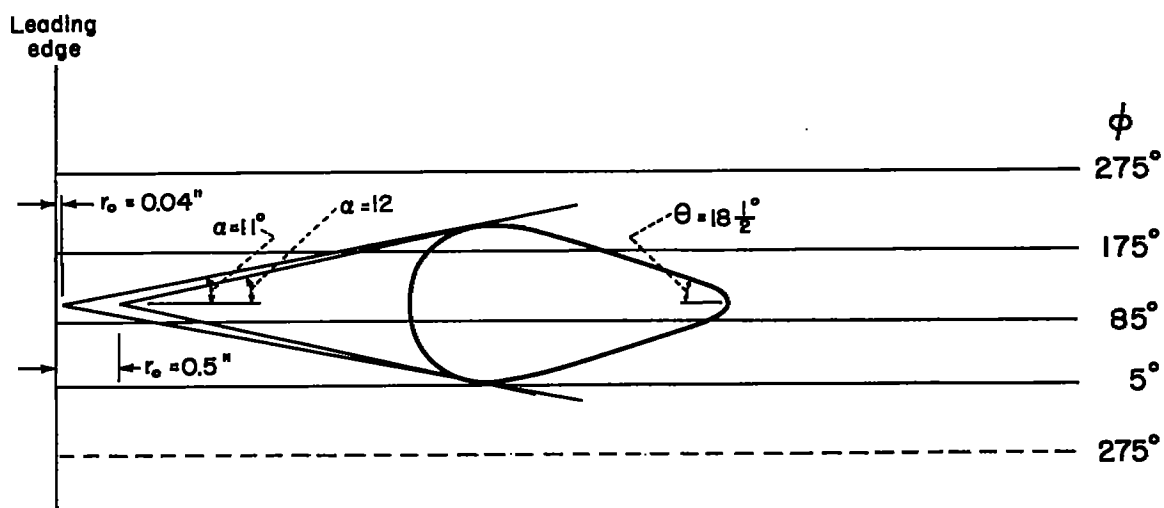
Figure 6.- Continued.



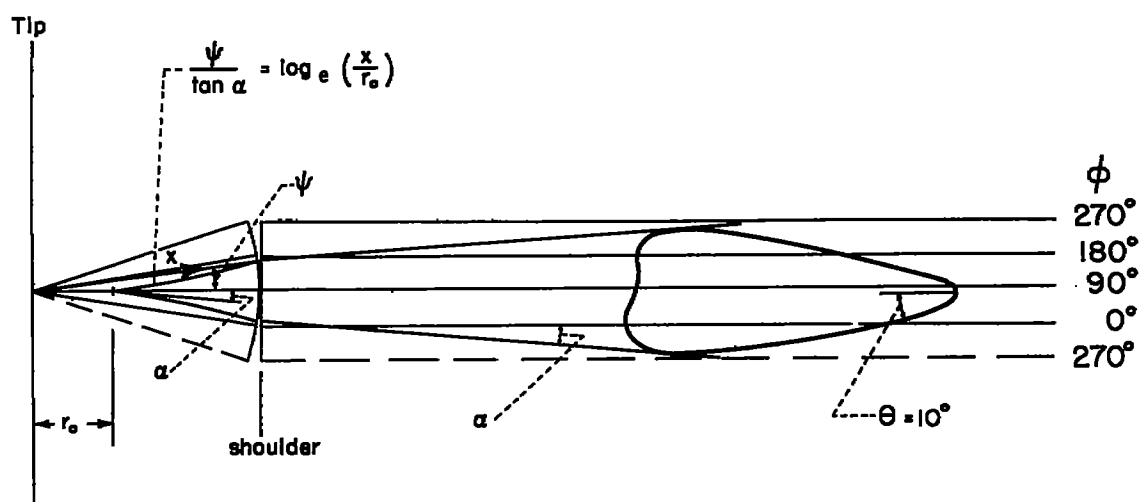


(c) Burst on straight tube; 3.1X.

Figure 6.- Concluded.

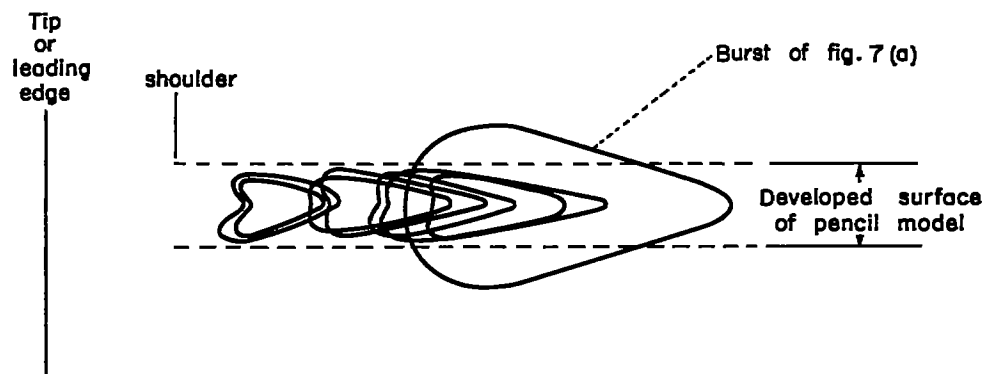


(a) Developed plan form of burst on the straight tube;  
 $M_e = 3.9$ ;  $U_e/\nu = 2.3 \times 10^6/\text{in.}$

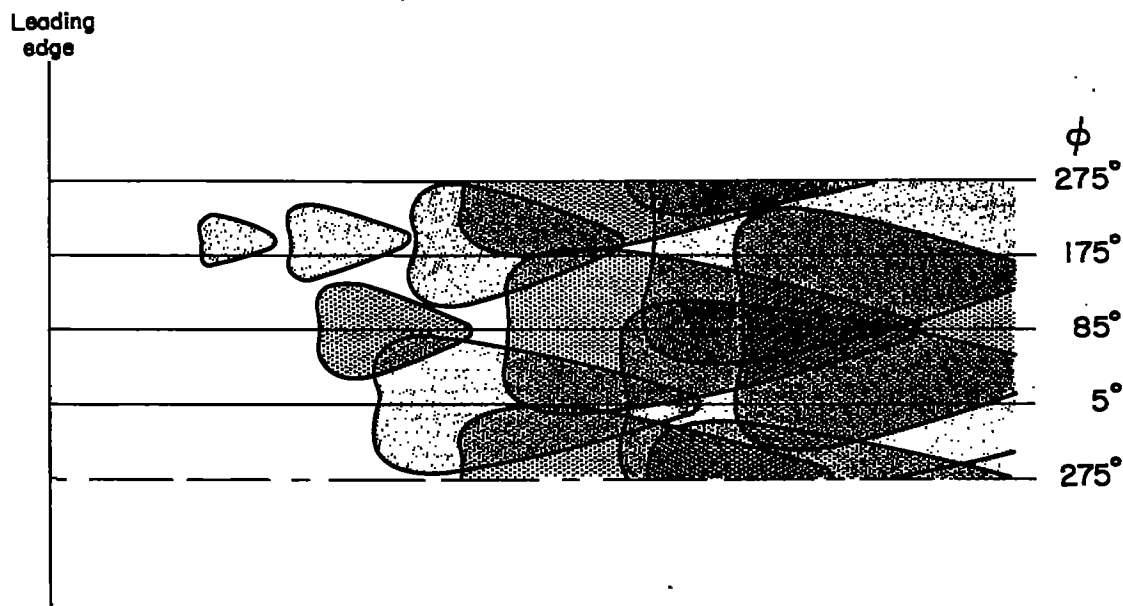


(b) Developed plan form of burst on the pencil model;  
 $M_e = 3.5$ ;  $U_e/\nu = 2.0 \times 10^6/\text{in.}$

Figure 7.- Burst plan forms determined from shadowgraphs.



(c) Composite of developed burst plan form.



(d) Distribution of bursts on developed surface of contoured tube.

Figure 7.- Concluded.

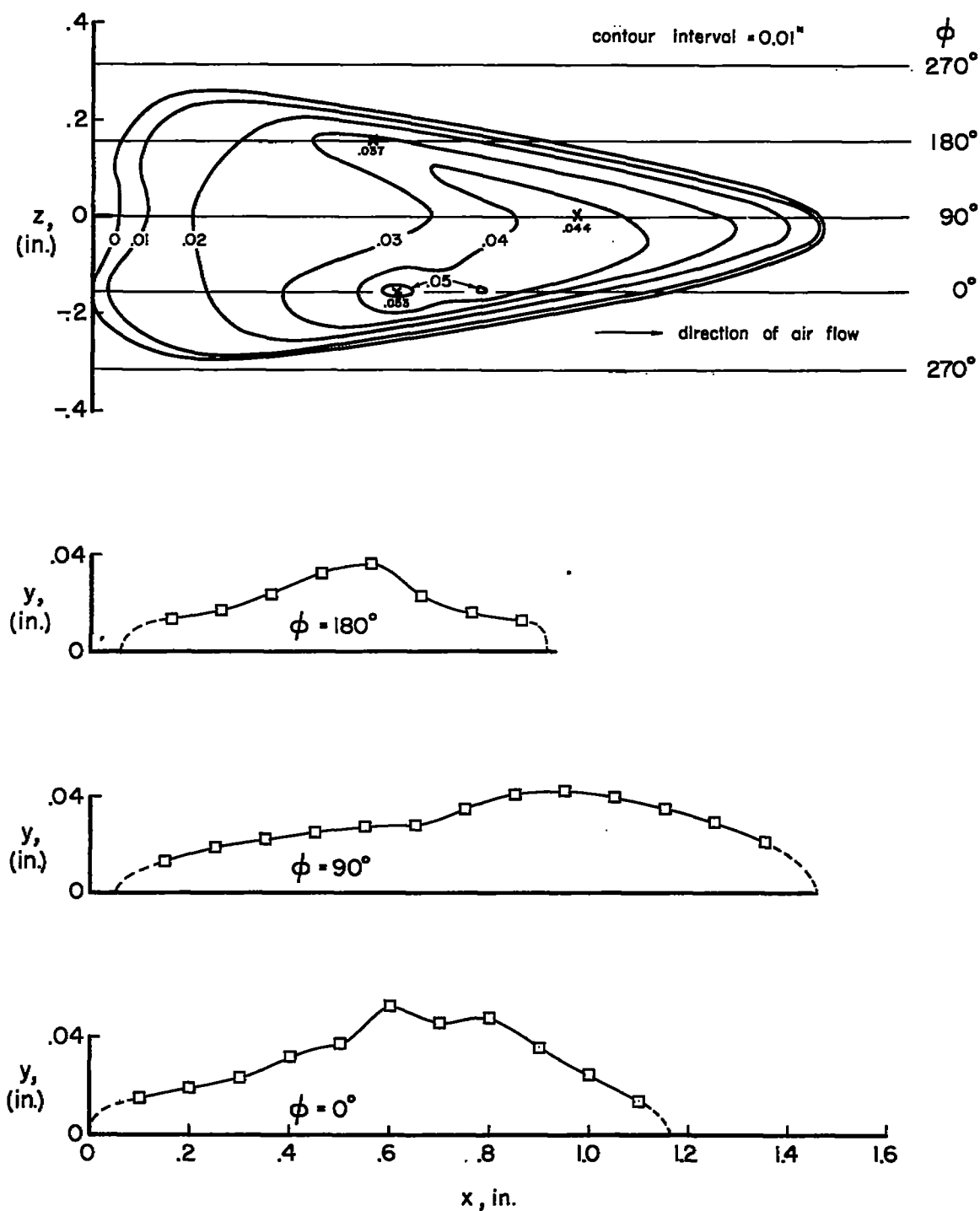


Figure 8.- Contour map and meridian profiles of a burst on the pencil model;  $M_e = 3.5$ ;  $u_e/\nu = 2.0 \times 10^6/\text{in.}$

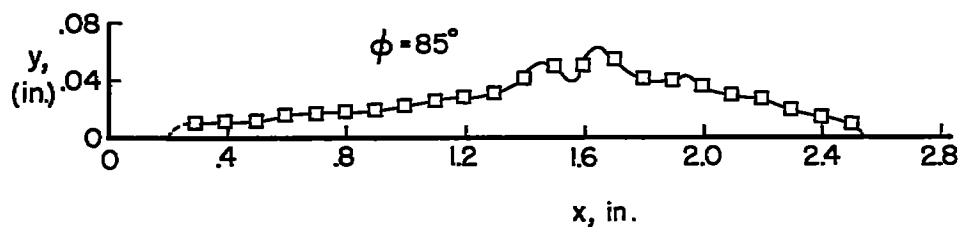
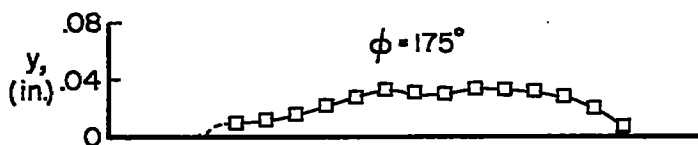
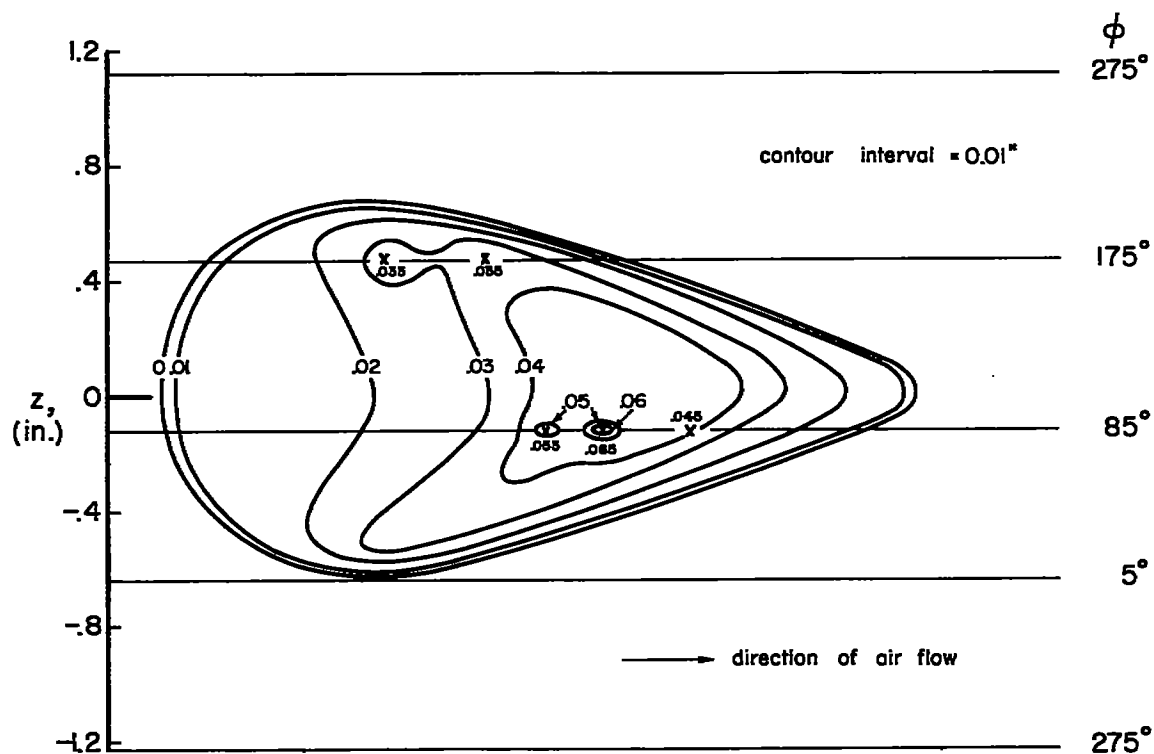
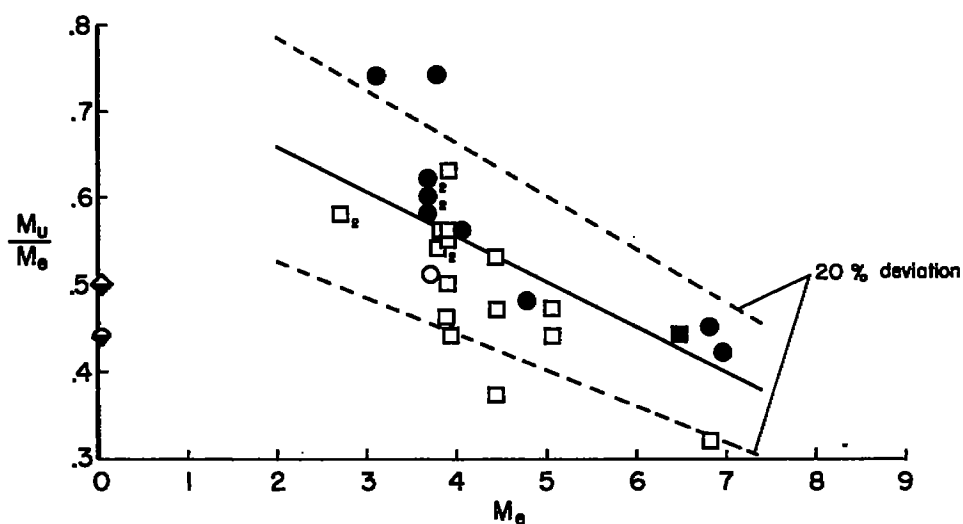


Figure 9.- Contour map and meridian profiles of a burst on the straight tube;  $M_e = 3.9$ ;  $U_e/\nu = 2.3 \times 10^6/\text{in.}$



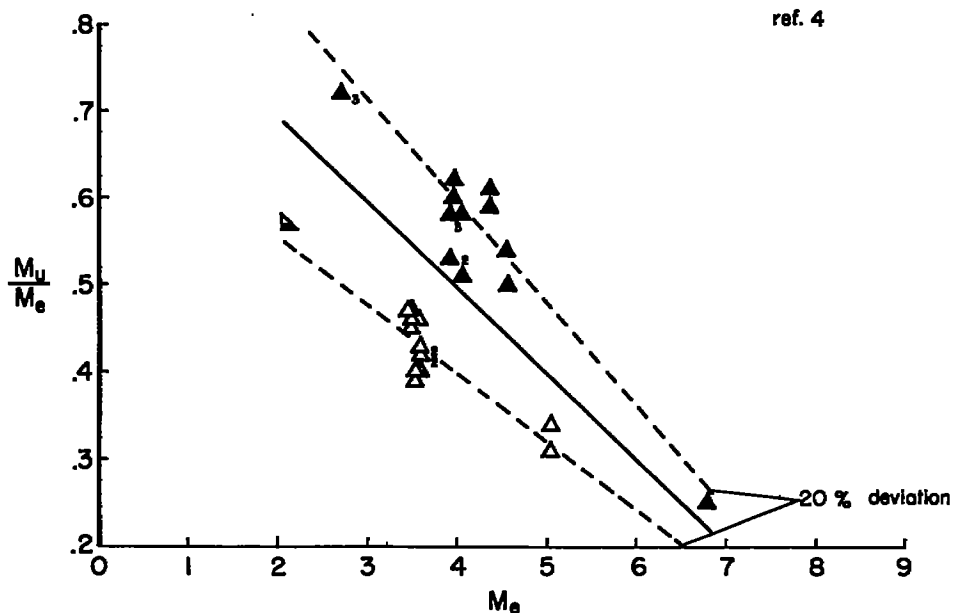
(a) Two - dimensional surfaces

● ■ ▲ rough surface  
○ □ △ smooth surface

Note: Subscript denotes number  
of observations giving  
identical results.

$u_{e/y} \times 10^{-3}, \text{ in.}^{-1}$   
1.7 - 3.2 < 1.7

○ Contoured tube  
□ Straight tube  
△ Pencil model  
◆ Flat plate, ref. 5  
◇ " " , ref. 10  
▲ 20° incl. ∠ cone - cylinder,  
ref. 4



(b) Three - dimensional surfaces

Figure 10.- Variation of Mach number ratio,  $M_u/M_e$ , with  
local Mach number.

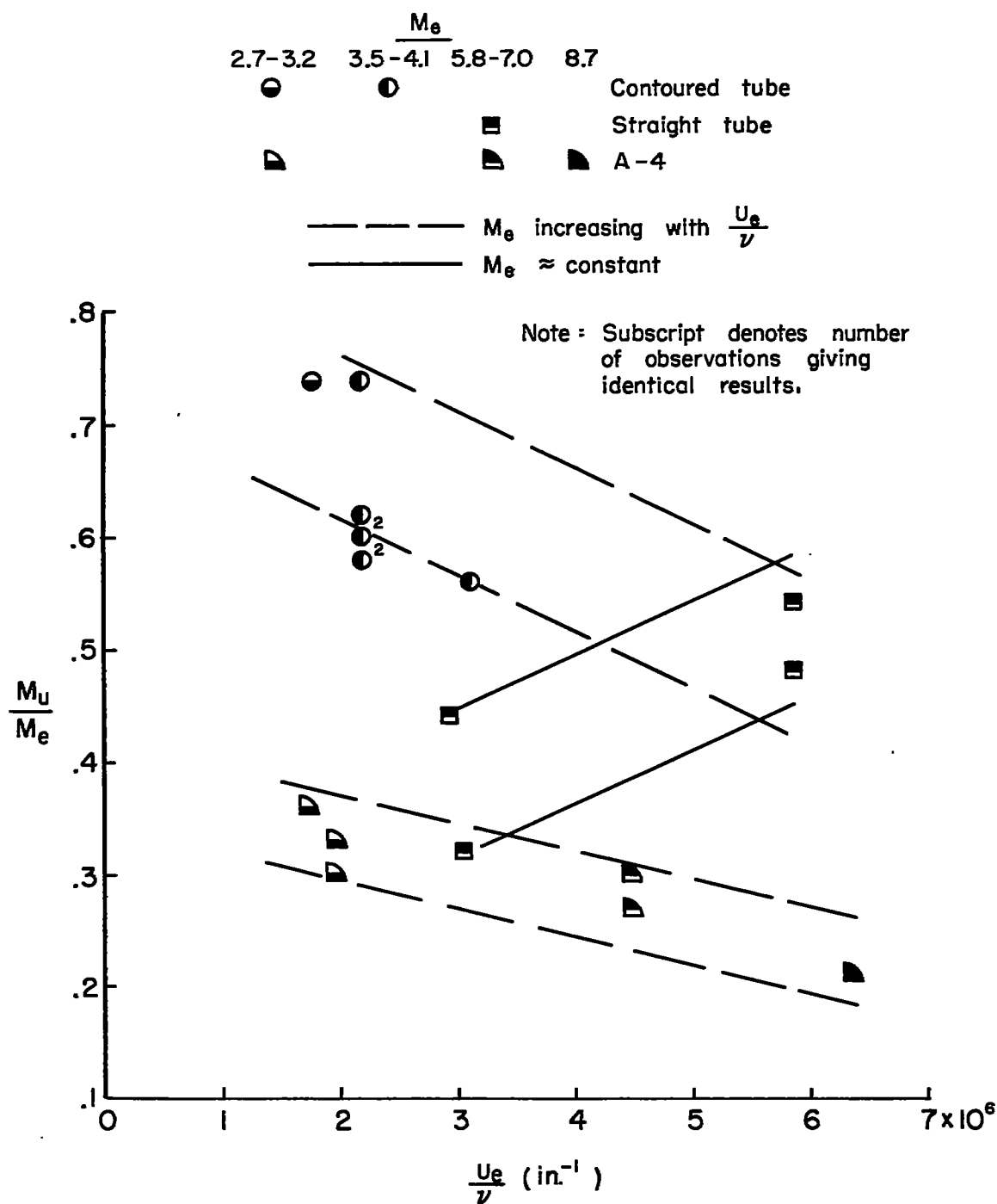


Figure 11.— Variation of Mach number ratio,  $\frac{M_u}{M_e}$ , with unit Reynolds number.

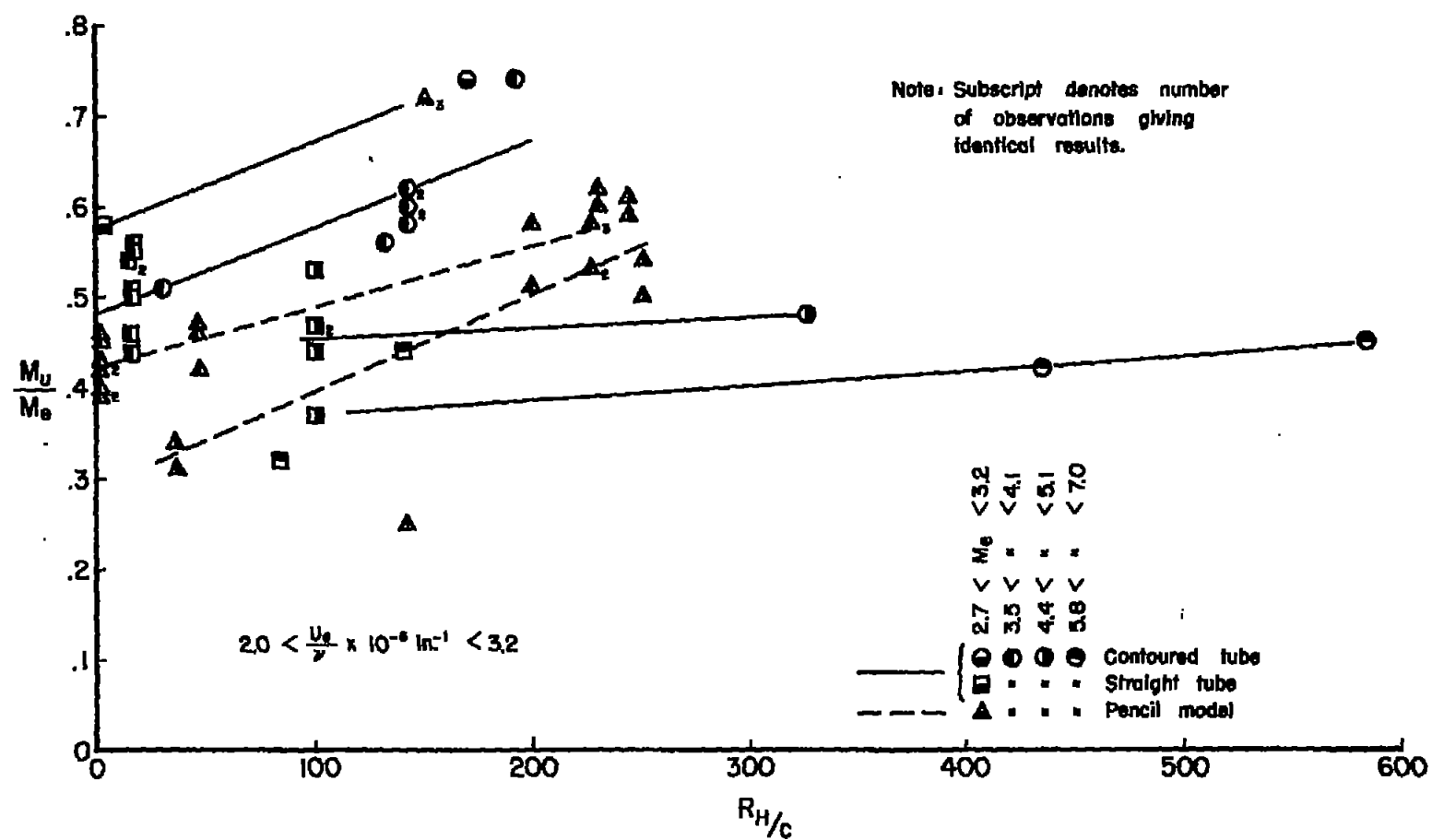


Figure 12.- Variation of Mach number ratio,  $M_u/M_e$ , with surface roughness parameter,  $R_H/c$ .



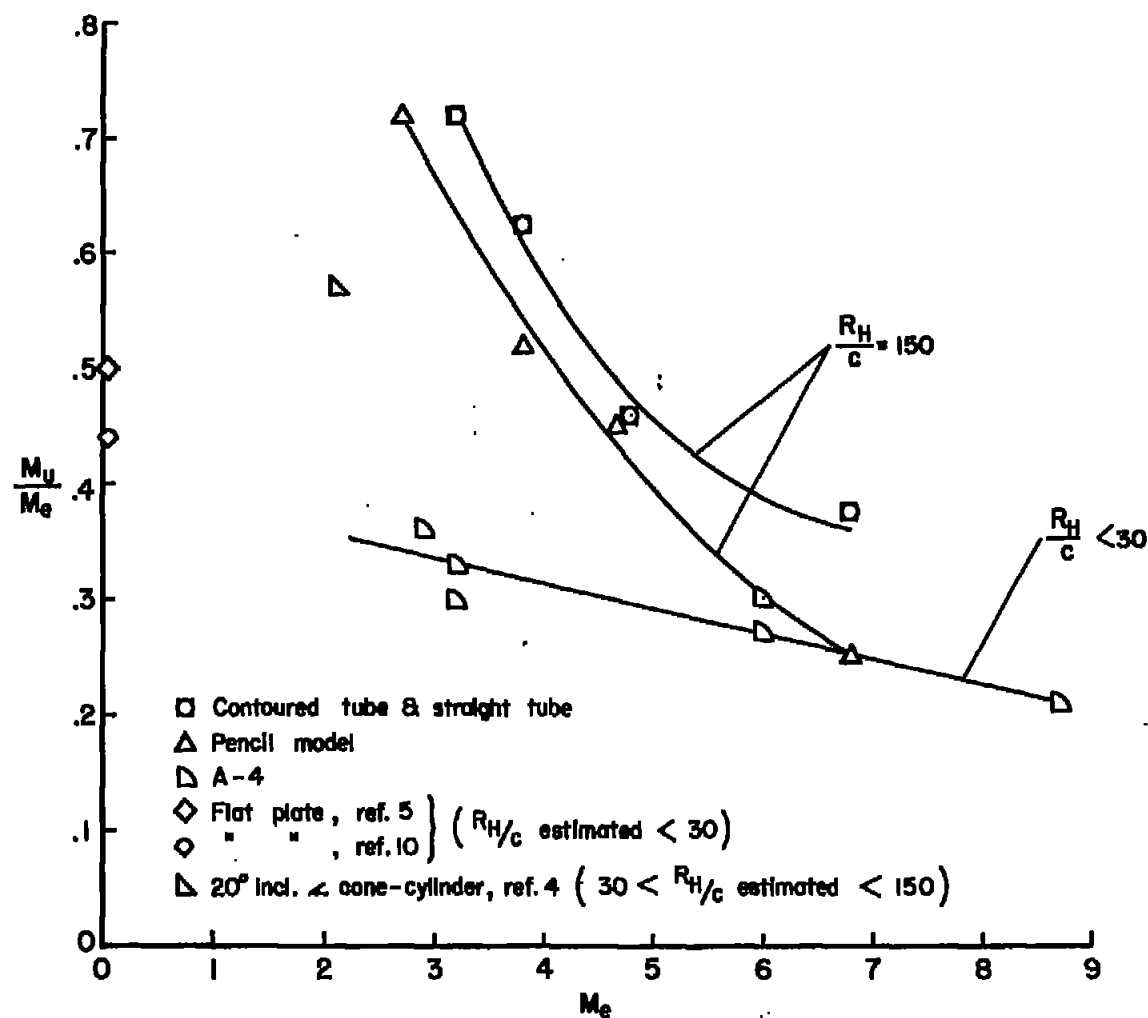


Figure 13.- Variation of Mach number ratio,  $M_u/M_e$ , with local Mach number, with roughness parameter,  $R_H/c$ , held constant.

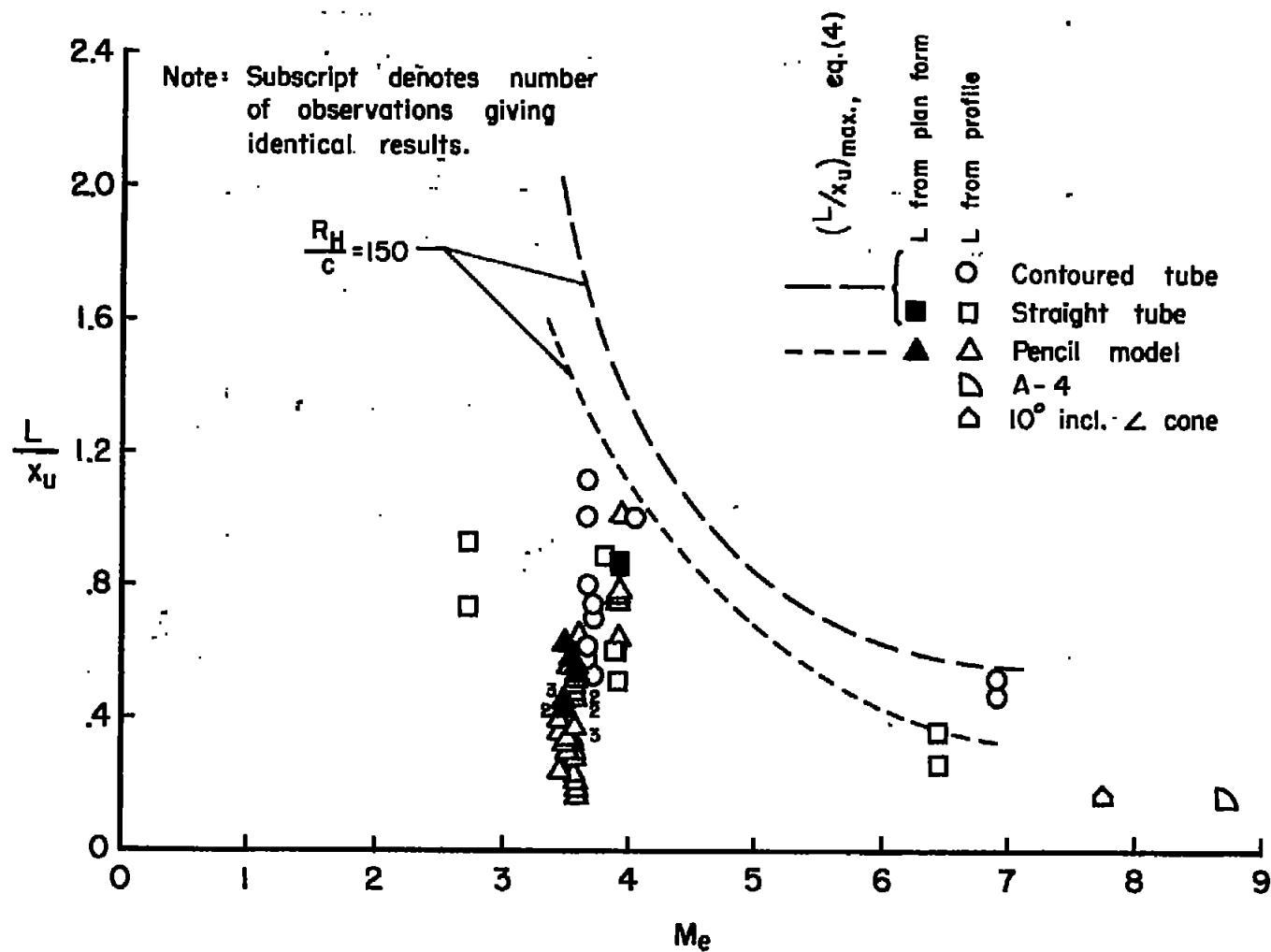
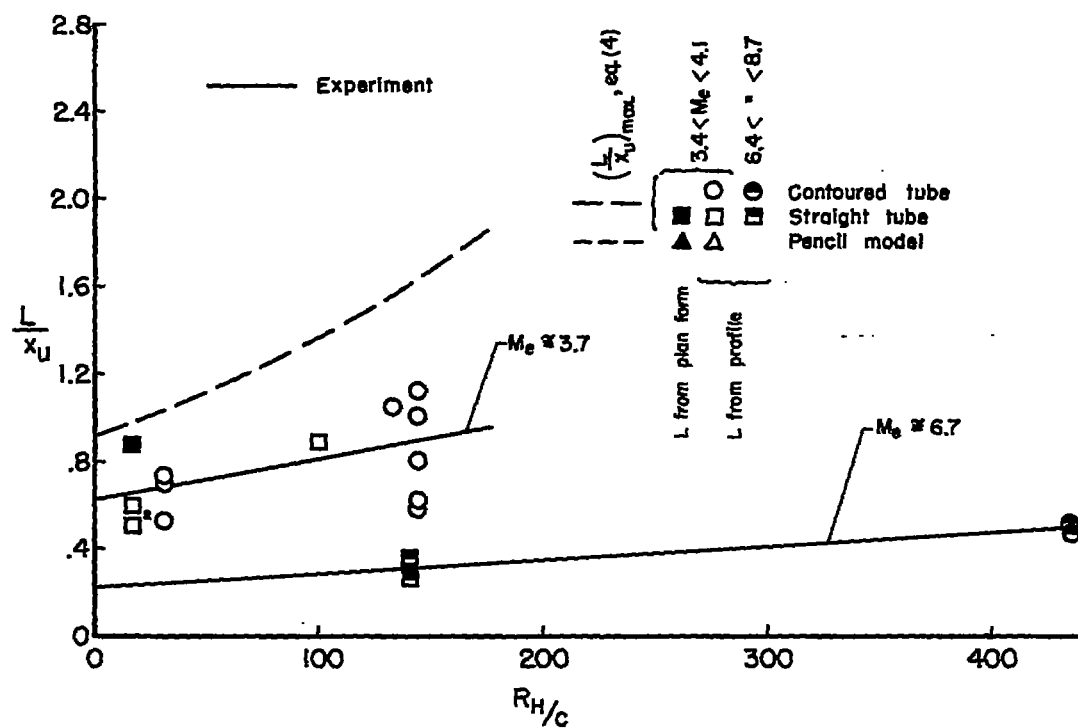
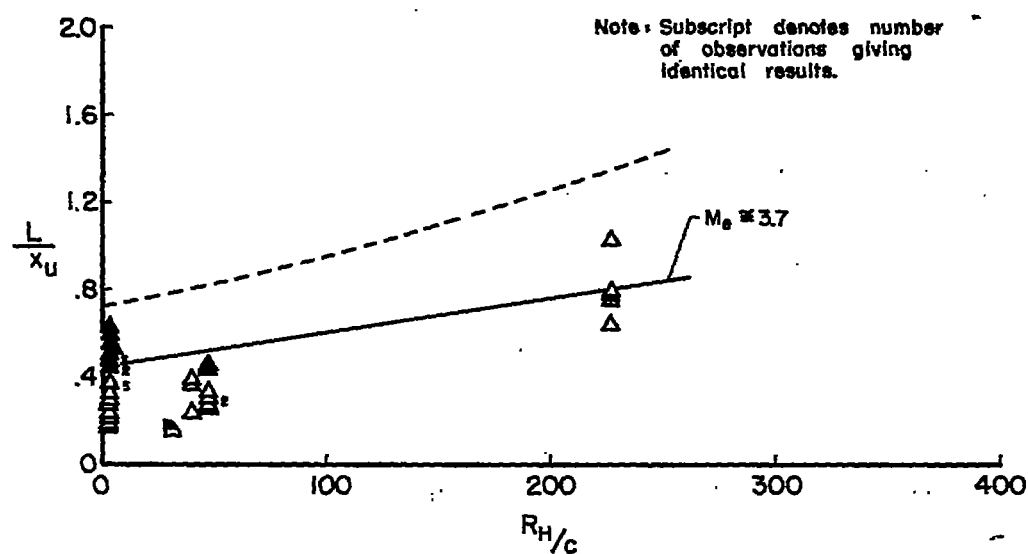


Figure 14.- Variation of relative burst length,  $L/x_u$ , with local Mach number.

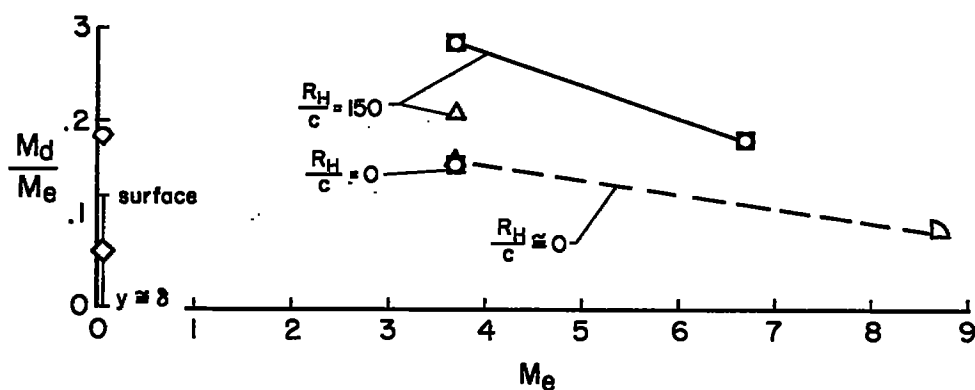


(a) Two-dimensional surfaces

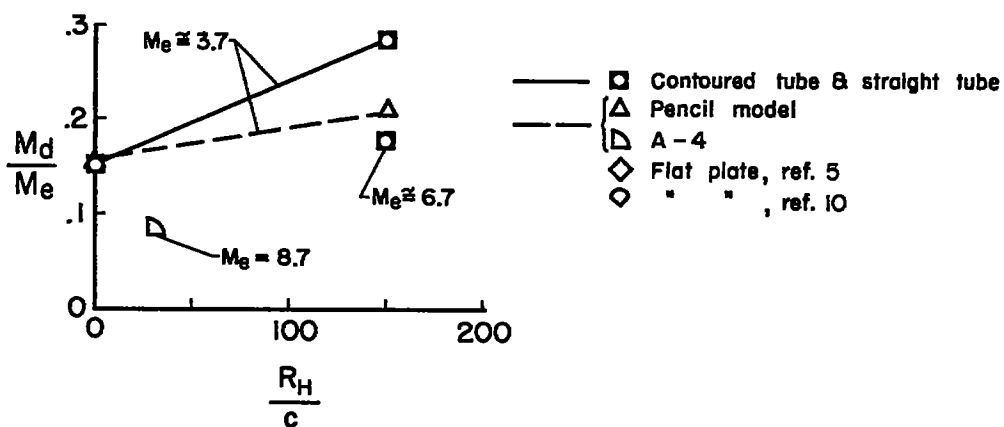


(b) Three-dimensional surfaces

Figure 15. - Variation of relative burst length,  $L/x_u$ , with roughness parameter,  $R_H/c$ .

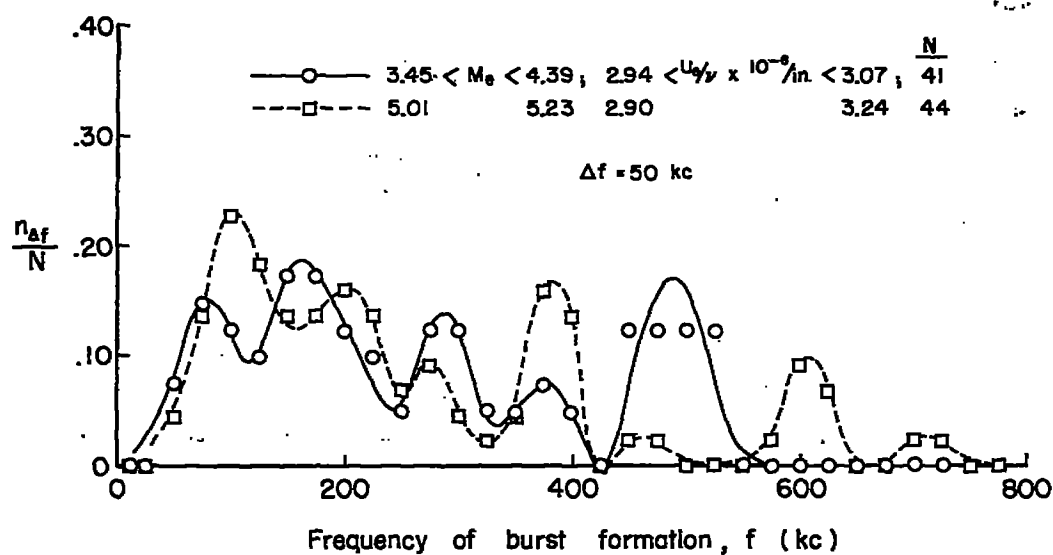


(a) Effect of Mach number

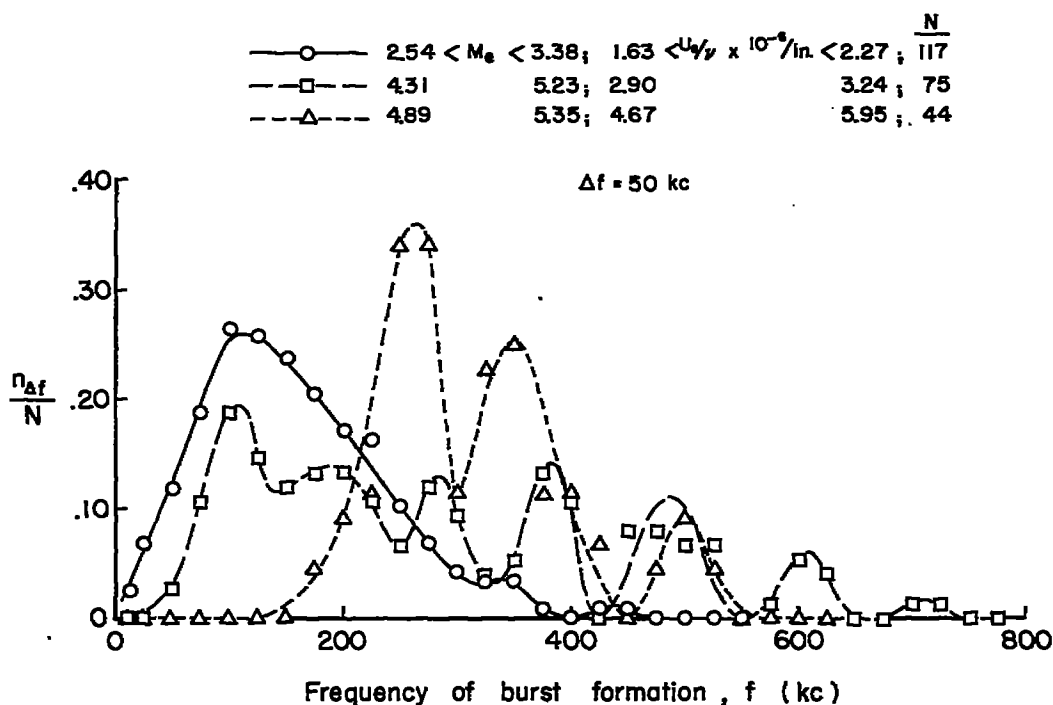


(b) Effect of surface roughness

Figure 16.— Variation of Mach number ratio,  $M_d/M_e$ , with local Mach number and roughness parameter.



(a) Effect of Mach number



(b) Effect of Reynolds number

Figure 17.— Spectrums of formation frequency of bursts on the  $19^\circ$  included angle cone.

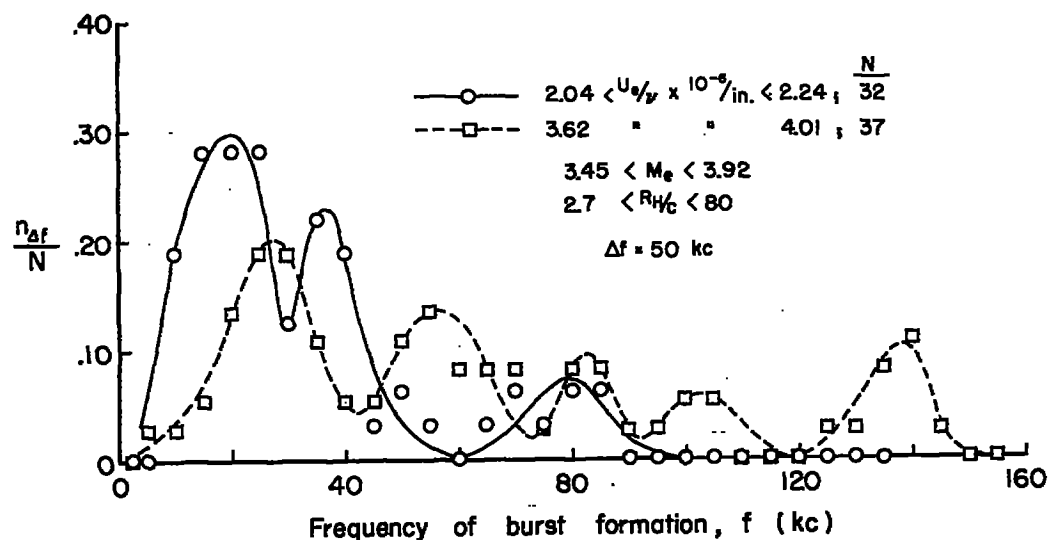


Figure 18.- Spectrums of formation frequency of bursts on the pencil models.

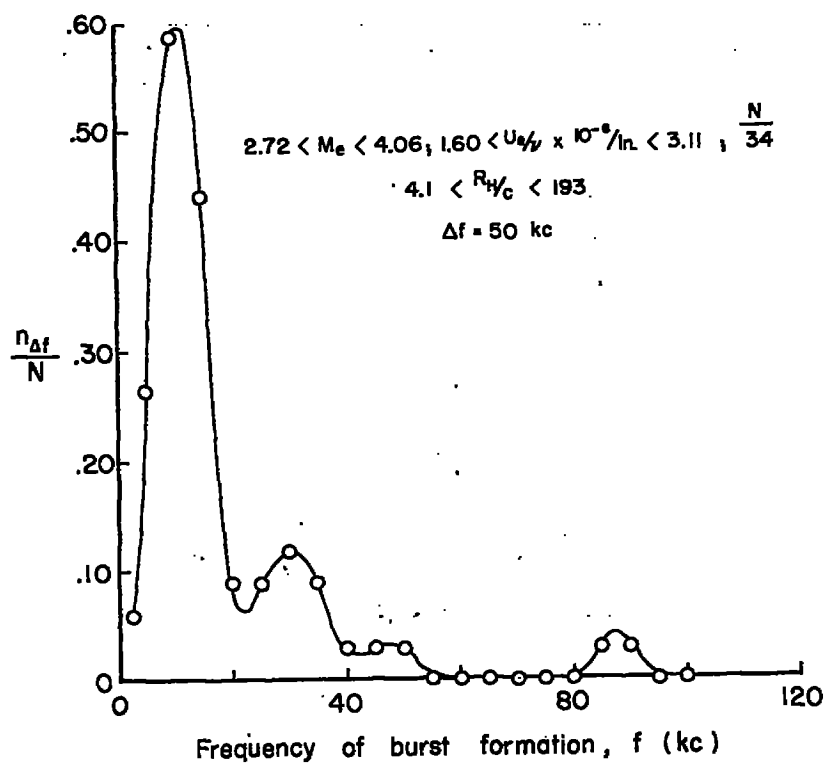
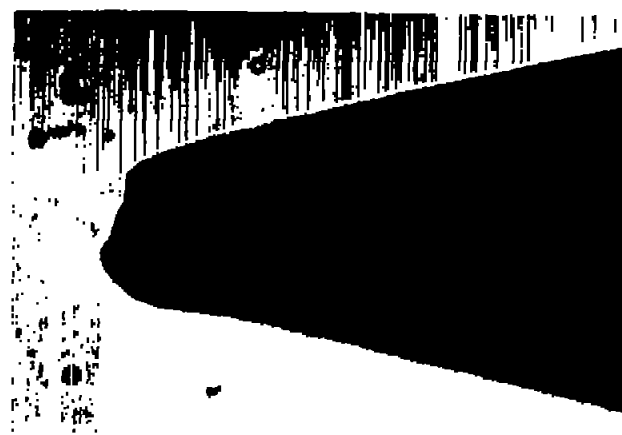


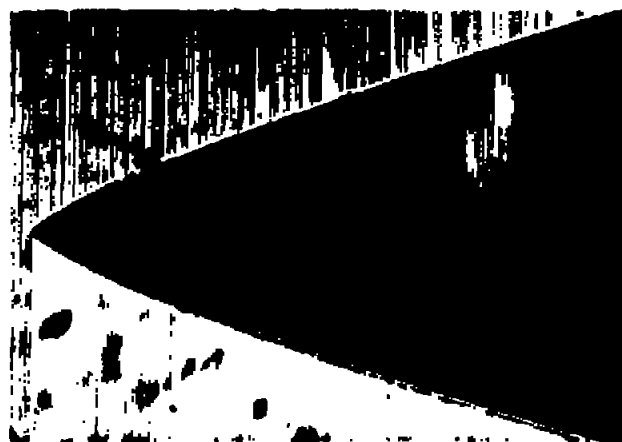
Figure 19.- Spectrum of formation frequency of bursts on the hollow-tube models.



(a)  $19^\circ$  included-angle cone; orthogonal views of the same tip.



(b)  $19^\circ$  included-angle cone.



(c) Pencil model.

Figure 20.- Photomicrographs of model tip profiles; 300X.